

Field Experiment on Sub-mesoscale Spatio-Temporal Variability in Linden- berg



A joint project within the Hans-Ertel Center for Weather Research Phase 3 (2019-2022)

Meteorological Institute, Hamburg Universität

Max Planck Institute for Meteorology

Institute for Geophysics and Meteorology, University of Cologne

Institute for Meteorology, Freie Universität Berlin

Institute for Atmospheric and Environmental Sciences, Goethe Universität Frankfurt

Meteorological Observatory Lindenberg – Richard-Aßmann-Observatory, Deutscher Wetterdienst

In cooperation with:

Institute of Atmospheric Physics, Deutsches Zentrum für Luft und Raumfahrt (DLR)

Environmental Physics, University of Tübingen

Meteorology and Air Quality, Wageningen University and Research

LR-Tech/National Oceanic and Atmospheric Administration (NOAA)

Institute of Geo-Hydroinformatics, Technical University Hamburg-Harburg

Institute of Meteorology and Climate Research - Atmospheric Environmental Research, Campus Alpin, Karlsruhe Institute of Technology

Finnish Meteorological Institute/ University of Helsinki,

Technical University Berlin,

METEK GmbH,

DWD Mobile Messeinheit (MME) Potsdam,

Helmholtz-Centre for Environmental Research GmbH (UFZ Leipzig)

Executive Summary

Measuring variability on scales finer than $O(10\text{ km})$ and therefore developing a hierarchical measurement strategy were the core tasks of the field campaign FESSTVaL, a field campaign initiated by the Hans-Ertel-Center for Weather Research (HErZ). During the summer months of 2021, FESSTVaL took place at the Meteorological Observatory Lindenberg – Richard-Aßmann-Observatory (MOL-RAO) of the German Weather Service (DWD) near Berlin. Prior to this, three preparatory campaigns were conducted in 2020, called FESST@home, as due to pandemic restrictions, the main campaign had to be postponed to 2021. With respect to the source of submesoscale variability, FESSTVaL and FESST@home focused on three main aspects: boundary layer patterns, cold pools, and wind gusts. The field campaigns combined vertical profiling of the atmosphere and surface observations, as well as commercial and low-cost self-design instruments. The collected measurements are used to (i) improve our process understanding, (ii) validate aspects of convection-permitting Numerical Weather Prediction (NWP) simulations and (iii) compare different measurement strategies and instrument types for the development of future measurement networks. This report gives a comprehensive overview of the measurement strategy and results achieved during FESST@home and FESSTVaL. A shorter overview article summarizing the measurement strategy and first results of FESSTVaL is currently under review in BAMS. All the data collected can be accessed via this webpage:
<https://www.cen.uni-hamburg.de/en/icdc/research/samd/observational-data/short-term-observations/fesstval.html>

1. Introduction

The **Field Experiment on Sub-mesoscale Spatio-Temporal Variability in Lindenberg (FESSTVaL)** took place in the summer of 2021 (May-August) with an IOP from June 5 to July 5, 2021. The idea of the field campaign was to deploy a hierarchical measurement strategy with the goal of observing features of the atmospheric flow occurring on scales between 100 m and 5 km. Such phenomena cannot be properly resolved and characterized from standard operational networks, e.g., the automatic measurement stations of the German Meteorological Service (Deutscher Wetterdienst, DWD) have a typical horizontal distance of 25 km. This results in a lack of data both for process understanding and for the validation of NWP models and large-eddy simulations (LES) results. Collecting information from observations at the sub-mesoscale therefore closes a relevant data gap.

The aims of FESSTVaL were to

1. measure sub-mesoscale variability by using new measurement devices and new measurement strategies
2. validate the representation of sub-mesoscale variability in convection-permitting models
3. use the observations for process understanding, in particular to investigate controls on and effects of sub-mesoscale variability.

The combination of these three goals contributes to an assessment of the possible ground-based observational network of the future. The goals also imply a synergistic use of measurements, models, and procedures for enhanced understanding of processes, for the further development and evaluation of models and procedures, and for the communication and presentation of products. As such, FESSTVaL addresses two objectives of the cross-cutting topic.

Initially, FESSTVaL was planned to take place in summer 2020. Due to the COVID-19 pandemic, FESSTVaL had to be postponed to the following year. Instead, in 2020, three preparatory measurements were conducted “at home”, the so-called FESST@home.

2. FESST@home in 2020

2.1 FESST@HH

2.1.1 Measurement strategy

The Field Experiment on Sub-mesoscale Spatio-Temporal variability at Hansestadt Hamburg (FESST@HH) was held at Hamburg (53.5 °N 10.0 °E) between June and August 2020. The observational set up of FESST@HH consisted of a ground-based network of 103 autonomous measurement stations, that covered the greater area (50 km x 35 km) of Hamburg with the primary goal to observe the spatial dimension of convective cold pools. During the experiment, 82 low-cost and self-designed APOLLO (Autonomous cold POoL LOgger) stations sampled air temperature and pressure with fast-response sensors at 1-s resolution, while 21 WXT weather stations with commercial compact sensors provided additional information on relative humidity, wind speed and precipitation at 10-s resolution. The average nearest-neighbor distance between all 103 measurement sites is 1.85 km with a standard deviation of 1.42 km, whereas it is 1.93 ± 1.41 and 5.49 ± 1.98 km for APOLLO and WXT, respectively. The measurement area is crossed by the Elbe river in southeast–northwest direction and is characterized by relatively flat terrain. The altitudes of all measurement sites lie between 1 and 82 m above sea level with an average of 17 m. The observation of convective cold pools by the ground-based station network was completed by an X-band rainfall radar, which is permanently installed on top of the Geomatikum building located in the city center and collects spatial information of precipitation at 30-s resolution within a radius of 20 km.

The measurement period started on 1 June 2020 and ended on 31 August 2020, whereas the installation of all stations was completed in mid-June. The realization of the experiment was enabled by the support of many institutions and private landowners who provided permission at short notice to use their premises as measurement sites. Ensuring the implementation of FESST@HH was compatible with pandemic-related restrictions affected not only the selection of measurement sites but also the maintenance strategy. Instead of a small team servicing the entire network, the maintenance work was shared between nearly 40 people. Private landowners who provided measurement sites in their backyard could also volunteer to regularly change the battery, check the data, and upload it to an FTP server. Other stations located on public grounds, schoolyards, or industrial premises were serviced by colleagues living nearby. The main benefit of this maintenance strategy was that the collective effort kept the individual workload very low and promoted the continuous operation of the instruments, which eventually eased the execution of the experiment under challenging circumstances. Further information on the measurement strategy and technical details of the instruments can be found in Kirsch et al. (2022a).

2.1.2 Methodical and scientific findings

The FESST@HH served as a successful proof of concept for the FESSTVaL measurement strategy for cold pools. The average availability of temperature data for the custom-built APOLLO and WXT stations over the three-month observation period is 83.2 % and 87.6 %, respectively. These numbers increase to 90.0 % and 94.3 % if only the period after completion of the installation phase on 15 June is considered. During this period, the daily availability of APOLLO and WXT measurements is always larger than 82.6 % and 90.0 %, respectively. These numbers are especially remarkable considering the fact that the stations have never been used in such a large number before. Apart from the removed measurements affected by erroneous sensors and local site conditions, most of the data gaps in the APOLLO data are due to missing power supply of the loggers either caused by technical issues related to the power bank batteries or insufficient maintenance. The experience from FESST@HH also helped to further improve the functionality of the APOLLO data loggers and optimize the process of installing and servicing the measurement stations with respect to FESSTVaL 2021.

During the three-month measurement period of FESST@HH, the station network recorded 37 cold pool events. One strong and nearly stationary cold pool on 10 August 2020 is particularly well suited to showcase the ability of the network to capture the morphology and evolution of a cold pool. About 10 min after the X-band radar measured the first precipitation echo of a convective cell east of the city center, the formation of a cold pool became evident from a rapid cooling of the surface-layer air. About 20 min after initiation of the convective cell, the cold pool exhibited a temperature perturbation of up to -8 K within an area of less than 10 km in diameter. After another 20 min, the temperature perturbation strengthened to about -11 K and the cold pool expanded to a size of roughly 10 km \times 20 km. At time of maximum intensity, the cold pool reached its temperature perturbation of about -12 K and a diameter of nearly 30 km. The strongest horizontal temperature gradient caused by the cold pool is 12 K within a distance of 11 km. The associated near-surface wind field observed by the WXT weather stations indicated a strong divergent flow at the cold pool center especially during the early stages of the cold pool's life cycle. Consistent with expected characteristics of a cold pool, the radial expansion of the cold-air region during the later stages was also present in the wind observations predominantly southwest of the cold pool center. According to the time lags between the cooling signals at different locations, the propagation velocity was about 4 m/s.

Apart from cold pool observations, the FESST@HH measurement setup is also capable to provide insides into other meteorological processes like the nocturnal urban heat island and variations of turbulent temperature fluctuations associated with different urban and natural environments. Further details on the findings of FESST@HH are described in Kirsch et al. (2022a).

2.2 FESST@Oberland

How can we make pupils aware of extreme weather events and the associated risks? This question was the subject of a research project called *KARE-CS* in the summers 2020/21 in the Bavarian Oberland, carried out by Freie Universität Berlin and Ludwig-Maximilians-Universität München in cooperation with the regional community foundation "Energiewende Oberland" (EWO), see Kox et al. 2021a,b for the description and some results. The project was funded by the Federal Ministry of Education and Research (BMBF). Since the technical concept and the staff of this project were very similar to FESSTVaL, it was mutually very helpful for further development and testing the MESSI device and web app and the weather risk survey. For further information on the project, see <https://klimaanpassung-oberland.de/de-de/schueler-innen-forschen/>.

2.2.1 Measurement strategy

The instrument set up was very similar to FESSTVaL (see 3.1.1.2), yet the measurement device *MESSI* (an automated weather station measuring pressure, temperature and radiation) was supplemented with a rain gauge as heavy precipitation events were a focus of the overarching project *KARE*. The participants assembled the *MESSI*s with help of a well-designed manual; They tested its functionality with simple experiments. The project was introduced during group video calls, in which pupils could eventually seek help if they had problems with assembling the instrument. A web application was used to provide instant view of the measurement data as well as information on the project, assembly, installation and maintenance instructions. 80 *MESSI*s were built, set up and maintained in the gardens of pupils of five schools in the region. Surveys were developed to test the knowledge about weather risks, observed climate change and the local climate.

2.2.2 Methodical and scientific findings

Although it was not the focus of this project, cold pools were also detected. Figure 1 shows the sudden drop in temperature by about 6K in 20 minutes, accompanied by a fast rise and subsequent fall in air pressure by 1 hPa and a drying of the air by a maximum of 2K in dew

point (relative humidity raises to 100%, not shown).

Since on site workshops were not possible due to the pandemic situation, digital materials on building, operating and maintaining the *MESSI*s were developed.

The project included workshops during and after the measurement period in which the data for specific events were analysed by the pupils. In order to allow this comfortably, the web app was extended to allow to view the complete archived data. Partly because of the structured terrain of the region, we learned to make more use of indoor gateways to fill in gaps in the radio network. Furthermore, good contacts with the local population, administration and craftsmen turned out to be essential for constructing and maintaining the radio infrastructure.

During the final workshops pupils drew sketches of their measuring site. The aim was to confront the pupils with the fact that measurement quality is affected by the placing of the device and that potential changes of its environment (growing trees, new buildings etc.) will have an impact on the long-term comparability of measurements. Documentation of the site is therefore necessary as well as citizen contribution to the scientific metadata on the measurements.

A teaching concept and materials were developed, aiming at pupils and teachers (grammar to high school) as well as other interested groups, which is action- and reflection-oriented: <https://klimaanpassung-oberland.de/de-de/schueler-innen-forschen/ergebnisse-und-berichte/bildungskonzept-fuer-schulen-und-andere-gruppen-2762911/>

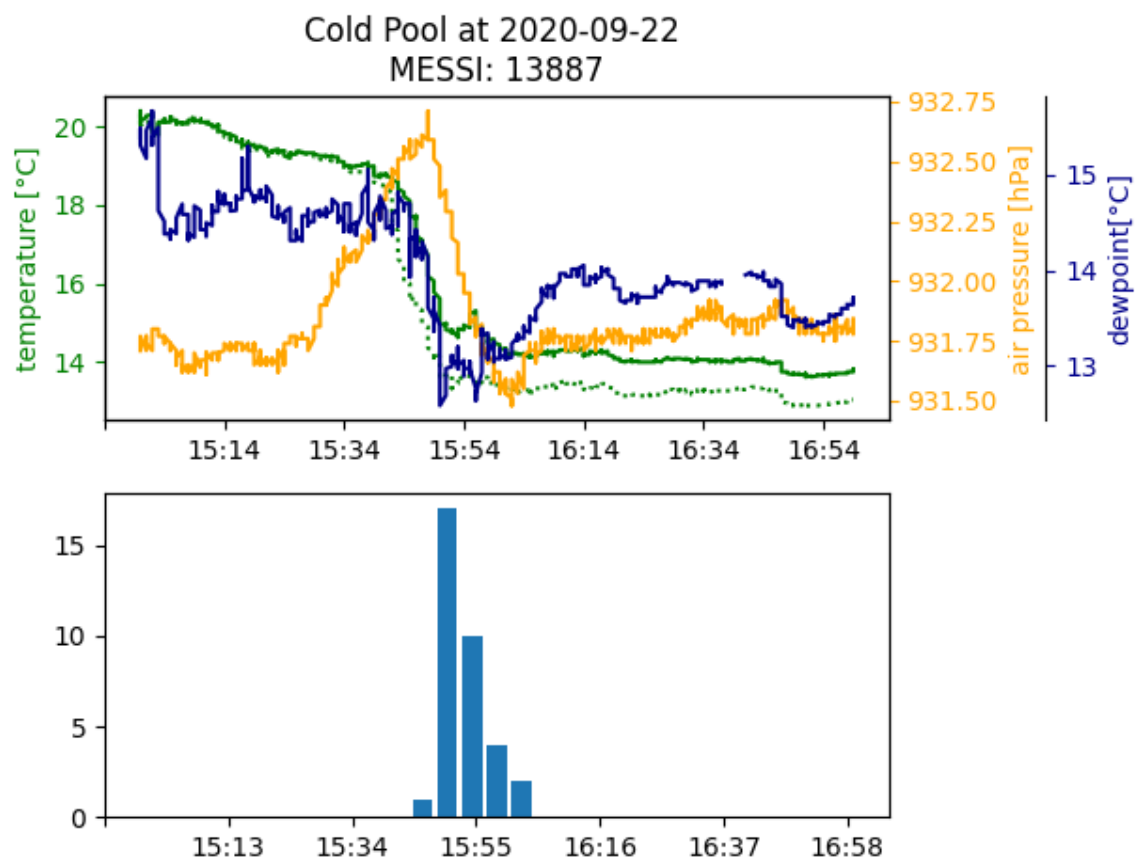


Fig. 1 Cold pool detected by a MESSI on 22.09.2020. Upper panel: temperature inside (dotted line) and outside (solid) the hut, dew point and air pressure at station height (about 600m). Lower panel: precipitation in number of pulses per 5 minutes, 3 pulses denote about 1mm of rain.

2.3 FESST@MOL

2.3.1 Measurement strategy

Measurements with Doppler lidar (DL) systems to derive profile information on wind and turbulence in the atmospheric boundary layer (ABL) were planned as a core contribution to FESSTVaL. Instead of operating DLs at different sites around Lindenberg (as planned for FESSTVaL), measurements with eight DL systems were performed at the boundary layer field site (GM) Falkenberg between June 01, and August 31, 2020. In addition to the two DWD instruments, two co-operation partners (KIT Campus Alpin Garmisch-Partenkirchen and the Institute for Atmospheric Physics at DLR Oberpfaffenhofen) brought each three DLs to Falkenberg. Moreover, measurements with small uncrewed aircraft systems (UAS) were performed at GM Falkenberg by the Environmental Physics group at Eberhard Karls University Tübingen (EKUT) and by DLR. EKUT operated their fixed-wing Multipurpose Atmospheric Sensor Carrier (MASC-3). 72 flights each lasting between 60 and 90 minutes were performed during the period July 07-31, 2020. DLR operated a fleet of racing quadrotors (SWUF-3D) for wind measurements in the lower ABL. During the period July 20-31, 2020 they realized 76 flights with up to ten quadrotors in the air simultaneously for about 6 -12 minutes.

All these measurements were oriented towards the following scientific-technical goals:

1. Comparison of different DL scan configurations to derive profiles of the mean wind vector and of the turbulent kinetic energy (TKE) among each other and versus in-situ measurements at the 99m tower, this included both single- and triple lidar configurations.
2. Test and assessment of different algorithms to derive and to characterize wind gusts from DL measurements.
3. Test of different UAS flight strategies suited to validate DL wind and turbulence retrievals by UAS measurements.
4. Test of different sensor packages at MASC-3 (gas and aerosol particle sampling, dew-point mirror for humidity fluctuation measurements) and validation of the SWUF-3D swarm flights vs. tower and DL wind measurements in different flight configurations.
5. Characterization of the diurnal cycle of the three-dimensional wind and turbulence fields in the ABL above a heterogeneous land surface.

To achieve these goals, the DL systems were operated in a number of different scan configurations (e.g. „vertical stare“, „virtual tower“, continuous and step-stare conical scan, horizontal / vertical sector scans <PPI, RHI>). Studies regarding the last question were supported by measurements of the components of the surface energy budget above the grass at GM Falkenberg (DWD) and above a neighboring corn field (KIT).

The setup of the DL systems at GM Falkenberg during FESST@MOL is sketched in Figure 2, Figure 3 shows pictures of the major measurement systems operated and tested during FESST@MOL.

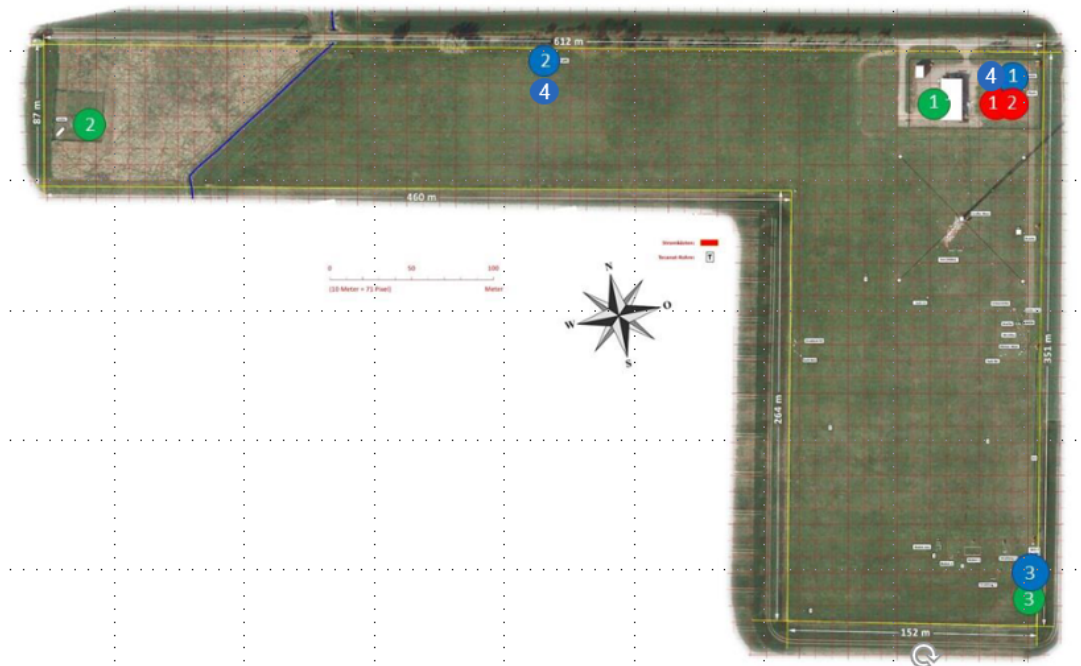


Figure 2 Map of GM Falkenberg with the positions of the tower and DL systems indicated (red: DWD DL systems Streamline #78, #177; blue: KIT DL systems Streamline #161, #74, #75, #26; green: DLR systems WindCube 200 #89, #86, #85)



Figure 3 Measurement systems operated during FESST@MOL: (left) A DL WindCube 200 (Leosphere) and a DL Streamline (Halo Photonics) in front of the 99m tower at GM Falkenberg, (center) MAS-3 approaching for landing, (right) a SWUF-3D quadrotor close to the 99m-tower at GM Falkenberg

2.3.2 Methodical and scientific findings

2.3.2.1 Wind profile measurements with DL systems

Typically, one DL system, operated in either a velocity-azimuth-display (VAD) configuration or in a Doppler-beam-swinging (DBS) mode, is employed to derive vertical profiles of the wind vector across the ABL. Both measurement modes rely on the assumption of horizontal homogeneity and stationarity of the wind field. They are based on line-of-sight radial velocity measurements at different azimuth angles performed sequentially at a fixed zenith angle (of typically between 15° and 55°). The single measurement rays form a cone with a diameter rapidly increasing with height. The completion of one measurement cycle needed to derive the wind vector is typically achieved within 20 to 120 seconds depending on the number of beam directions and the mode of positioning the scan head of the DL (either continuous scan mode (CSM)

or step-stare mode (SSM)). Alternatively, a triple-DL setup allows to derive the wind vector within a small sampling volume and a kind of virtual tower (VT) can be built by changing the elevation angles of the different DL systems. It was one goal of FESST@MOL to quantify the differences in the derived wind vector values between a single-DL- and triple-DL setup. For this, two DL systems were operated in a CSM mode with zenith angles / cycle times of $28^\circ / 3.4$ s and $54.7^\circ / 72$ s, respectively. Each three WindCube 200S and three Streamline DL systems were arranged as VTs, and the following configurations were tested:

- Tower setup: L-shape, T-shape, Y-shape
- Measurement mode: VT01 = one DL in vertical stare, two performing continuous RHI scans, VT02 = one DL in vertical stare, two performing step-stare elevation scans with six fixed positions between 90 m and 500 m above ground where the beams remained at each height for 30 minutes, VT03 = one DL in vertical stare, two in slanted stare providing data at one level with 1 s time resolution

At 90 m height, both the single DL VAD wind and the triple DL VT winds were compared against sonic measurements at the meteorological tower at GM Falkenberg. Selected statistical results of the intercomparison between the fast CSM VAD retrieval and the VT02 mode are given in Table 1.

	Height (m)	Averaging Time (min)	Bias (m/s)	RMSD (m/s)
VAD vs. sonic	90	10	-0.02	0.33
VT02 vs. sonic	90	10	0.09	0.45
VAD vs. sonic	90	30	-0.03	0.32
VT02 vs. sonic	90	30	0.12	0.47
VAD vs. VT02	95	30	0.15	0.32
VAD vs. VT02	250	30	0.30	0.58
VAD vs. VT02	500	30	0.58	0.82

It becomes obvious, that the VAD-VT intercomparison provides results comparable to the DL-sonic intercomparison at 90 m height, but both the bias and the RMSD values of the VAD-VT DL intercomparison increase with height which might be attributed to the increasingly different spatial representation of the wind retrieval due to the larger sampling volumes of the VAD scan in the slow CSM with a 54.7° zenith angle.

2.3.2.2 Experiences with special DL operation modes for the derivation of wind gusts and TKE

Two special DL configurations to derive wind gusts and turbulence variables had been identified – we called them fast CSM and slow CSM. Both modes were extensively tested during FESST@MOL. Their basic configuration parameters are given in Table 2.

Mode	Zenith angle (deg)	Number of pulses per ray	Azimuthal resolution (deg)	Scan duration (s)
Fast CSM	28	3000	30-35	3.4
Slow CSM	54.7	2000	1-2	120

During FESST@MOL important operational experience with both modes could be obtained, some of the most relevant conclusions were:

- For both CSM it is recommended to change the direction of rotation of the lidar scan head cyclically every 30 minutes in order to avoid the risk of an overflow of internal counters (in particular for the fast CSM). This can be realized by configuring daily scan files for the operation of both systems.

- For the CSM, the assignment of the azimuthal position of the scan head does not occur at the center position of the azimuthal sector covered by the rotation during the emission of pulses forming one ray. This became obvious through regular artificial jumps of wind direction every 30 minutes in the fast CSM and needs to be corrected in the data processing. For the slow CSM, the effect is negligible because the azimuthal resolution is at 1-2 degrees.
- For the slow CSM we tested different pulse numbers per ray (2000, 4000, 6000), the operation with 2000 pulses per ray appeared to be mandatory in order to ensure the high azimuthal resolution necessary to implement the correction algorithm suggested by Smalikho and Banakh (2017, see below in 2.3.2.4).
- Due to the low number of pulses per ray in both CSM tested, the signal-to-noise ratio (SNR) is relatively low. This implies that standard quality control procedures using a fixed SNR threshold are not appropriate as (unique) basic criterion for filtering of noisy data. In conclusion, special filtering algorithms had to be developed, these efforts became a major work package for the analysis of the FESST@MOL and later FESSTVaL data.
- For one of our systems operated during FESST@MOL data availability and quality rapidly decreased with height due to a mismatch between the configured and real focus settings.

2.3.2.3 Retrieval of wind gusts from DL measurements

The fast CSM described in the previous section has been identified as a promising way to derive wind gusts from DL measurements. Operation of the Streamline DL with a cycle time of 3.4 s to complete one full scan circle allows a temporal resolution for the derivation of the wind vector very close to the standard WMO definition of wind gusts (3s-running mean). Two algorithms have been developed to analyse these data (Steinheuer et al., 2022, Detring et al., in preparation). As an example, Figure 4 shows the diurnal evolution of the mean and gust wind speed as derived from the DL measurements in comparison with the sonic data. It becomes obvious that the DL-retrieved values nicely follow the in-situ measurements.

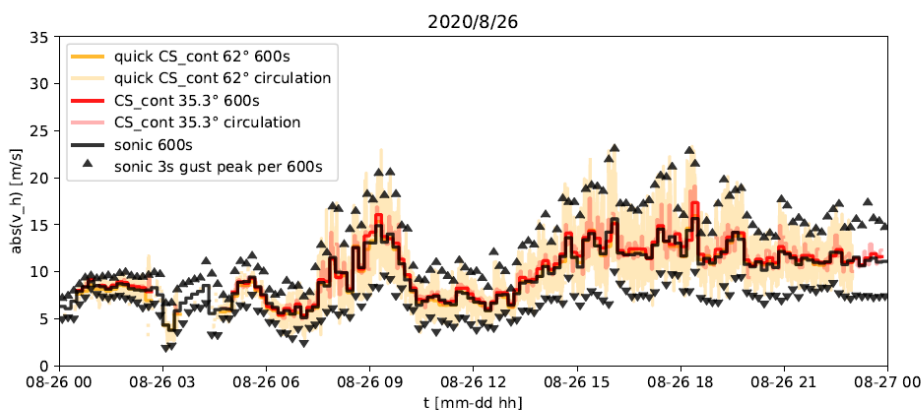


Figure 4 Diurnal evolution of the mean, maximum and minimum 3-sec wind speeds at 10 minutes resolution derived from DL measurements using the algorithm by Steinheuer et al. (2022) and from sonic anemometer data at 90 m height for August 26, 2020.

Figure 5 presents the statistical results of the maximum wind speed intercomparison between DL and sonic at 90 m for the whole FESST@MOL data set (June 01 – August 31, 2020). Both values are highly correlated, no systematic deviations are found, and a root-mean-square difference of 0.71 m/s is in the order of typical deviations between point and volume-averaged wind speed data.

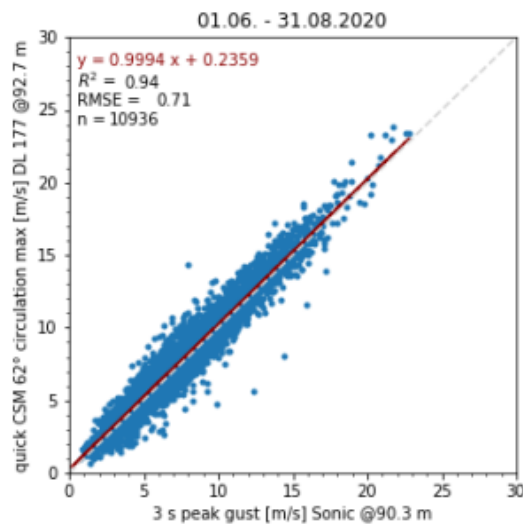


Figure 5 Scatter plot of 3sec maximum wind speed values at 10 minutes resolution as derived from DL and sonic anemometer measurements during FESST@MOL at a height of 90 m a.g.l., the DL data are based on the algorithm by Detring et al. (in preparation)

2.3.2.4 Derivation of the TKE from DL measurements

Turbulence kinetic energy (TKE) is an important process variable to characterize the ABL. Routine TKE measurements are typically performed using 3D ultrasonic anemometers; this limits their availability to near-surface levels (up to about 200 m above ground at a few tower sites). Alternatively, TKE may be derived from measurements with ground-based remote sensing instruments, such as DL. Based on a method proposed by Kropfli (1986) for the derivation of TKE from Doppler radar measurements, Smalikho and Banakh (2017) suggested an algorithm to derive TKE profiles from DL measurements. The method includes a correction for the underestimation of TKE due to pulse volume averaging effects. Concerning data acquisition, it requires a conical scan with a comparably high azimuthal-temporal resolution (< 2 deg, < 5 s) which was realized by configuring the scanner using continuous motion (CSM) with a relatively small number (2000) of lidar pulses per ray. This can have a negative effect on the quality of measurement data (e.g. increased fraction of noise) if DLs with pulse accumulation are used. The particular challenge for this operation mode is a proper filtering of noise prior to a TKE retrieval, since even small amounts of noise can lead to large errors in the retrieved TKE product. An example to illustrate the above described issues is shown in Fig. 6 for May 17, 2020. During the night the time series plot of radial velocity measurements (Fig. 6a) clearly shows next to reliable data also a huge amount of noise (outliers) randomly taking any value over the whole measurement range $[-20$ m/s, $+20$ m/s]. Additionally, it is shown that the application of a classical data filtering method such as the SNR threshold technique helps to reduce some noisy data, but the chosen threshold ($\text{SNR}_{\text{thresh}} = -18.2$ dB) does not seem suitable to remove them all. Further increasing this threshold would become more effective in removing noisy data, but it carries the risk of unnecessarily rejecting a large amount of reliable data (not shown here). This in turn would prove unfavourable for the overall TKE product availability for a routine 24/7 application. Hence, during FESST@MOL we started to experiment with new filtering techniques to overcome the above described issues. A first simple approach was to test the

SNR thresholding technique in combination with the 3-sigma rule of thumb which is frequently used for outlier detection. However, the filter results were not satisfactory due to the low robustness of the 3-sigma rule against outliers. This is due to the fact that, depending on the fraction of outliers, the statistical parameters mean and standard deviation (σ) used as input data for the 3-sigma test are also affected by outliers. The latter is evident in the poor filter results of an originally noise-contaminated 30min measurement interval where the above described filtering technique has been applied (Fig. 6c). Although compared to Fig 6a noisy data could be further reduced and narrowed down to a range between about $[-6 \text{ m/s}, +4 \text{ m/s}]$, the noise fraction is still too high, so that the derived TKE product shows a strong overestimation of TKE compared to independent sonic measurements (Fig. 6b). To rule out that the method might introduce errors contributing to such an overestimation, additional results based on an arbitrary noise-free 30min measurement interval are shown in Fig. 6d. Here, the good agreement between DL TKE and sonic TKE indicates that the method itself is suitable to retrieve TKE, provided the measurements are free of noise. These insights into both the existing potential of the method to deliver reasonable results but the emerging problems in data filtering with classical approaches in cases of noise contaminated measurements finally triggered further activities to implement and to test more advanced filtering techniques.

In addition, the algorithm suggested by Smalikho and Banakh (2017) allows to derive profiles of momentum flux, eddy dissipation rate and the integral length scale of turbulence. Thus, a consistent data set to characterize turbulent processes in the atmospheric boundary layer can be obtained.

17.05.2020, height = 95m, CSM conical scan ($\Delta \theta < 2$, $T_{\text{scan}} = 72\text{s}$)

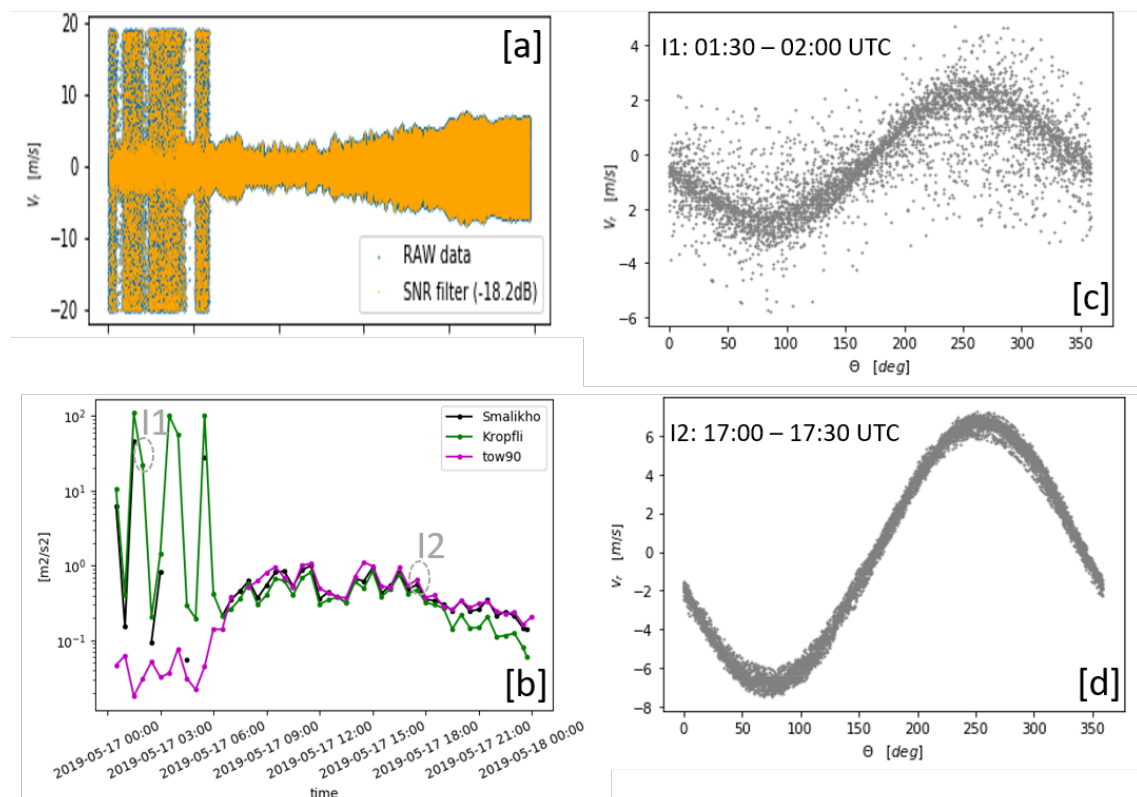


Figure 6 (a) Time series plot of DL radial velocity V_r at 95m height for May 17, 2020. (b) Comparison of 30min averaged TKE from DL at 95m with sonic at 90m height. Both the DL TKE determined using the Kropfli and the Smalikho&Banakh methods are shown. (c), (d) VAD diagrams from conical scans over two selected 30min intervals (marked I1 and I2 in (b)) which differ with respect to the degree of noise contamination.

2.3.2.5 The horizontal wind field derived from DL measurements

In order to investigate the local spatial and temporal variability of the wind field, PPI/RHI scans were realized with a triplet of Leosphere WindCube 200 DL systems. Two lidars performed PPI scans at low elevation (1° to 2°) over a sector of about 120° , and the third one was operated in RHI scan mode between 0° and 60° elevation pointing at a fixed azimuth direction either centred in the sector covered by the two PPI systems or adjusted to the actual wind direction. Figure 7 shows an example of the reconstruction of the instantaneous wind field close to GM Falkenberg from these measurements.

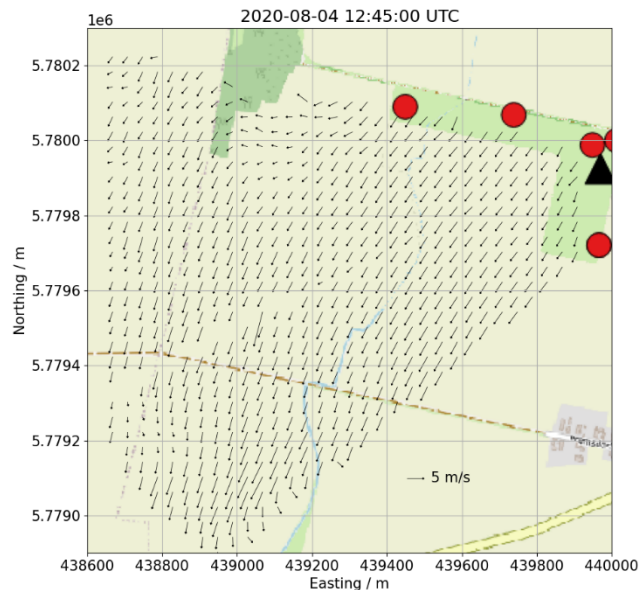


Figure 7 Horizontal wind vector field in the sector SW of GM Falkenberg reconstructed from two PPI-scanning DL on August 04, 2020, 1245 UTC (red dots show the position of the DL systems in FESST@MOL – the double PPI scans were performed by the upper left and lower right lidar systems, black triangle marks the position of the 98m tower)

2.3.2.6 Test of MASC-3 flight patterns for the validation of DL wind retrievals

Different MASC-3 flight patterns for the validation of DL wind retrievals were tested during FESST@MOL, these included

- VT validation flights (legs at different heights parallel to mean wind),
- VAD validation flights (single legs at different heights both aligned with the mean wind and with a fixed geographical orientation, two- and four-leg patterns forming either a cross or a square centred above the lidar location),
- Boundary layer profile flights with single legs at different altitudes normalized with respect to the ABL height.

Besides these tests of different flight patterns, methodical questions had to be considered for the comparison of UAS- and DL-based wind retrievals taking into account the different spatial and temporal sampling strategies. As an example, Figure 8 illustrates the variability of the wind profile during one MASC flight such that for a fair comparison a lidar composite needs to be constructed from the profiles derived for consecutive time intervals.

2.3.2.7 SWUF-3D wind retrievals

Three flight patterns were realized with the SWUF-3D quadrotor fleet

- Drone tower (8 drones at different heights very close to the Falkenberg tower, these flights were used to calibrate the wind retrieval from the quadrotor dynamical behaviour),

- Lidar PPI pattern (grid of 3*3 drones SW of Falkenberg tower in the are covered by the lidar PPI scans (see 2.3.2.5)),
- 8 drones along the ray of a slanted stare lidar (intercomparison with lidar radial velocity measurements at high temporal resolution).

The validation of the wind retrieval from the drones vs. the in-situ sensors at the tower resulted in an RMSD $< 0.3 \text{ ms}^{-1}$ for 10-minute averages. Comparison of the profiles of the retrieved wind vector revealed good agreement between the vertical wind shear as derived from the drones and from the tower sensors. Also, the fluctuations on short timescales agree between the systems. Detailed flow structures became visible in the two-dimensional lidar scan pattern (3*3 grid) and in the time series of the lidar line-of-sight measurements observed with the fleet of quadrotors and were sampled with an even higher time resolution than the deployed lidar could provide (Figure 9).

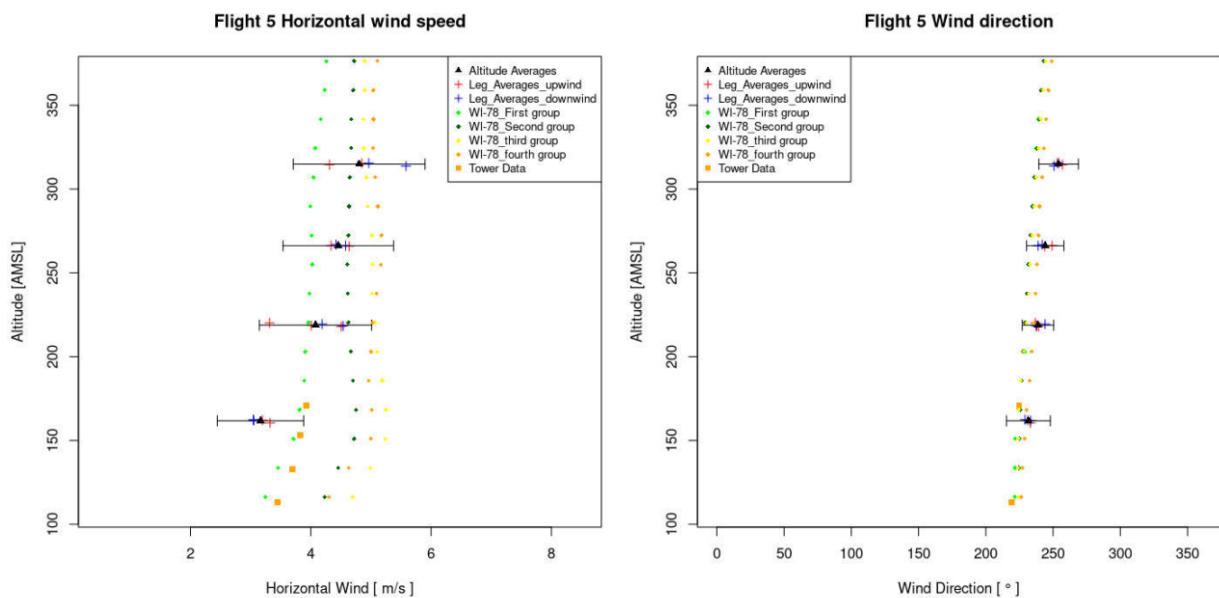


Figure 8 Wind profiles in the lower ABL as derived from MASC-3 measurements at four altitudes compared to a series of 10-minute-averaged DL wind profiles on July 08, 2020, 1505-1625 UTC.

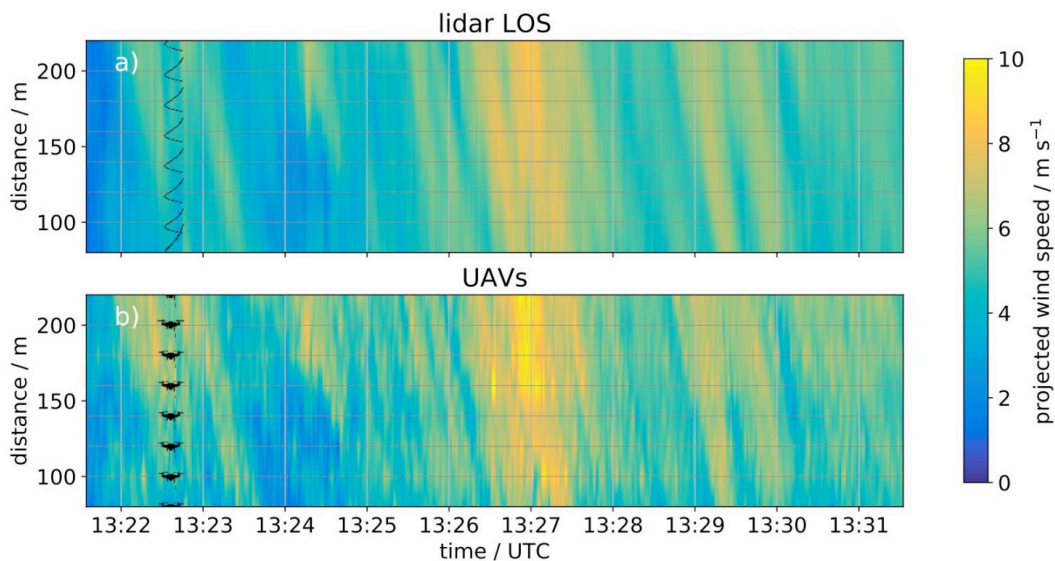


Figure 9 High-resolution spatio-temporal variability of the projected wind speed derived from DL measurements and from a fleet of 8 quadrotors operated along the slanted DL path on July 30, 2020.

3. FESSTVaL

3.1 Measurement setup

The FESSTVaL measurement strategy combined a dense network of surface observations deployed within a circle of 15-km radius around the boundary layer field site (in German: Grenzschichtmessfeld, GM) Falkenberg of DWD with a vertical sampling of the atmosphere at the three supersites GM Falkenberg, Lindenberg and Birkholz. The achieved spatial resolution in the FESSTVaL circle ranges between 100 m and 5 km, whereas the edge length of the triangle is 5-6 km. Additional instruments were located at GM Falkenberg to get more information on variability on scales smaller than 100 m. On top of that, FESSTVaL could rely on the routine measurement program of MOL-RAO. This includes operation of a suite of ground-based remote sensing instruments (482-MHz radar wind profiler, cloud radar, several water vapor lidars, several ceilometers), operational radiosoundings (regularly at 04:45 UTC, 10:45 UTC, 16:45 UTC and 22:45 UTC), the Lindenberg Baseline Surface Radiation Network station, and micrometeorological measurements at GM Falkenberg (surface energy budget, soil temperature and soil moisture, tower profiles of wind, temperature and humidity between 0.5 m and 98 m) and at a forest station.

3.1.1 Surface observation networks

3.1.1.1 Apollo / WXT networks

Surface observations were performed by WXTs. The WXT weather stations employ a compact multi-parameter sensor developed by Vaisala. They record basic meteorology in terms of temperature, pressure, relative humidity, wind speed, wind direction and precipitation. Solar panels ensure their power supply. WXTs are widely used commercial instruments, but their cost limits the number of stations within a network. Nineteen instruments were deployed during FESSTVaL, with distances ranging between 1.5 and 9.6 km, giving a median distance of 4.9 km.

To augment this spatial resolution, 80 Autonomous cold POoL LOggers (APOLLOs) were added to the network. The spatial density diminishes from the center of the FESSTVaL circle (100 m) towards its edge (4.8 km). The median distance is 1.8 km. The majority of stations was installed along public roads, while the remaining stations formed local clusters at the three supersites Lindenberg (three stations), Falkenberg (five stations), and the fields of a farmer in Birkholz (three stations). APOLLOs are self-developed instruments, with a cost of around 300 Euro per station, see Kirsch et al. (2022) for a comprehensive description of the instruments. APOLLOs measure temperature and pressure, two quantities that are straightforward to measure at low cost and allow a reliable detection of cold pools. A battery provides the necessary power, but the battery needs to be changed every 10-14 days. This makes APOLLOs maintenance-intensive. Servicing through all stations resulted in a tour of about 350 km. This effort limited the area size that could be covered by APOLLOs. The overall availability of quality-controlled data is 92.0% and 98.1% for the APOLLO and WXT stations, respectively.

3.1.1.2 MESSI network

A network of citizen weather stations called MESSI (translation: “My Own Sub-Scale Instrument”, see Fig. 10) was operated starting in middle of June 2021 until the end of FESSTVaL. MESSIs are low-cost devices designed and pre-manufactured in-house (Kox et al. 2021). Every 10 seconds, MESSIs measure temperature, relative humidity, pressure and light intensity. MESSIs were designed to be energy autonomous and independent of Wifi to allow a free choice of placement and avoid near-to-house-installation. 70 MESSIs were distributed to citi-

zens who live in the villages and small towns in the area of the FESSTVaL region. This collaborative involvement of citizens implied the risk of sub-optimal assembly, placement and maintenance, although the citizens were guided on those aspects during a virtual workshop, and provided with extensive documentation and an email hotline. The Long-Range Wide Area Network (LoRaWAN) technology is independent of participants' wifi. It transfers data so that it is available in near real time. To receive the data from the MESSIs 6 LoRaWAN outdoor gateways and 10 LoRaWAN indoor gateways were installed and operated by the MESSI-team. Data can be visualized in real time with a web application (still active for a follow-up project and hosted at https://messi.openuco.berlin/public_devices). Data transmission failures and a few instrument outages meant that about 60% of the installed data capacity was viewable in real time (Fig. 10). Data were also stored in flash memory directly on the device and were thus available close to 100%, when the instruments were returned at the end of the campaign.



Figure 10 Left: Example of installed MESSI. Right: Daily time series of data reception in real time with distribution of number of hours (top right) and number of MESSIs (bottom right).

For the social scientific goal of the project, at the beginning and at the end of FESSTVaL, questionnaires tested the level of knowledge and understanding of weather forecasts and warnings. The aim was to investigate the effect of participation in the measurement campaign on the understanding of weather forecasts, warnings and weather risks, and to evaluate the measurement campaign by the participating citizens. The original plan was to involve primary school pupils only, in order to: 1) have a sample of people with relatively similar knowledge about weather risks prior to the participation or non-participation for the reference group; 2) to have little communication overhead because of the involvement of whole classes, supported by their teachers. Due to the Covid-19 pandemics this set up was not possible to realize anymore. Participants of all ages were now acquired via the MOL-RAO, the “Weather Museum” and local media.

3.1.1.3 Soil network

Most WXTs and APOLLOs were paired with commercial soil sensors (Soil Analysis Sensor, Scanttronic, Germany) to obtain concurrent measurements of the atmosphere and soil states, allowing to study interactions between cold pools and the surface. The soil sensors were placed at the surface to measure skin temperature and at 11cm below the surface to measure temperature and soil moisture. A battery, which has a lifetime of about one month by a measurement sampling rate of 5 min, provides the power supply. Additionally, 29 soil sensors were deployed at GM Falkenberg, with distances of O(50 m). The aim was to capture variability at scales smaller than in the FESSTVaL circle as soil moisture is known to be highly variable.

3.1.1.4 Surface solar irradiance network

From June 14 until 29, we have deployed a network of custom multi-band radiometers with the goal of measuring local surface solar irradiance variability driven by clouds. This was the first official field campaign that our instruments are deployed at. We have gathered good data, but also discovered unexpected shortcomings. In the next two paragraphs, the measurement strategy, instruments, and resulting dataset are described.

Using low-cost, custom radiometers, described in Heusinkveld et al. (2022), we have measured surface solar irradiance in a network of 24 sensors. The first 20 were located at Falkenberg in a rectangular 4x5 grid with 49 meters horizontal spacing. The other 4 were spread around the FESSTVaL area to the west, south, east and north at about 5 kilometers away, next to WXTs. Our instruments measure the solar spectrum at 18 wavelengths (410 to 940 nm) with a sampling rate of 10 Hz. We have near perfect data completeness from June 14 to 29, with the notable exception being maintenance (cleaning, data checking). On some days, we have additional cloud camera images to help interpret observations of surface patterns captured by the radiometer network.

Resulting products from our instrument network are calibrated global horizontal irradiance (which is the integrated spectrum signal) at 1 second and 0.1 second resolution. Calibration is done against the Falkenberg sun-tracker. A showcase of calibrated data with cloud cameras is available on Vimeo: <https://vimeo.com/645952995>. We discovered some issues with about two-thirds of the wavelengths, that make it hard to provide reliably calibrated spectra for individual wavelength bands.

3.1.1.5 Soil moisture monitoring with stationary and mobile CRNS

The method of cosmic-ray neutron sensing (CRNS) is a novel technique to measure average root-zone soil moisture at the field scale (Zreda et al. 2012). The instrument consists of a passive neutron detector at 1-2 meters above the ground which counts the number of neutrons in the atmosphere. The method takes advantage of the permanent and omnipresent background radiation which consists of cosmogenic epithermal neutrons that are highly sensitive to soil moisture. Epithermal neutrons have probed the soil into depths from 10 to 70 cm depending on water content, and, once reflected back, mix in the air within 10-10 hectares (Köhli et al. 2015). This way, the system can measure the surrounding average water content independent of small-scale heterogeneity. All devices also measure air temperature, air humidity, and air pressure as auxiliary data.

In the scope of FESSTVaL (Fig. 11), the temporal variation of soil moisture has been measured with 20 minutes resolution by a stationary CRNS system (Schrön et al. 2018a) in Falkenberg (52.165, 14.121), and with a 1 minute resolution by a mobile CRNS system (Schrön et al. 2018b) on Aug 18 and Aug 27, 2021 in and around Falkenberg in a ~100 km² area. The route has been designed along the APOLLO and WXT stations that were distributed in the area in order to facilitate later comparison studies.

Temporal measurements show strong signals of precipitation events in the summer and subsequent soil dry-out. Particularly in August 2021 the average soil moisture in Falkenberg reached values below 0.05 m³/m³ and responded to a rain event on Aug 23 with a sudden rise up to 0.25 m³/m³.

The mobile CRNS campaigns have been conducted 5 days before and 4 days after the mentioned rain event and clearly reflected the general increase of water content in the region. The local measurements in the area of the Falkenberg facility revealed remarkable soil moisture patterns with particularly wet spots in the north-western part of the area. These observations can be explained by a decent slope and a small water creek.

The measurements in the larger region showed a clear rewetting of the soils due to the rain event in the whole area. While the mean and the variation of soil moisture has been very low on Aug 17, the measured patterns on Aug 27 have clearly revealed hydrologically dominant flow paths and drainage patterns. The results also demonstrated that some areas in the region were able to store the added water longer than other areas (e.g., valleys and forests versus flat agricultural land).

All in all, the CRNS technique seems to be a promising tool to monitor temporal dynamics and capture spatial patterns of root-zone soil moisture in a region. The data may help to evaluate and support processes understanding in hydrological and meteorological models.

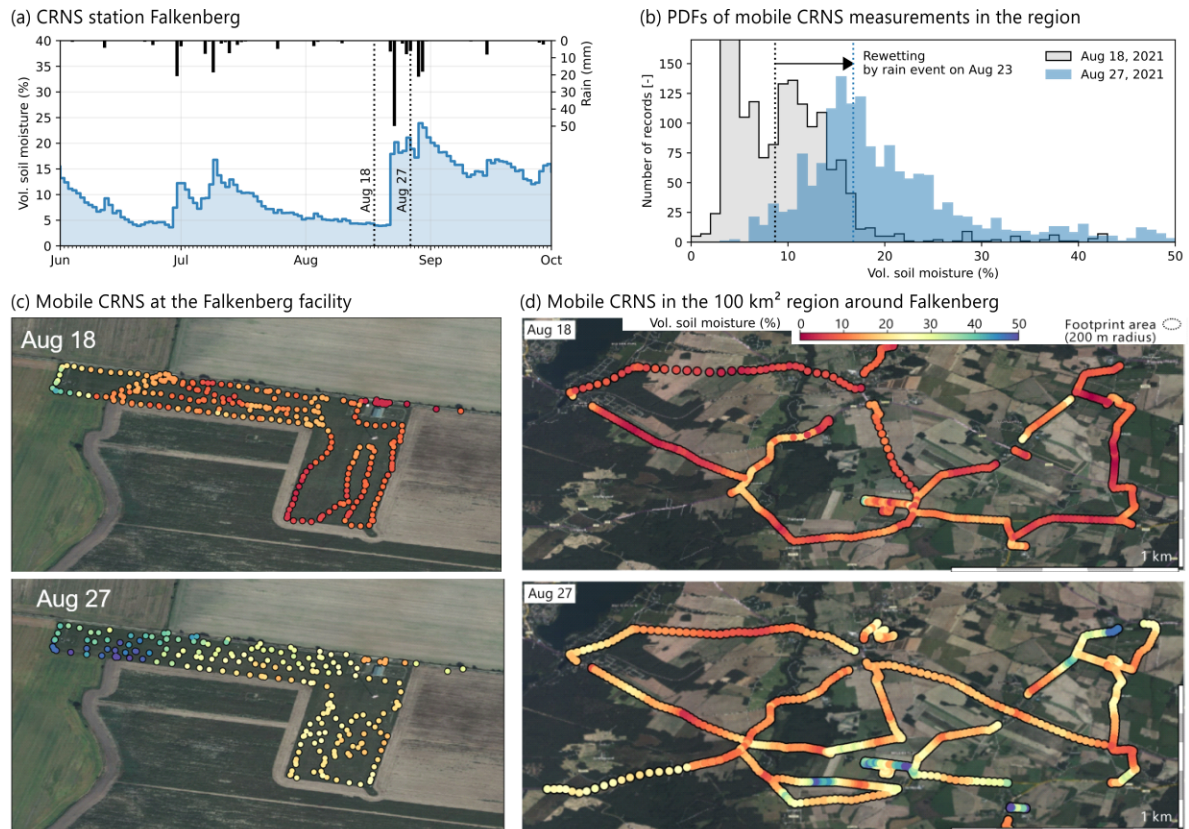


Figure 11 Cosmic-Ray Neutron Sensing (CRNS) during FESSTVal. (a) soil moisture product of the CRNS at Falkenberg, (b) probability density functions of regional soil moisture at Aug 18 and Aug 27 measured with the mobile CRNS rover, (c) soil moisture patterns at the Falkenberg facility measured with the mobile CRNS rover, (d) same as c) measured in the 100 km² region around Falkenberg (compare also b).

3.1.2 Vertical sensing of the atmosphere

3.1.2.1 Doppler lidar wind and turbulence measurements

Doppler lidar (DL) measurements were a central element of the FESSTVal experiment. Eight DL “Streamline” / “Streamline XR” manufactured by Halo Photonics Ltd. were operated in different configurations at the three supersites Falkenberg, Lindenberg, and Birkholz. Moreover, a WindCube 200S (manufactured by Leosphere) was operated at GM Falkenberg. Table 3 summarizes the basic instrumental characteristics of the different DL systems.

Table 3 Overview of basic system parameters of the DLs operated during the FESSTVaL experiment. Except for the DL89, all systems are from the manufacturer Halo Photonics. These are Streamline or Streamline XR systems. The type is indicated in the second column (Streamline – ABL, Streamline XR - XR).

DL number	XR or AGS system (for Halo Photonics systems)	Owner	Maximum range (km) (number range gates)	Sampling frequency (MHz)	Pulse length (ns)	Pulse repetition rate (kHz)	File names used in the ICDC archive
44	XR	DWD – MOL 1	12 (250)	50	401	10	sups_rao_dlidx00
74	ABL	KIT	3 (100)	50	166	15	fval_kit_dlidx00
78	ABL	DWD – MOL 2	7.5 (250)	50	180	10	sups_rao_dlidx01
143	XR	TU Berlin	12 (250)	100	352	10	fval_tub_dlidx00
146	XR	FMI	12 (250)	50	413	10	fval_fmi_dlidx00
161	XR	KIT	12 (250)	50	330	10	fval_kit_dlidx01
172	ABL	DWD – MME	3 (100)	50	214	10	sups_rao_dlidx03
177	ABL	DWD – MOL 2	12 (333)	50	180	10	sups_rao_dlidx02
89 (Leosphere)	-	DLR	2.5 5		200 400	20 10	fval_dlr_dlidppi

To ensure a certain degree of harmonization concerning the range resolution, all “Streamline” DL systems were configured with a range resolution of 30 m and a focus setting at 500 m, while all “Streamline-XR” DL systems were configured with a range resolution of 48 m and the focus set to infinity per default. Note that the resulting height resolution depends on the zenith angle which was different for the various modes of operation employed during FESSTVaL.

The DL systems were employed in FESSTVaL for different measurement tasks, this implies a different measurement configuration with respect to scan geometry, zenith angle, azimuthal resolution, pulse number, and scan duration. A summary of these settings for the different operation modes is given in Table 4. Table 5 gives an overview of the sites and configurations of the different DL systems during FESSTVaL.

For quality assurance purposes, an intercomparison experiment of the eight “Streamline” DL systems participating in FESSTVaL was organized in Falkenberg between July 16 and August 09, 2021. During this period, the DLs were operated in each of the measurement configurations realized in FESSTVaL simultaneously for a few days (see section 3.2.3).

Table 4 Measurement configuration of the DL systems

Configuration	Zenith angle (deg)	Number of pulses per ray	Number of azimuthal positions per scan circle	Duration of one circular scan (sec)	Averaging times (min)	Application
VAD24	15	30000	24	120	10, 30	Mean wind
Fast CSM	28	3000	10-11	3.4	10	Mean wind, gusts
Slow CSM	54.7	2000	ca. 240	72	30	Mean wind, TKE, momentum flux, EDR, L0
Vertical Stare	0	30000	N/A	N/A	1, 30	Vertical velocity
RHI / PPI	PPI: 89.7 RHI: 30-90	20000 / 10000	(scan sector 175°-285°)	N/A	N/A	Horizontal wind field

Table 5 Measurement configuration and sites of the DL systems employed in FESSTVaL during the period May 17 – August 31, 2021.

Doppler Lidar overview – FESSTVaL 2021: 17.05.-31.08.2021

DL	Date	from 12.05.	from 17.05.	from 18.05.	from 26.05.	from 02.06.	from 07.06.	from 11.06.	from 15.07.	from 16.07.	from 19.07.	from 02.08.	from 03.08.	from 09.08.	from 10.08.	from 12.08.	from 13.08.	from 14.08.
44			VAD-24							T3		VAD-24		CSM (gust)	CSM (gust)	T4	T5	CSM (gust)
74			T1	CSM (gust)				VS		T3		VS			VS			
78			T1	CSM (TKE)						T3		CSM (TKE)		CSM (gust)	CSM (gust)		T5	CSM (gust)
143						VAD-24				T3		VAD-6						
146			T1	VS						T3		VS					T5	
161			T1	RHI / PPI	RHI		T2	CSM (gust)	VS		T3	VAD-6		CSM (gust)	CSM (gust)			
172		CSM (gust)		CSM (gust)				CSM (gust)		T3		VS						
177			T1	CSM (gust)				CSM (gust)		T3		CSM (gust)		CSM (TKE)	CSM (TKE)		T5	CSM (TKE)
89 (Leosphere)			RHI / PPI		PPI			RHI / PPI from 10.08.										

Lindenberg - WP
Lindenberg – SMZ
GM Falkenberg
Birkholz

 Lidar Triangle 1
 Lidar Triangle 2
 Lidar Triangle 3

T1 Performance measurements; slanted stare for comparison
T2 Test CSM (gust) mode configuration on XR system before moving it to Lindenberg
T3 DL comparison campaign 16.07.-09.08.2021: VAD-24 (16.-19.07.); slanted Stare (19.-23.07.); VS (23.-26.07.); CSM TKE (26.-29.07.); CSM gust (29.07.-02.08.); from 02.08. onwards the FESSTVaL configurations were partially set again → sometimes interruptions due to other experiments (e.g. LES; hard target...)
T4 VS for ARTHUS group (only from 05:00 – 17:00 UTC)
T5 VS for ARTHUS group; LES experiment with DL78, DL146, DL177 (only from 05:00 – 17:00 UTC)

3.1.2.2 MWRP network

During FESSTVaL, ground-based microwave profilers (MWRPs) of type HATPRO (Humidity And Temperature PROfiler, Rose et al., 2005) were operated at all of the lidar profiling sites Lindenberg, Falkenberg and Birkholz and were additionally supplemented by ceilometers. These passive microwave instruments receive atmospheric radiation (expressed in terms of brightness temperature TB) in seven K-band (22-32 GHz) and seven V-band (51-58 GHz) channels of the electromagnetic spectrum. Their default observation direction is zenith, providing TBs every ~2 s, however different instruments were operated with application-dependent scanning configurations (see Tab. 6). The TBs can be used to retrieve the temperature profiles in the ABL and low-resolution water vapor profiles, but especially highly accurate path integrated values of Integrated Water Vapor (IWV) and Liquid Water Path (LWP). Azimuth scans can additionally be used to obtain horizontal inhomogeneities in water vapor and liquid water field.

Table 6 Overview of MWRP measurement set-up during FESSTVaL 2021. Images of the four MWRP systems are given in Fig. 12.

MWRP	Operator	Location	Time period	Configuration	Retrieved variables	Log interval
RAOHAT	DWD	Lindenberg	01.05.21-31.08.21	Elevation scans, alternating with zenith observations	T-profiles in ABL, LWP, IWV	T-profiles every 10 min., IWV and LWP in between every ~2s
FOGHAT	UoC	Lindenberg	06.05.21-19.08.21	Continuous azimuth scans	Line-of-site IWV & LWP @ 30° elevation	Every ~2s
HAMHAT	UHH	Birkholz	13.05.21-31.08.21	Elevation scans, alternating with zenith observations	T-profiles in ABL, LWP, IWV	T-profiles every 10 min., IWV and LWP in between every ~2s
SUNHAT	UoC	Falkenberg	03.05.21-31.08.21	Continuous elevation scans	Continuous T-profiles in ABL	T-profiles every 5 min

The RAOHAT and HAMHAT systems carried out MWRP measurements following a typical, standard operation procedure. Continuous zenith observations providing LWP and IWV every ~2s are interrupted every 10 min by elevation scans that deliver rather accurate temperature profiles in the lowest kilometer of the atmosphere (Crewell and Löhnert, 2007). The uncertainties increase from 0.2 K at the lowest levels around 50 m to about 0.8 K at 1 km height. LWP and IWV accuracies are on the order of 25 gm⁻², respectively 0.5 kgm⁻². Note that temperature and humidity profiles are also retrieved every ~2s when LWP and IWV are derived, however, with a lower accuracy.



Figure 12 The MWRPs FOGHAT, SUNHAT and RAOHAT during the common calibration campaign at Lindenberg on May 3, 2021 (left) and the MWRP HAMHAT at the Birkholz site (right).

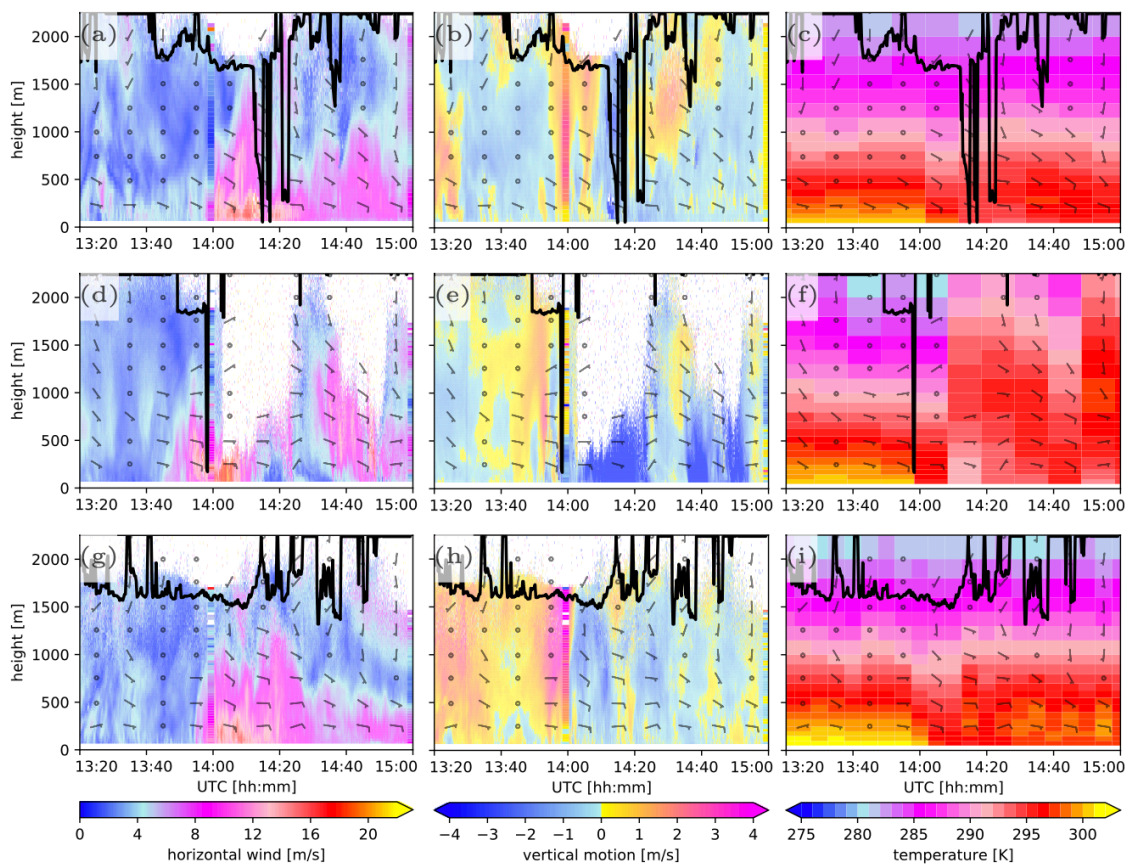


Figure 13 Profiles of horizontal wind speed (first column) and vertical motion (second) from Doppler lidars, and temperature (third column) from MWRPs on June 29, 2021 at 13:40 to 15:20. The profiles are from Lindenberg (top row), Birkholz (middle), and Falkenberg (bottom). Wind barbs showing wind direction are included every 250m/10min and the lowest cloud base height recorded by a ceilometer is indicated as a thick black line. (Figure taken from Steinheuer and Löhnert, in preparation)

The SUNHAT system carried out continuous elevation scans to ensure high-quality, continuous temperature profiles at the Falkenberg site next to the 99m tower. This proved beneficial for analyzing the passage of cold pools in the vertical dimension. A synopsis of the Doppler wind lidar and MWRP observations is given in Fig. 13 which shows the Jogi cold pool. The sudden temperature drop around 14 UTC is very pronounced close to the surface (> 5 K) and the vertical cold pool extent can be traced up to a height of more than 1 km. Fig. 13i also shows

the benefit of the continuous elevation scans for temperature profiling every 5 min by providing an improved temporal resolution compared to the other two MWRPs RAOHAT and HAHMAT. The FOGHAT system scanned continuously for 0° to 360° azimuth at a fixed elevation of 30°. From these observations, horizontal water vapor gradients have been derived and attempts to derive the water vapor advection by additionally using the Doppler lidar mean wind observations are currently being assessed.

3.1.2.3 ASSIST-II spectrometer observations and retrievals

The ASSIST-II is a ground-based infrared spectrometer, which measures downwelling infrared radiance between 3.3 and 19 μm at approximately 1 cm^{-1} spectral resolution. The temporal resolution of these data is 20 seconds. The instrument regularly observes two blackbody targets, one at ambient temperature and the other at 60 °C, which enable a radiometric calibration of better than 1% of the ambient radiance. A wide range of atmospheric variables can be retrieved from these spectra, including thermodynamic profiles, cloud properties, and more.

The ASSIST, which was provided by LRtech, was operated during FESSTVaL from 8 June to 21 August 2021 at the Lindenberg site, directly next to the RAOHAT and FOGHAT MWRP systems (see 3.1.3.2). The TROPoe-algorithm (Turner and Löhnert, 2021) was used to derive temperature and humidity profiles, as well as cloud properties, from the infrared spectra. Fig. 14 shows the passage of the cold pool Jogi on June 29, 2021 at 14:00 UTC with temperature drops on the order of 5K at the surface. Sharp temperature decreases are seen up to a height level of 1km. The high temporal resolution of the ASSIST nicely shows that the cooling starts in the upper part of the ABL and then propagates downwards reaching the surface a few minutes later.

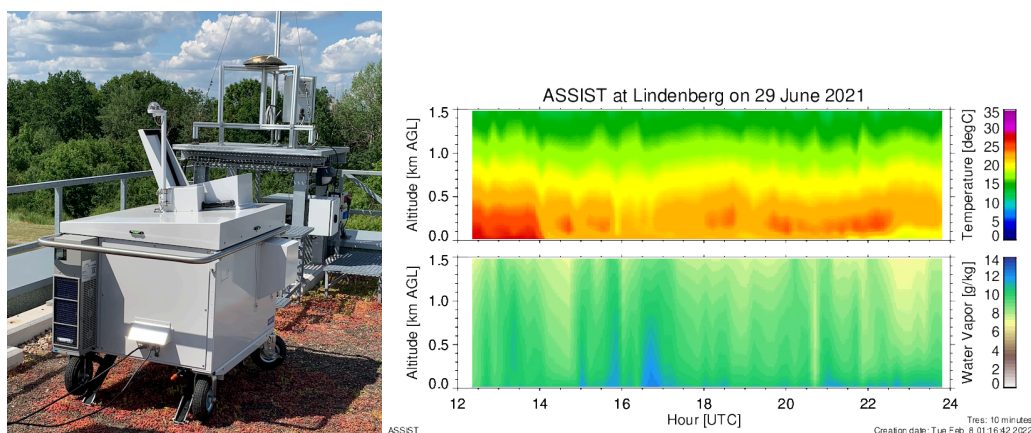


Figure 14 The LRtech ASSIST at the Lindenberg super site (left). ASSIST retrievals of temperature and water vapor on June 29, 2021, which shows the passage of the cold pool at 14:00 UTC.

3.1.2.4 X-Band radar

An X-band Doppler radar was deployed at GM Falkenberg to monitor rainfall rates at high spatio-temporal resolution, refining observations of two C-band radars of the German nationwide radar network, within a 20 km scan radius. This single-polarized, non-Doppler local area weather radar (Lengfeld et al. 2014) operates at one elevation angle of 2.3° with a 60-m range, an azimuthal sampling of 1° and a temporal sampling of 30 s. The X-band radar observations were calibrated and validated with operational micro rain radar measurements located in Lindenberg. The availability of quality- controlled data throughout the measurement period is 98.2% (Burgemeister et al., 2022).

3.1.2.5 Ceilometer measurements

Two ceilometers CHM15k (Jenoptik / Lufft) are operated at the MOL-RAO and GM Falkenberg sites. The ceilometers send short laser pulses at a wavelength of 1064 nm into the atmosphere and measure the backscattering from molecules and aerosols. From the backscatter profiles, cloud bases and aerosol layer heights are derived as 15 s averages from near the ground up to a maximum height of 15 km with a vertical resolution of 10 m or 15 m, respectively. Depending on the cloud optical thickness up to three cloud base heights can be determined. Additional parameters are the vertical visibility and the cloud penetration depth. The backscatter profiles are also very useful for estimating the mixing layer height, at least in a convective boundary layer.

Table 7 Days with MASC-3 flight measurements. The flight patterns are: lid: lidar validation flight with either 30-min flight sections at two selected altitudes or 10-min flight sections at 5-6 altitudes covering a distance of 2.5-3 km; BL: boundary layer flight with an ascent up to the top of the PBL and then a 15-min descent with level flight legs at 4-6 predefined altitudes (taken from Hohenegger et al. 2023).

Date	Time (UTC)	Flight
7 June	11:23-14:16	lid
8 June	07:26-08:56, 10:30-11:54	lid
9 June	08:39-09:51	lid
9 June	11:53-13:05	BL
10 June	07:14-08:32, 09:24-10:33, 12:13-13:30, 13:56-14:45	BL
11 June	08:29-10:01, 11:07-12:05, 17:51-19:16	lid
13 June	11:30-12:40, 13:27-14:40	lid
13 June	17:04-17:59	BL
14 June	05:05-06:05	BL
14 June	07:03-08:18, 11:57-12:58, 14:57-15:46	BL
15 June	09:23-10:36, 15:33-16:39	lid
16 June	08:41-09:44, 12:13-13:15	lid
16 June	18:00-19:30	lid
17 June	07:53-09:20, 12:11-13:02, 14:52-16:35	BL
18 June	10:36-11:42	lid
19 June	06:21-07:36, 08:23-09:05	lid
21 June	12:48-14:16	lid
23 June	08:25-09:55, 15:33-16:52	lid
24 June	08:55-10:10	lid
25 June	08:33-09:24, 10:16-11:56, 14:17-15:41	lid
26 June	06:31-08:04, 09:08-10:35	lid
28 June	14:51-15:45	lid
29 June	07:47-09:20	BL
29 June	10:05-11:20	lid
1 July	17:59-19:24	lid
2 July	09:30-11:05, 12:58-14:18, 16:53-18:00	lid

3.1.2.6 MASC-3 measurements and copter profiles

A large unmanned aircraft called MASC-3 performed 47 flights between June 7 and July 2. MASC-3 is described in Rautenberg et al. 2019. It flew in one of two flight patterns with flight duration of about 75 min each (see Table 7). MASC-3 covered a horizontal distance of 2.5 to 3 km and sampled the full PBL up to 2.5 km above the ground. The measurements by the MASC-3 were validated against the DWD operational tower measurements at 90.3 m above ground. Otherwise, MASC-3 was especially employed to validate some of the novel lidar retrieval algorithms, to characterize the vertical mean and turbulent structure of the convective PBL and to capture coherent patterns in the PBL.

3.1.2.7 SWUF-3D measurements

The SWUF-3D fleet of quadcopters UAS (Wildmann and Wetz, 2022) was operated at GM Falkenberg (Fig. 15) from 21 June to 2 July in one of five predefined flight patterns (see Table 8). Hundred twenty-four formation flights were conducted, representing 174 h of data, with a maximum of 21 drones flying simultaneously. The horizontal range of the measurements is a few hundreds of meters. A primary goal during FESSTVaL was to investigate coherence in PBL flows on the microscale, as documented in Wetz and Wildmann (2022). The fleet was operated during the cold pool „Jogi“ event on 29 June showing its applicability in such strong gust events. Some first flights were conducted for a multi-point in-situ validation of Doppler lidar VAD wind and turbulence retrievals. For this, twelve drones were placed in a VAD scanning cone. The full list of flights is presented in Table 8.



Figure 15 SWUF-3D drones next to the 99-m mast at GM Falkenberg during FESSTVaL 2021

Table 8 SWUF-3D flights. The flight patterns are: vert: vertical profile with six stationary drones on top of each other; hor: horizontal profile with several stationary drones at one height; vprof: vertical profile with one vertically moving drone; cal: calibration flight with 10 drones close to the DWD meteorological tower at the altitudes of the sonic anemometer measurements; vad: validation flight with several drones along the scanning cone of lidars. These flight patterns were associate width different mission types: stratification, targeting the thermal stratification of the boundary layer and turbulence profiles; morning transition (From night into day); coherence, with the aim to analyse spatial correlation and coherence; cold pool; lidar validation as a proof-of-concept to show that drones are a very good tool to compare lidars retrieval accuracy and calibration to calibrate the drones with the help of the sonic anemometer measurements from the meteorological tower. Taken from Hohenegger et al. (2023).

Date	Time (UTC)	Flight pattern	Mission type
21 June	15:16	vert	stratification
22 June	10:00, 10:30, 12:35, 12:54	vert	stratification
22 June	14:00, 15:40	hor	coherence
23 June	07:50, 08:35	cal	calibration
23 June	09:57, 10:20, 10:54, 12:04, 12:30	hor	coherence
23 June	14:11, 14:34, 15:04, 15:43	cal	calibration
25 June	07:13, 09:08, 09:34	cal	calibration
25 June	07:42, 08:12, 09:58, 12:00, 12:40, 13:35	hor+vprof	coherence
25 June	12:14, 12:55, 13:56, 15:53, 15:56	hor	coherence
26 June	06:57, 07:20, 09:21, 09:50	cal	calibration
26 June	08:32, 10:39, 10:42	hor	coherence
27 June	13:00, 13:10, 13:20	vert+vprof	stratification
27 June	14:09	vad	lidar validation
27 June	14:54, 15:07, 15:56	hor	coherence
27 June	15:44	hor+vprof	stratification
28 June	03:54, 04:04, 04:14, 04:25, 04:35, 04:47, 04:57, 05:09, 05:20, 05:32, 05:43, 05:54	vert+vprof	morning transition
28 June	06:06, 06:18, 06:30, 06:41, 06:54, 07:05, 07:17, 07:29, 07:40, 07:52, 08:04	vert+vprof	morning transition
29 June	03:54, 04:07, 04:57, 05:10, 05:52, 06:18, 13:51, 14:02	hor	morning transition
29 June	03:56, 04:13, 04:38, 05:05, 05:16, 05:48, 05:59, 06:21, 13:54	vprof	morning transition
29 June	04:20, 04:43, 06:04	hor+vprof	morning transition
29 June	07:30	cal	calibration
29 June	12:37, 12:39, 13:06, 13:07	vad	lidar validation
29 June	13:51, 14:05	hor+vprof	cold pool
30 June	14:57, 15:28, 17:34, 17:58	cal	calibration
30 June	16:05, 16:52, 17:05	hor+vprof	coherence
30 June	16:19	hor	coherence
1 July	06:54, 16:37, 17:05	cal	calibration
1 July	07:19, 15:38	vad	lidar validation
2 July	07:08, 09:07, 11:06, 13:22, 13:52	cal	calibration
2 July	08:02, 11:50, 12:29, 15:12	hor	coherence
2 July	08:42, 14:22, 14:48	vad	lidar validation
2 July	11:36, 12:17	hor+vprof	coherence

3.1.2.8 Atmospheric radiosonde profiles

We complemented the operational radiosoundings of DWD with additional experimental launches on days with flight operations or with forecasted thunderstorm activity in the area, see Table 9 for a list of additional soundings.

Table 9 Additional soundings.

Date	Time (UTC)	Comment
27 May	15:40	Test
8 June	16:15	Test
10 June	06:45, 08:45, 12:45, 14:45	UAS flight
14 June	06:30, 13:30	UAS flight
17 June	07:45	UAS flight
19 June	13:30	Cold pool
29 June	06:45, 08:45, 12:45, 14:00, 16:00	Cold pool
1 July	08:00	For movie making
5 July	15:21	Cold pool
9 July	13:22, 17:04	Cold pool
13 July	20:46	Cold pool
17 July	12:30	Cold pool
25 July	14:38, 16:05	Cold pool
10 August	12:30, 18:30	Cold pool
11 August	19:50	Surface inversion of nocturnal boundary layer
12 August	02:50, 19:50	Surface inversion of nocturnal boundary layer
13 August	02:50	Surface inversion of nocturnal boundary layer
17 August	13:23	Wind gust

3.1.3 MOL-RAO routine observation program

3.1.3.1 Micro-meteorological data from near-surface and tower measurements

MOL-RAO performs routine micrometeorological measurements at its boundary layer field site (GM Falkenberg) and at a forest site (Kehrigk forest) about 10 km west of Falkenberg in order to characterize the interaction between the atmosphere and the land surface for two vegetation classes typical for the region (grassland – representing low, agricultural vegetation and a pine forest). These measurements include basic meteorological variables, soil status and process variables, all relevant components of the surface energy budget and profile measurements of wind, temperature and humidity at towers up to a height of 98 m at Falkenberg and 30 m at Kehrigk forest, respectively. Table 10 gives an overview of the measured variables, measurement heights, and sensors used.

Table 10 Micrometeorological measurements at GM Falkenberg and Kehrigk forest				
Variable	Measurement Heights	Sensor	Manufacturer	Remarks
Basic meteorology <ul style="list-style-type: none"> • Temperature / Humidity • wind speed • wind direction • pressure • precipitation 	2 m (Forest: 2.25 m) 10 m (Forest none) 11.5 m (Forest 30.6 m) 1 m (Forest: 28 m) 1 m	HMP-45D F460 wind monitor PTB220A Rain[e]	Vaisala Climatronics R.M. Young Vaisala Lambrecht	ventilated
Mast / tower profiles <ul style="list-style-type: none"> • Temperature / Humidity • Wind speed • Wind direction • Turbulent fluxes 	0.5 m, 1 m, 2 m, 4 m, 10 m 10 m, 20 m, 40 m, 60 m, 80 m, 98 m 0.5 m, 1 m, 2 m, 4 m, 6 m, 8 m, 10 m 10 m, 20 m, 40 m, 60 m, 80 m, 98 m 40 m, 98 m 50.3 m, 90.3 m	HMP-45D (Frankenberger Psychrometer) HMP-45D (Thygan) F460 Wind transmitter Wind dir. transm. USA1 + LI7500	Vaisala Th. Friedrichs Vaisala Meteolabor Climatronics Thies Thies Metek / Licor	ventilated Kehrigk forest measurement heights: 2.2 m, 4 m, 9.5 m, 12 m, 14.5 m, 17.5 m, 21 m, 24.2 m, 28.3 m
Radiation <ul style="list-style-type: none"> • shortwave • longwave • surface temp. • PAR 	2 m (Forest 29 m) 2 m (Forest 29 m) 2 m (Forest 26 m) 2 m (Forest none)	CM24 DDPIR KT15.82D LI190SZ	Kipp & Zonen Eppley Heitronics Licor	ventilated ventilated
Soil <ul style="list-style-type: none"> • soil temperature • soil moisture • soil heat flux 	-5, -10 , -15, -20 , -30 , -45, -50, -60 , -90 , -100, -120, -150 cm -8 (-10), -15, -30 , -45, -60, -90 cm - 5 cm	Pt-100 TRIME EZ HP3	TMG IMKO RIMCO	bold: measurement levels Forest bold: measurement levels Forest
Turbulent fluxes <ul style="list-style-type: none"> • momentum • sensible heat • latent heat 	2.4 m (Forest: 30.6 m) 2.4 m (Forest: 30.6 m) 2.4 m (Forest: 30.6 m)	USA1 USA1 USA1 + LI7500	Metek Metek Licor	

An aerial view of the two sites is given in Figures 16 and 17. Data of the turbulent fluxes of momentum, sensible and latent heat are based on eddy-covariance measurements with a 20 Hz sampling rate, fluxes were calculated as 30-minutes averages using the EddyPro software. All other variables were sampled with 1 Hz, pre-averaged in the data loggers to 1-minute basic data, and finally provided as a quality-controlled data product for 10 minutes averaging time. Basic principles of the quality control scheme are described in Beyrich and Adam (2007).

No specific micrometeorological measurements were performed at the Lindenberg supersite. Data for some basic atmospheric variables and for the downward radiation fluxes, however, are available from two standard measurement program:

- 10-minute averages (based on 1 Hz sampling) of air temperature and humidity at 2 m (LTS2000 – Ketterer and EE33 – E+E Elektronik, both in a LAM630 screen – Eigenbrodt), wind speed and wind direction (2D sonic – Thies) at 10.4 m (on top of the winch house), pressure (PTB220 – Vaisala) at 2 m, precipitation (rain[e] – Lambrecht) at 1 m, all data are part of the measurements at the automatic synoptic weather station of DWD (WMO no. 10393)
- 1-minute averages (based on 1 Hz sampling) of the downward radiative fluxes (global diffuse, direct solar and longwave) from the BSRN station measured at the radiation platform (CMP22, CH1 and CGR4, all manufactured by Kipp&Zonen).

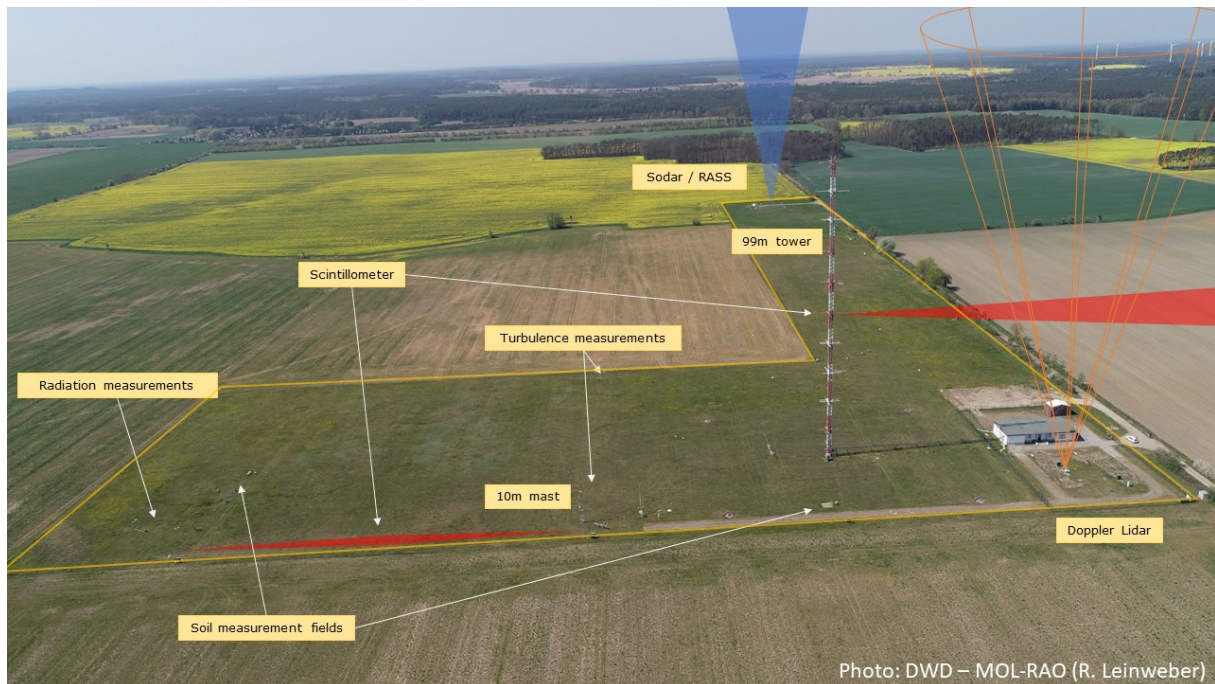


Figure 16 Aerial view of GM Falkenberg with the different measurement complexes and systems indicated.



Figure 17 The meteorological mast above the pine trees at Kehrigk forest

3.1.3.2 Scintillometer measurements

Scintillometers consist of a transmitter-receiver pair for electromagnetic radiation separated from each other by a distance of $10^2 - 10^4$ meters. While propagating through the atmosphere the emitted radiation is scattered by turbulent eddies of different density. This results in high-frequency intensity fluctuations of the electromagnetic signal (“scintillations”) recorded at the receiver. Using wave propagation theory and Monin-Obukhov similarity theory, the refractive index structure parameter of the air and the turbulent heat fluxes can be derived from these measurements. Operation of a large-aperture optical scintillometer (LAS) at wavelengths in the near-infrared allows to derive the sensible heat flux, combining a LAS and a microwave scintillometer (MWS, with mm wavelength) additionally provides the latent heat flux. The signal

at the receiver represents an integrated effect of the conditions along the path, scintillometers therefore provide area-averaged values of the turbulent fluxes. During FESSTVaL, MOL-RAO operated a BLS900 LAS (manufactured by Scintec AG) together with an MWSC-160 microwave scintillometer (RPG GmbH) between the 99m tower at GM Falkenberg and the tower at the Lindenberg observatory site over a distance of 4.8 km at an effective path height of 43 m above ground.

Data acquisition, data analysis and flux calculations were performed with the mwsc.exe software package provided by RPG. Structure parameters and the temperature-humidity correlation coefficient (rTq) for each 10min time interval have been calculated twice based on different settings, i.e. using the methods described in Hill (1997) which assumes a constant $rTq = -0.6$ at night and $rTq = 0.8$ during daytime and in Lüdi et al. (2005) which calculates rTq from the cross-correlation of the optical and microwave signals. The similarity model proposed by Kojimans and Hartogensis (2016) was then used to derive the heat fluxes from the structure parameters. Using temperature and humidity profile measurements at the Falkenberg tower and measurements of the radiation budget, the deduced fluxes have been checked for sign consistency with the mean gradients of temperature and humidity and for a violation of the energy budget. In the end “most plausible” fluxes from the two methods (Hill, Lüdi et al. – see above) have been merged to a composite to ensure a better availability / quality of the fluxes especially around sunrise and sunset when the assumptions of the Hill approach typically fail.

3.1.3.3 Additional measurements

In addition to the measurements characterized in the previous sections, the following measurement systems are operated at MOL-RAO on a routine base, data from these systems are available for FESSTVaL:

- 482-MHz radar wind profiler: vertical profiles of wind speed and wind direction between 0.5 km and 9.3 km (with 250 m vertical resolution, low mode) and between 5.5 km and 16 km (with 500 m vertical resolution, high mode) as 30-minute averages
- MIRA-36 cloud radar: vertical profiles of radar reflectivity, Doppler velocity, spectral width and Linear Depolarisation Ratio between 0.15 km and 15 km agl (with a vertical resolution of 30 m) as 10 s averages
- Cloudnet (synergy product mainly based on measurements of a cloud radar, a microwave radiometer and a ceilometer): vertical profiles of target classification, liquid and ice water content, between 0.2 km and 15 km, cloud base / top height as 30-s averages
- MRR micro rain radar: vertical profiles of radar reflectivity, fall velocity, drop size distribution and rain rate for droplet sizes between 0.2 mm and 6 mm for a vertical range between 0.1 km and 3 km as 1-minute averages
- IRCCAM and CamLum: total cloud cover and cloud cover for low-, medium-, and high-level clouds based on hemispheric mirror / camera images
- Different Spectro-Photometers (Cimel CE 318T, PMOD-WRC PFR, Prede POM, MFR SR): aerosol-optical depth (AOD) for different wavelengths, single-scattering albedo (SSA), total precipitable water vapour (PWV).

3.2 Field campaign Overview

3.2.1 Weather conditions

The weather conditions during the FESSTVaL period showed the full range of typical weather patterns for mid-latitude summertime conditions. During the entire 103 day period, the targeted processes occurred as follows: 32 days with cold pools, 20 days with wind gusts, 55 days with low-level jets, 8 days with almost no cloud and 30 days with cloud-topped boundary layer.

In the last week of May, numerous showers drifted over the region. In the first week of June the weather was largely friendly, which was caused by a stable high over Scandinavia. The "SOP" (special observation period) of the experiment started on June 7, 2021. At the beginning of the week, the weather conditions were primarily summery and characterized by a stable high. On June 12 there was a cold front passage with heavy cloud cover and rain. The second week of the SOP started with a blue sky and no rainfall in sight. In the next few days, it got warmer, up to very hot days on weekends, thus atmospheric turbulence. In particular, on June 19^h and 20 there were thunderstorms in the region - visible in the distance. With air temperatures of about 35 °C the air was moist-warm and unstable, yet the rain in Lindenberg remained absent. Week three of the SOP was volatile. At the beginning it was hot and sticky with a tendency to thunderstorms. In the course of the week, it cooled down a bit and there was also thick cloud cover with almost no wind. The first Cold Pool, who made it entirely to our measuring area, occurred on Tuesday, June 29 and was named Jogi. At the end of the SOP (until July 2) and the beginning of week 8 there was again drizzle. The next days followed with rain and gray in gray, until July 9. Several cold pools, accompanied by hail and turbulence, moved over the region. Week 9 started with summery weather and harmless cumulus clouds. In the course of Tuesday evening, however, a thunderstorm front was brewing southeast of the campaign region and there was a thunderstorm impact exactly over the measuring devices at the MOL-RAO and in the vicinity. At the end of July, a few days lined up that were meteorologically, from FESSTVaL's point of view, rather unspectacular. The weather was mostly calm, with loose to closed cloud cover and moderate wind speeds.

The 12th week of the measurement campaign rain persistently evaded the region, even when a front ran through. As a result, some heavy rain showers affected the region indirectly, as they at least had an effect on the temperature at the measuring locations. In week 13 two cold pools occurred at the beginning of the week. Both were poorly forecasted by numerical weather prediction models and characterized by sharp temperature reductions, the onset of rainfall, and an increase in near surface wind speed. The rest of the week until August 15 was comparably calm, dry, and warm due to a semi-stationary high-pressure system that determined the local weather conditions. Largely cloud-free conditions led to ideal conditions for the development of a stably stratified nocturnal boundary layer in two consecutive nights. The surface inversion in the first night was unusually strong for this time of the year. We have seen nocturnal low-level jets, although with relatively low wind speeds in their jet core due to the weak horizontal pressure gradient. In the fourteenth week, there were two weather extremes to be observed. At the beginning of the week, a storm low from Scandinavia reached the area, with cold and humid air. It brought numerous heavy wind gusts with it. At the weekend, a low-pressure area followed, which brought a large amount of rain with it from Saturday evening: 65 mm fell in 14 hours. This heavy rain led to numerous minor floods in the region and significant puddling.

3.2.2 Quality assurance activities

3.2.2.1 MWRP calibration

The EUMETNET project E-PROFILE and the European Research Infrastructure for the observation of Aerosol, Clouds, and Trace gases (ACTRIS), both supported by the COST action PROBE (PROfiling the atmospheric Boundary layer at European scale) currently focus on establishing continent-wide quality and observation standards for MWRP networks for research as well as for NWP applications. Due to the four available MWRP systems, activities carried out during FESSTVaL could actively contribute to these European objectives by developing, applying and recommending procedures for calibration and error characterization that can be applied to any HATPRO network instrument. A "COST Virtual Mobility Grant" carried by Tobias Böck of the University of Cologne was used to draft the document "HATPRO MWR Uncertainty Assessment" available through www.probe-cost.eu.

During FESSTVaL, TB errors of different HATPRO generations were investigated and characterized by means of systematic differences (bias) between collocated HATPROs, calibration repeatability, long-term drifts, and radiometric noise. From these errors sources, a total maximum error (TME) per channel has been proposed. It consists of the sum of the mean biases, mean repeatability, noise at the hotload target and optionally a mean or absolute drift over a certain time. Without the drift, the experiments have shown that such a TME can reach 0.4 K in the K-band and up to 1.1 K in the lower (optically thinner) V-band channels. With drifts included, TMEs can be as high as 0.6 K in the K-band and range from 1.3 to 2.3 K in the V-band. If the Observation minus model Background (O-B) values per channel are consistently higher than the TMEs, it is proposed to take action, i.e. a new calibration should be performed. A total minimum error consists only of the calibration repeatability and the radiometric noise, assuming all systematic errors have been accounted for. For all channels this error was shown to lie well below 0.5 K, which is the absolute calibration error according to the HATPRO manufacturer RPG (Radiometer Physics GmbH).

3.2.2.2 Doppler lidar intercomparison

After the end of the FESSTVaL IOP, all 8 StreamLine Doppler lidars were set up in two rows at GM Falkenberg near the 99m tower to perform comparison measurements for quality assurance (see Fig. 18). The setup covered 4 Halo Photonics StreamLine XR systems (hereafter often referred to as XR) and 4 Halo Photonics StreamLine boundary layer systems (hereafter often referred to as ABL systems). During the experiments, which were performed from 16.07. to 09.08.2021, several questions were investigated:

- Can the manufacturer's specifications for the systems (e.g. pulse width and pulse repetition rate) be reproduced?
- How do the actual measurements (level-1 data, i.e., profiles of backscatter intensity and radial velocity) compare between the different DL systems and operation modes?
- Do possible differences have consequences for our retrieved products?



Figure 18 Setup of the Doppler lidar intercomparison experiment at the boundary layer field site Falkenberg (Photo by F. Beyrich)

In a first step, optical power measurements were performed on all systems to verify the pulse length and the pulse repetition frequency (PRF). The results of the measurements and the resulting pulse shapes can be seen in Fig. 19. The PRF corresponds to the value given by the manufacturer for all devices and the pulse length also agrees quite well. For the ABL systems (upper row) there are deviations of up to $\pm 7ns$, for the XR systems (bottom row) these are up to $\pm 17ns$. The manufacturer's specifications could thus basically be reproduced.

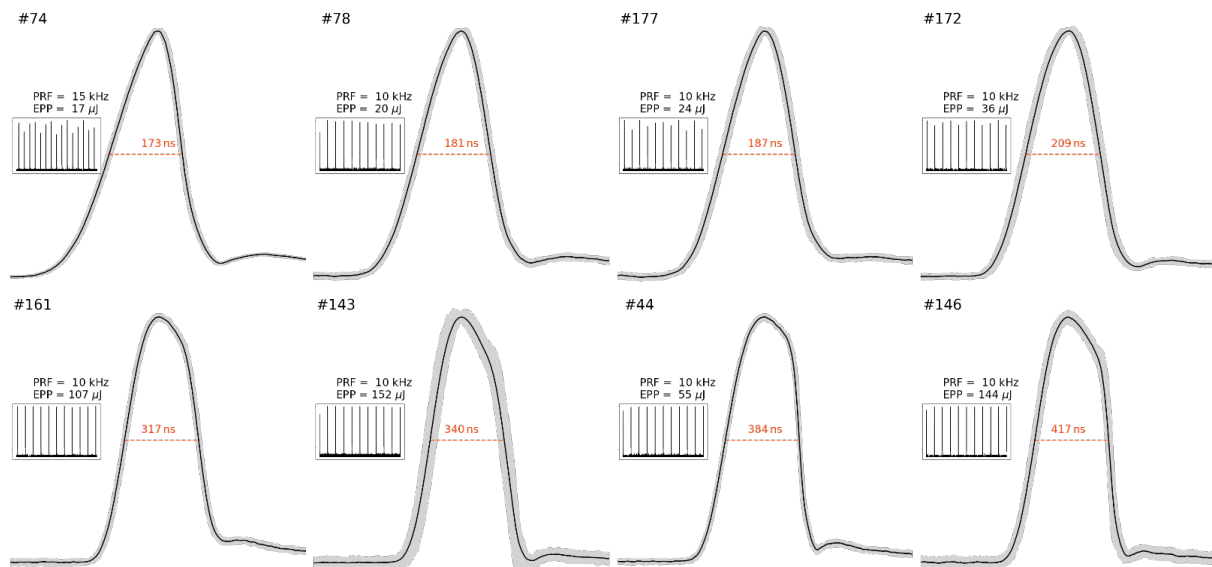


Figure 19 Measured Doppler lidar characteristics of the eight Halo Photonics systems. The upper row shows all the ABL systems and the bottom row the XR systems which were operated during FESSTVaL in summer 2021. Shown are the pulse shapes with the related pulse length and the calculated pulse repetition frequencies (PRF). (Figure by Markus Kayser)

Furthermore, all systems were operated simultaneously in each of the configurations applied in FESSTVaL for 2-3 days. First examples of measurement results based on a slanted stare configuration of each of the DL systems are presented. The focus is initially only on a representation of the basic output (e.g. radial velocity, intensity) of the DL system. A detailed in-depth analysis of the intercomparison experiment for the derived data products has to be the subject of further (future) work.

In a slanted stare experiment, profiles of backscattered signal intensity and radial velocities were recorded based on emission of 30000 pulses per ray. A low elevation angle (5°) was used to measure inside the ABL so that a high and nearly homogeneous aerosol density can be assumed over large distances. This was necessary in order to be able to precisely analyze the ranges of the individual DL systems. Figures 20 and 21 provide time-height diagrams of the two basic output variables for the eight systems on July 22, 2021. For the presentation of the radial velocity profiles a standard SNR-filter has been applied in order to illustrate the range limitations of the different systems. For signal intensity, the XR systems show a gradual decrease of the signal intensity with range due to the focus setting to infinity. DL #44 and DL #146 have the strongest signals in the near-range (note that these two systems operate with the largest pulse length), DL #143 has a significantly weaker signal. For the ABL systems, the focus setting to 500 m becomes clearly visible. The general time evolution with maxima between 04 and 05 UTC and before midnight is consistent between the systems except for DL #74 which shows a different behaviour. DL #177 exhibits a rather narrow region of strong backscatter with the maximum clearly below 500 m. Also, the signal decreases more rapidly with height when compared to the other systems (darkest blue in the upper part of the diagram), this has consequences for the range over which valid radial velocities are derived if a fixed SNR threshold is applied (see Fig. 21), which is the lowest for DL #177 (except for DL #74 which obviously suffered from some instrumental problems). From a purely visual point of view the general behaviour of the radial velocities over time and range is quite consistent between the other seven systems. The intensity, however, plays an important role in estimating the measurement uncertainty. Hence it has yet to be analyzed in more detail to what extent the differences in the intensity would eventually contribute to differences in mean profiles of wind and turbulence (e.g. gust, TKE) variables and its uncertainty estimation.

First conclusions from the intercomparison experiments can be summarized as follows:

- The manufacturer's specifications of the systems (pulse length and pulse repetition frequency) could be reproduced.
- The two groups of systems (XR and ABL) show similar results for the tested measurement configurations within one group, but differ from each other.
- The use of classical SNR filters in slanted stare mode leads to different availabilities in height
- DL74 behaves differently from the other systems in all tested configurations and should not be taken into account in further analyses due to obvious instrumental issues.

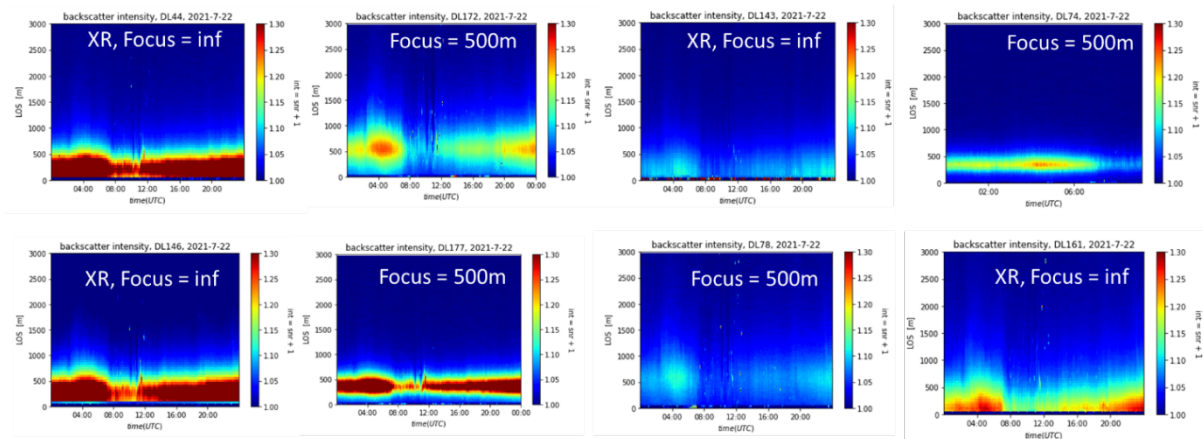


Figure 20 Time-height diagrams of the recorded signal intensity for the eight StreamLine DL systems simultaneously operated in a slanted stare mode (elevation angle 5°, 30000 pulses/ray) at GM Falkenberg on July 22, 2021

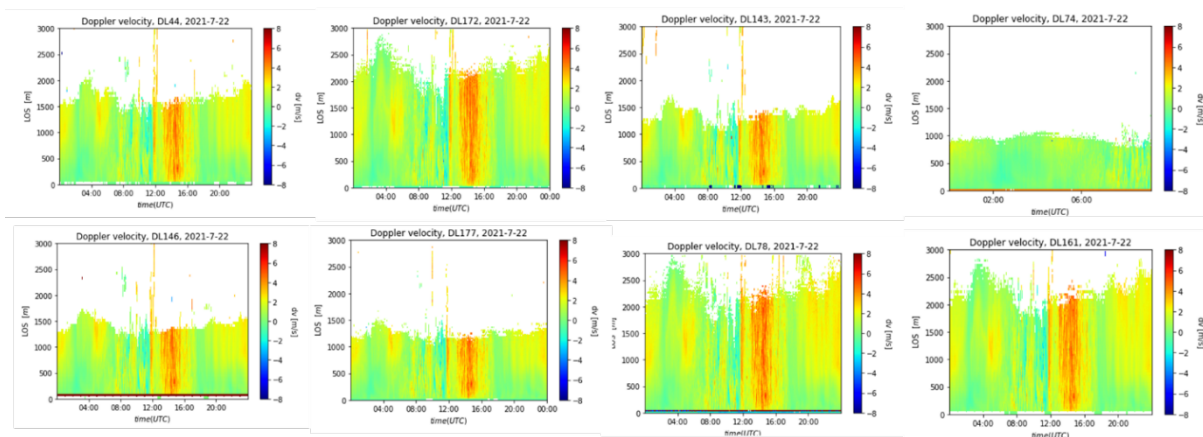


Figure 21 As Figure 20, but for radial velocity after application of an SNR threshold filter using $SNR_{\text{thresh}} = -18.2\text{dB}$ (intensity = 1.015)

3.3 First results and current status of the data analysis

3.3.1 Boundary layer patterns

3.3.1.1 Doppler lidar TKE retrieval

FESSTVaL had set a scientific focus on deeper insights into the connection between the character and intensity of turbulence and sub-mesoscale motions during the diurnal cycle of ABL evolution. Essential variables of interest are the turbulent kinetic energy (TKE), the eddy dissipation rate and turbulence length scales. A suitable approach to provide a self-consistent dataset of these variables based on DL measurements is the method proposed by Smalikho and Banakh (2017). It relies on a work by Kropfli (1986) where the focus was on the determination of TKE from radar measurements. When transferring the approach to DL measurements Smalikho and Banakh (2017) suggest additional correction terms for both the underestimation of TKE due to pulse volume averaging effects (σ_t^2) and an overestimation due to the instrumental error of the radial velocity estimation (σ_e^2). These corrections require a special measurement strategy, i.e., conical scans with a high azimuth-temporal resolution (< 2 deg, < 5 s). In FESSTVaL the method proposed by Smalikho and Banakh (2017) (SB hereafter) has been implemented and tested for routine 24/7 measurements to enable a continuous monitoring of the boundary layer up to 500m height. It quickly became obvious that increased efforts were necessary in terms of a pre-processing of the measured data to minimize noise contamination. Otherwise, large errors in the derived products were to expect (see sections 2.3.2.4 for more details).

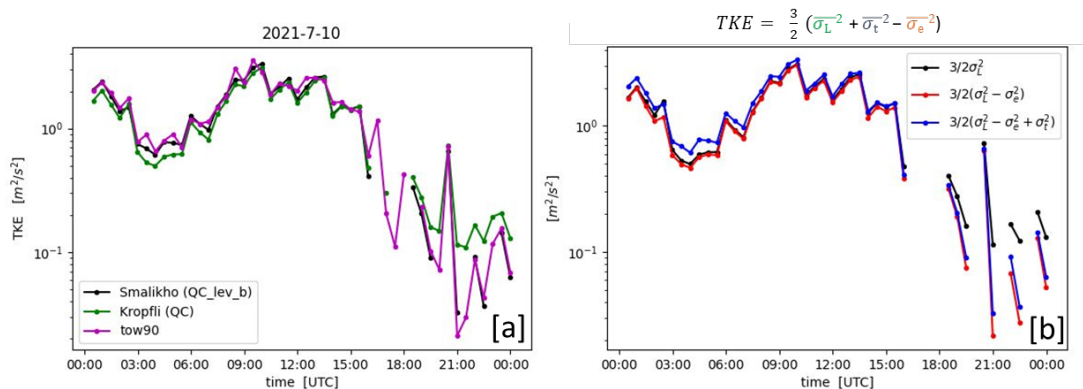


Figure 22 (a) Comparison of TKE from Doppler lidar with sonic TKE at a measurement height of 90m for July 10, 2021. Two results from two retrieval methods are presented for the TKE obtained from DL, namely the Kropfli (1986) method and the method proposed by Smalikho and Banakh (2017). (b) Effects of the single corrections proposed by Smalikho and Banakh (2017) taking into account averaging effects over the DL pulse volume (σ_t^2) and instrumental error effects (σ_e^2).

Provided that instrumental noise can be filtered effectively and a sufficient number of reliable data is available after filtering for a derivation of turbulence variables, the corrections introduced by the SB method yield reasonable results. This is illustrated in Fig. 22 using the example of a DL TKE retrieval for July 10, 2021 in comparison to independent sonic measurements at 90m height on the meteorological tower at GM Falkenberg. Comparing the results of the Kropfli approach (i.e., $TKE = 3/2 (\sigma_L^2)$) with those of the SB method (i.e., $TKE = 3/2 (\sigma_L^2 - \sigma_e^2 + \sigma_t^2)$) it becomes clear that, especially in the early morning hours, the underestimation of TKE is reduced (Fig. 22a) by means of the correction term σ_t^2 (Fig. 22b). This underestimation of the TKE by the Kropfli method seems to be plausible having in mind that at night turbulent eddies are of limited size. These were obviously not fully resolved by the DL system due to the pulse averaging effect. On the contrary, a higher uncertainty in the radial velocity estimates seemed to be the bigger problem in the evening and night hours, leading to a larger

overestimation of TKE by the Kropfli method. With a reasonable estimate for σ_e^2 this was corrected by the SB method.

Good results of the SB method can be proven not only for one day, but for the entire FESST-VaL period. This is demonstrated in Fig. 23. Here, only TKE results that passed an additional quality control (QC) are included in the graphs. As part of the QC, it is checked whether certain theoretical assumptions, underlying the TKE reconstruction method by BS, are fulfilled. Best possible agreement between DL and sonic TKE is achieved if these assumptions are strictly met (indicated by QC: flag_lev_a in Fig. 23). In this case, however, the availability of reliable TKE values is comparably low (43.6 %). Further analysis revealed that the agreement between sonic and DL TKE data deteriorates only moderately if some of the QC test criteria are formulated less strict (mean = - 3.6%, limits of agreement = +34,3% /- 41%). At the same time the data availability increases significantly (to 83,9%). Therefore, the data products made available as part of the FESSTVaL data set contain two quality flags (flag_lev_a, flag_lev_b) which should be selected depending on the users' data quality requirements.

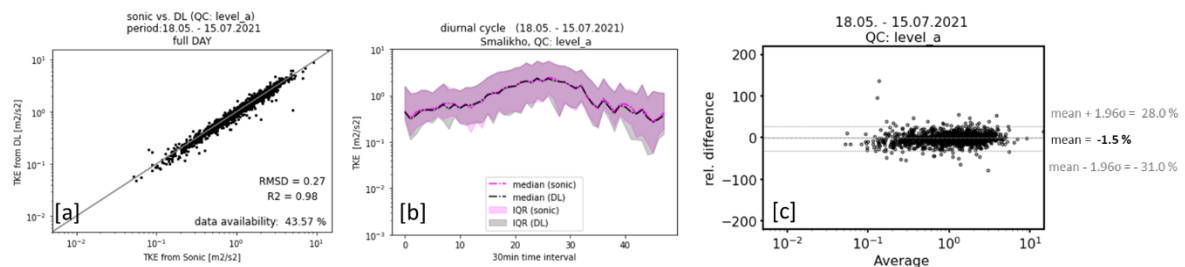


Figure 23 Comparison of TKE from DL with sonic measurements at 90m height for the measurement period 18.05. – 15.07.2021. (a) The scatter plot and (c) the Bland-Altman plot show the extent to which 30min averaged TKE measurements agree. The x(y)-axis labels in (c) are defined through Average = (DL+sonic)/2 and rel_difference = (DL-sonic)/sonic * 100%. The horizontal lines in (c) indicate the mean relative differences (mean) and +/- two standard deviations (1.96 σ) of the mean as statistical limits of agreement. (b) A comparison (sonic vs. DL) of the average (median) daily TKE over the entire measurement period. The shadowed regions around the median mark the interquartile range (IQR) of the half-hourly daily measurements over the entire measurement period.

Plots of daily TKE profile data show prominent features during the diurnal cycle which are consistent with common understanding of the ABL structure. An example is given in Fig. 24 where 30min averaged DL wind and TKE profiles are shown for June 17, 2021 (Fig. 24a,b). The first obvious phenomenon is the mechanically induced TKE due to shear below the axis of a low-level jet (LLJ) occurring at around 300 – 400 m at the beginning of the day. Furthermore, the typical development of the boundary layer can be seen in the evolution of TKE over time (Fig. 24b). It starts with the morning transition between the stable nighttime ABL and the daytime convective boundary layer (CBL). It can be seen that about two hours after sunrise TKE values start to increase in the lower layers, which reflects the onset of the boundary layer growth. In the further course, enhanced TKE values are observed over an increasing height range, i.e., the morning growth phase of the CBL is reflected in the profiles. This is followed by a longer period of vertically almost homogeneous TKE profiles representing the well mixed ABL during day characterized by vigorous turbulence and comparably weak winds. Finally, an LLJ forms again after sunset, and the associated mechanically induced TKE values superimpose the effect of the decay of atmospheric turbulence in the evening boundary layer around sunset, which is nevertheless discernible between 300 and 600m.

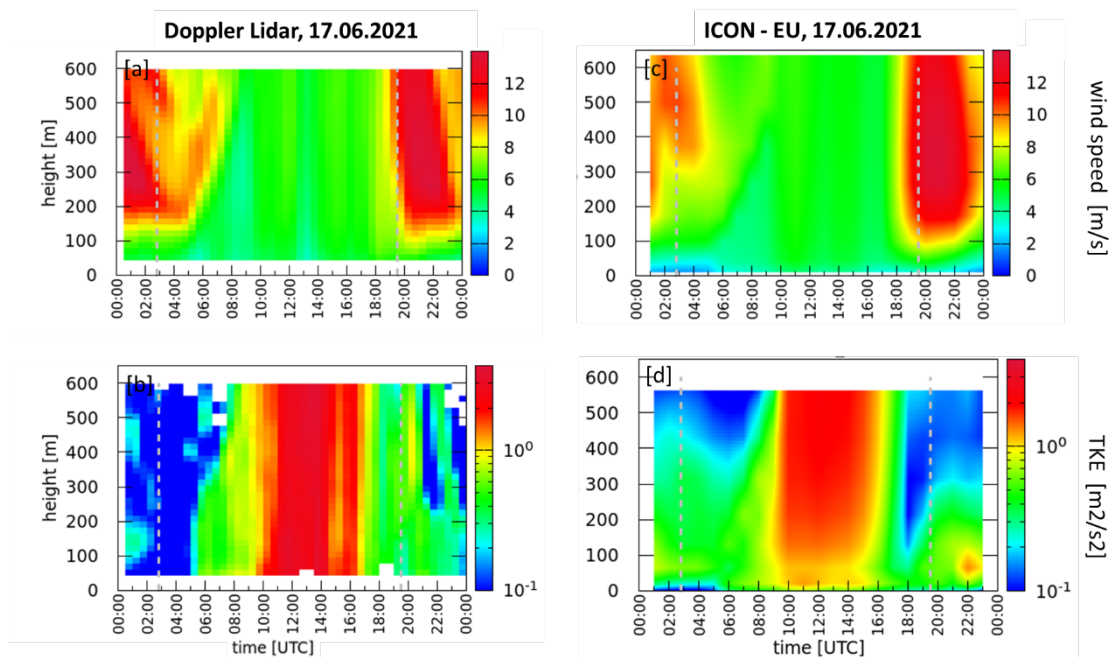


Figure 24 Comparison of DL wind and TKE time-height cross-sections (a,b) for June 17, 2021 with corresponding simulations obtained with ICON-EU (c,d).

We compared these measurements with the output of the operational NWP model ICON-EU. In the ICON-EU model (with a horizontal grid spacing of $\sim 7\text{km}$) turbulence is fully parameterized. Fig. 24d shows good agreement in general, but it also reveals possible deficits of the model parameterizations. The modeled wind shear-induced TKE below the LLJ in the early morning is too high and its position does not match the observations while the LLJ was modeled too weak (Fig. 24c). Discrepancies between the position of the LLJ and the shear-induced TKE can also be observed in the evening. Inside the daytime mixed layer observed TKE values exceed the modelled ones. Moreover, there is a kink in the modelled TKE profiles in the lowest layers which is not present in the observations. Finally, it is worth to point out that finer structures can be seen in the DL measurements, so that the measurements would also be suitable for validating model simulations with smaller grid spacing. In these cases, however, it must be taken into account that modelled turbulence is not only represented via the parameterizations, but is also partially resolved explicitly on the computational grid. This requires a particularly careful preparation of the TKE data from model simulations in order to carry out a reliable comparison with DL measurements. Further work on a DL – ICON model intercomparison with respect to TKE in the lowest 500 m is planned.

3.3.1.2 Vertical velocity statistics

Higher-order vertical velocity statistics are investigated to study the characteristics of turbulence in the convective boundary layer. The vertical velocity was measured using Doppler lidar operated in the vertical stare mode during the FESSTVaL campaigns. The collected data were categorized into clear-sky days and cloud-topped days. The mean of σ_w^2 profile was compared to the Lenschow et al. (1980) profile as a reference (Fig. 25). Moreover, the dependence of the σ_w^2 profile on the meteorological parameters was investigated. The σ_w^2 was calculated from the raw data at 1.5s and 3s resolution and averaged to 30 min. The σ_w^2 profiles were normalized by the convective velocity, w_*^2 . The height is also normalized by the boundary layer height. For the analysis, the σ_w^2 profile is averaged daily from 10UTC to 15UTC.

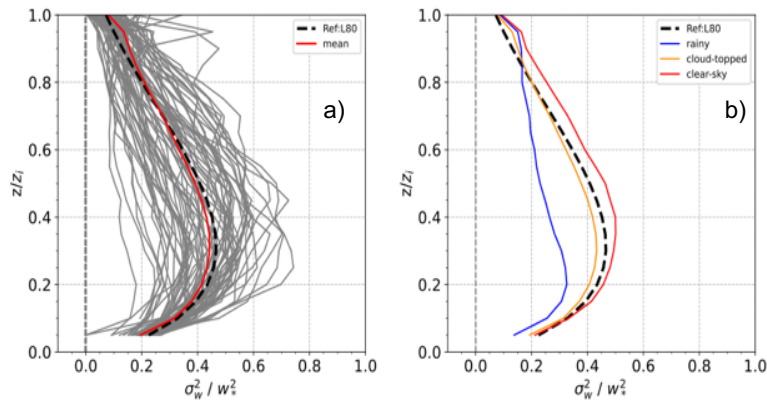


Figure 25 (a) Mean profile (red line) of the vertical velocity variance of all selected clear-sky and cloud-topped days compared to the profile of Lenschow et al. (1980) (black dash line) with daily averages of individual days (grey lines); (b) mean profiles of the clear-sky days, cloud-topped days and rainy days.

The mean of the σ_w^2 profile of all selected days is similar to the reference profile as shown in Figure 25a. However, the variability of the daily average of the individual day is still large, meaning that the scaling velocity w_*^2 does not account for all the relevant factors that control the vertical motion in the convective boundary layer. Therefore, the dependence of the σ_w^2 profile on the meteorological parameters was investigated for clear-sky and cloud-topped days. Figure 25b shows that the magnitude of the mean of the σ_w^2 profile in the clear-sky days is higher than cloud-topped days. Additionally, the mean of the selected rainy days is added for the comparison to show that rainy days have the lowest magnitude of σ_w^2 .

In the clear-sky days, the σ_w^2 profile shows two regimes based on the year of measurements (Fig. 26). The magnitude of σ_w^2 in 2020 is higher than in the 2021 dataset. This result is attributed to the difference in the surface Bowen ratio. In the 2020 dataset, the Bowen ratio is higher compared to the 2021 dataset. This signifies that the moisture flux from the surface plays a role in setting the strength of circulations even in the cloud-free days, although we have not yet explained the exact mechanism behind this finding. We also found that the profiles of the normalized variance measured during the cloud-topped days is dependent on the Bowen ratio, cloud fraction, latent heat flux and relative humidity in the boundary layer.

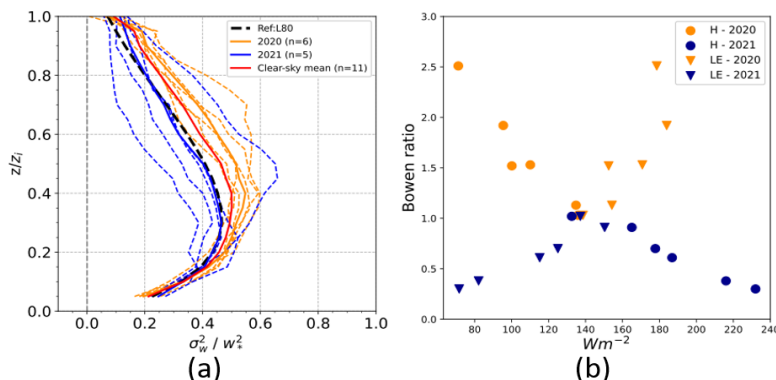


Figure 26 (a) Profiles of the vertical velocity variance in all the observed clear-sky days; (b) Comparison of the surface sensible heat flux (dot) and latent heat flux (triangle) in 2020 (orange) dataset and 2021 dataset (blue).

3.3.1.3 Assessment of nocturnal low-level jets during FESSTVal

NLLJs are a common phenomenon during summer in the Lindenberg area, as seen in measurements during the FESST@home campaign 2020 (Luiz & Fiedler, 2022) and the FESSTVal campaign in 2021. The number of nights with NLLJs during both years was similar in the two summers, with 2021 having ~13% higher LLJ profile frequency than 2020. The three super-

sites (Lindenberg, Falkenberg and Birkholz) had a similar frequency of LLJs in 2021, with 20-23% of all available profiles. When accounting only for nocturnal profiles (solar height $< 20^\circ$), the frequencies were higher, which shows the higher probability of having LLJs during nocturnal stable stratification. From all the LLJs profiles in Falkenberg, we observed a co-occurrence at the other two sites in about 75% of cases. Restricting the analysis to events longer than 3 hours, the co-occurrence was larger (84%). This is consistent with the larger spatial extent of longer events, more likely driven by inertial oscillations, while short LLJ events can be associated with smaller scale convective events or are affected by local conditions. LLJs longer than 6 hours happening during night-time were classified as nocturnal LLJs (NLLJ). They were found in 25% of the summer nights. From all profiles classified as a NLLJ in Falkenberg, 74% happened during an average increase of the temperature with height, in agreement with the requirement for an inertial oscillation. Figure 27 shows an example for the vertical gradient in the temperature from the microwave radiometer in Falkenberg and the wind profiles from Doppler wind LIDARs at all three super-sites, where we can see the NLLJ presence and the nocturnal stable stratification of the surface layer.

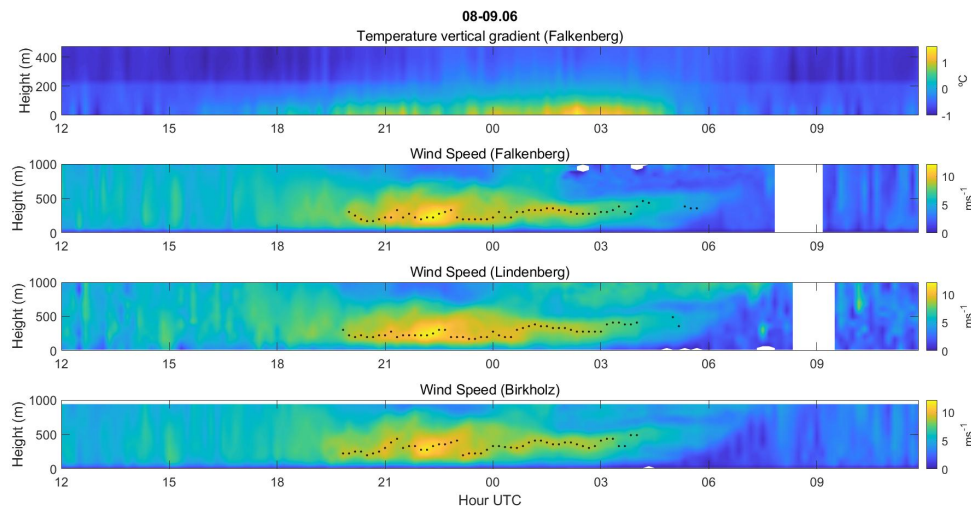


Figure 27 Vertical temperature gradient and wind speed profiles in Falkenberg, Lindenberg and Birkholz during the NLLJ event of 08-09 June 2021. The black circles mark the LLJ from the automated identification, following the method described in Luiz and Fiedler (2022).

The FESSTVal dataset was also a unique opportunity to analyse LLJs connected to cold pool events. During the campaign, about 4.7% of all LLJ profiles in Falkenberg were connected to a cold pool event (CPLLJ). CPLLJs were shorter than NLLJs owing to the fact that they are connected to cold pools, which are generated by downdrafts from deep convective clouds. Differently from NLLJs, which are favoured by anticyclonic weather patterns (Luiz & Fiedler, 2022), CPLLJs happened mainly during the influence of low-pressure systems, since they require convective instability that allow the development of deep convective clouds.

3.3.2 Cold pool

During FESSTVal we were able to observe 42 cold pool events listed in Figure 28a. As depicted, most cold pools were detected by numerous stations, which enables us - for the first time - to picture the spatial structure and its evolution in detail (s. example of Cold Pool Jogi, Fig. 28b). The data set of quality-controlled APOLLO/WXT station network measurements is published and fully documented by Kirsch et al. (2022b). Scientific data analysis in the third HErZ phase was focused on the morphology and growth of cold pools. For a complete documentation of all results, we refer to the dissertation Kirsch (2022), in particular to the paper draft in Annex C, which is submitted in a revised version in summer 2023 for publication in QJRMS. Here, we will just briefly present selected key findings.

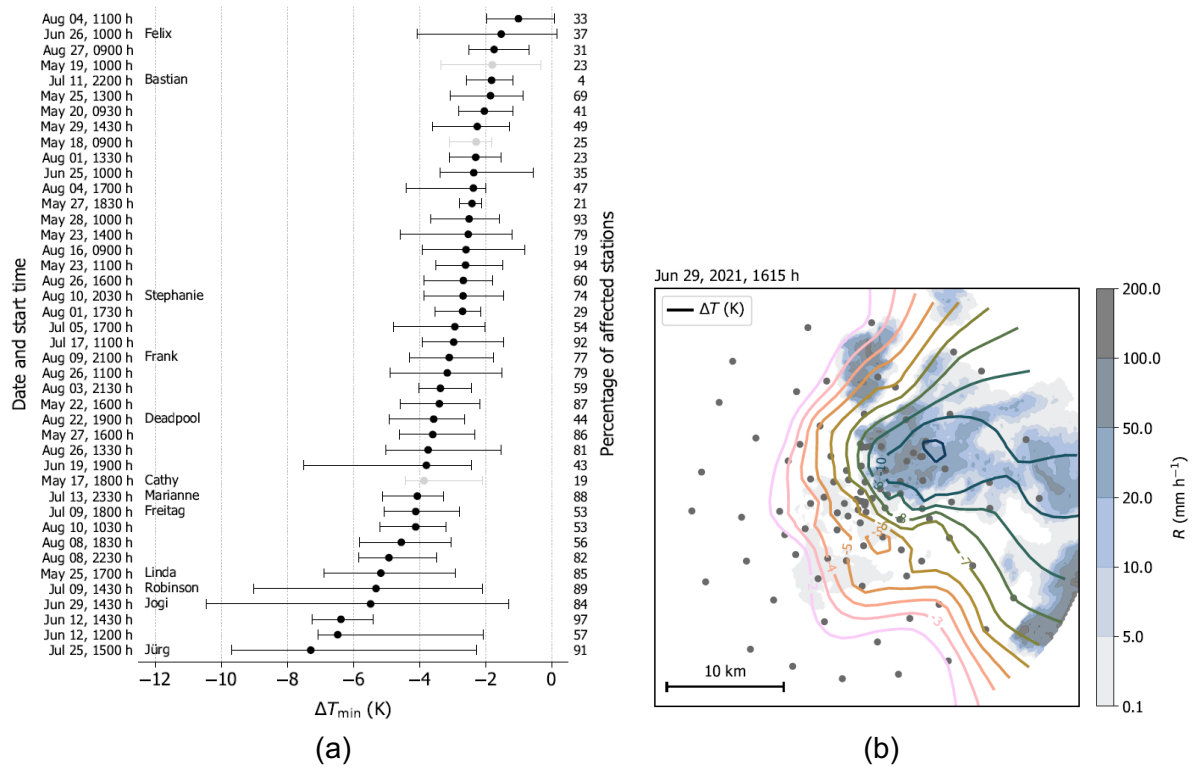


Figure 28 (a): Cold pools detected APOLLO and WXT stations during FESSTVaL sorted by the median (black dots) of strongest detected temperature perturbation ΔT_{\min} . Indicated are also the start time of the events in local time (UTC+2), the percentage of all 99 stations that have experienced a cold pool passage, and the names given to selected events. (b) Spatially interpolated temperature perturbation ΔT (colored isolines) observed by the FESSTVaL station network (gray dots) and radar-measured rainfall rate R (blue shading) during cold pool event Jogi on June 29, 2021 at 1615 h local time (UTC+2)

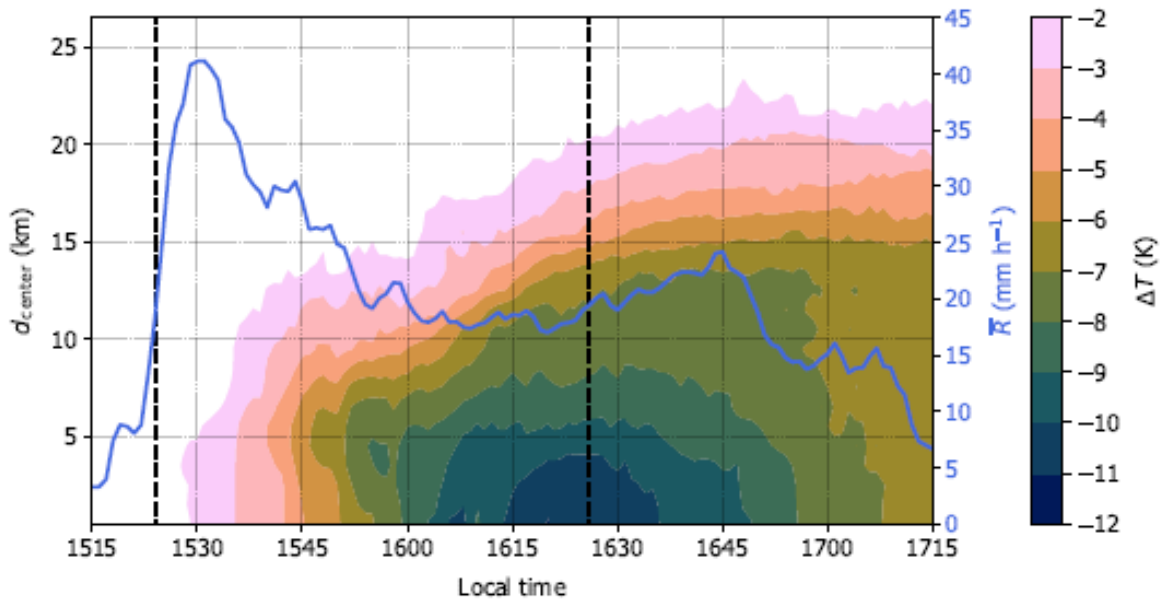


Figure 29 Time series of temperature perturbation ΔT dependent on distance to cold pool center for event Jogi on June 29, 2021 (local time = UTC+2). Blue solid line indicates the mean radar-observed rainfall rate for $R \geq 0.1 \text{ mm h}^{-1}$. Dashed vertical lines mark the begin and end of the growth phase analyzed in Figure 30.

Cold pools feature a cold core. As shown for the case of the cold pool event Jogi (Fig. 29), the temperature perturbations increase almost linearly with decreasing distance to the cold pool center. Thus, bigger cold pools are colder. This rule and the linear structure are also common to the other analyzed cold pools. However, cold pools are typically not round but exhibit an aspect ratio in the order of 1.6 (not shown). We hypothesize that the shape is strongly determined both by the wind field and the structure of the rain field feeding cold pools with cold air. As long as it precipitates, cold pools grow fast and quickly reach a size which cannot be captured completely by our observational network with a diameter of just 30 km. Additionally, cold pools are advected by the mean wind and likely travel outside the observational domain.

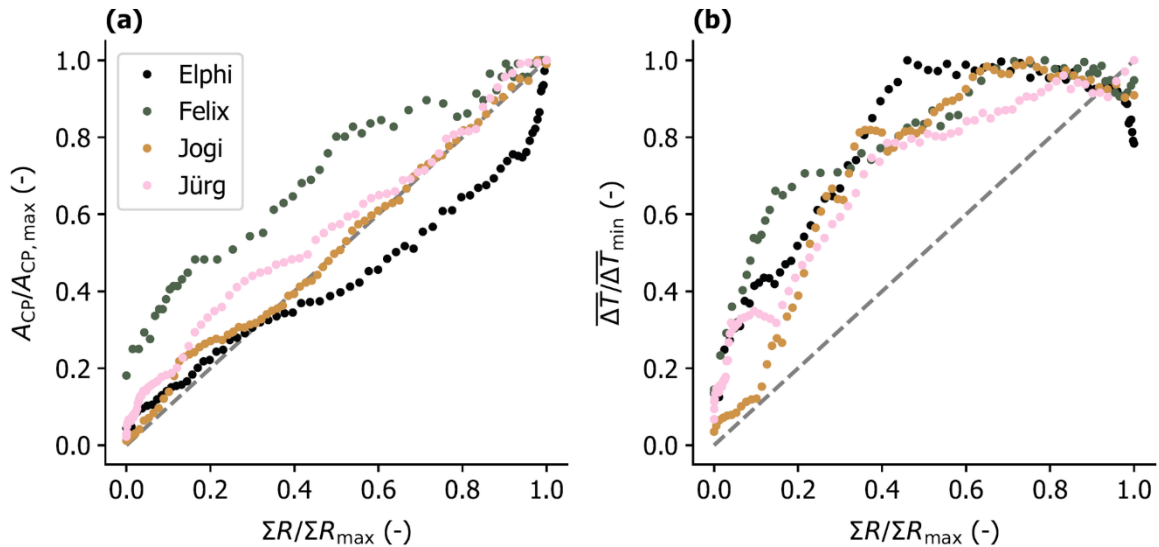


Figure 30 (a): (a) Cold pool area A_{CP} and (b) object-mean temperature perturbation ΔT dependent on area-integrated accumulated rainfall amount ΣR during the growth phase of cold pool events Elphi (FESST@HH), Felix, Jogi, and Jürg. The minimum–maximum range of all quantities is normalized between 0 and 1 per event.

As a consequence, we limit our analysis of temporal evolution to the initial growth phase of young pools. We identified four cold pools which developed mostly within our observational domains (Fig. 30). Surprisingly their growth in terms of cold pool area scales very well with the total accumulation of rain water (Fig. 30a). We hypothesize that the volume of cold air generated by precipitation - both by evaporation and down-mixing of cold air - is the dominant driver for cold pool expansion. Dynamics in the height of the cold pool or purely density driven flows seem to be of minor relevance. The cooling efficiency is highest in early growth phases (Fig. 30b), which indicates that the increasing ambient humidity slows down the evaporation rate during the cold pool life cycle.

Jointly with the group of Sue van den Heever (Colorado State University), we have started to analyze the spatial and temporal cold pool evolution using spatial variograms. Preliminary analysis for both model simulations and observations indicate that variograms are very well suited to describe the change in near surface temperature variability caused by cold pools. We will further elaborate this approach and intend to prepare a joint publication.

3.3.3 Wind gust

One of the key tasks of FESSTVaL was to gain a better process understanding of wind gusts, specifically considering their vertical structure and their horizontal propagation. For this purpose, Doppler wind lidars (DWLs) were used, since Suomi et al. (2017) showed that the determination of wind gusts with a DWL is possible with high accuracy. Their results were based

on two days of measurements by a Windcube V2 DWL manufactured by Leosphere. Streamline DWLs from the company Halo Photonics were available for FESSTVaL. Since the Doppler beam swinging (DBS) configuration used by Suomi et al. (2017) could not be used in a similar way with these systems, other configurations had to be tested and thus other derivation methods had to be developed. Thus, different DWL configurations were tested and analyzed during preliminary experiments (2019) and the FESST@MOL campaign in summer 2020, as the Streamline DWLs offer a wider range of configuration possibilities than the Windcube V2 from Leosphere. However, a suitable measurement mode was found for the detection of wind gusts and operated almost continuously at all three sites (Lindenberg, Birkholz, Falkenberg) during the FESSTVaL campaign in summer 2021. This configuration is a quick continuous scanning mode (CSM), that completes one DWL head circulation in 3.4 s while it measures in 11 different directions. A detailed description of the tests performed in 2019 and the evaluation of the tested configuration in 2020 can be found in Steinheuer et al. (2022).

As a reference for the evaluation of the DWL measurements, data from the meteorological tower at 90.3 m were collected using an ultrasonic anemometer manufactured by Metek (USA-1). These are very high temporal resolution (20 Hz) measurements of the individual wind components, from which, following a quality check, both the mean wind (10 min mean) and the maximum gust of each interval are determined. The maximum wind gust is defined as the maximum value of a 3 s moving average within a 10 min interval (WMO,2018). The quality assessment is based on the study by Vickers and Mahrt (1997). A more detailed description of the sonic anemometer data can be found in Steinheuer et al. (2022).

Two independent retrieval algorithms have been developed for the determination of wind gusts from DWL measurements (Steinheuer et al., 2022; Detring et al., in prep.). For the wind derivation from DWL measurements, a filtering of the data is usually conducted in advance. Filtering by signal-to-noise ratio (SNR) is often used to distinguish between trustworthy and erroneous radial velocity estimates (noise) (Schween et al., 2014; Päschrke et al., 2015). Data filtering primarily based on an SNR-threshold was shown to be inappropriate for the fast CSM due to the low number of pulses per ray (3000). This would have resulted in the rejection of too many reliable single measurements which are needed to identify gusts. Thus, two new methods were developed independently of each other.

The approach by Steinheuer et al. (2022) has the following data processing steps: Instead of filtering the measurements in advance, a method is developed that initially includes all measurements but then iteratively filters out those measurements that deviate significantly compared to an intermediate fit solution such that they are detected as noise. This ensures that enough data are available to derive a high-resolution time series of the wind, and, in particular, the wind gusts. Simultaneously, the iteration incorporates thresholds that terminate the retrieval procedure if the set of measurements is too inconsistent and conditions prevail under which the wind vector cannot be derived. The complete iteration procedure is explained in Steinheuer et al. (2022). It can be applied either to a set of measurements within 10 minutes or only the 11 measurements of one single DWL revolution. The first yields the 10 minutes mean wind, while from the latter, the maximum wind gust is calculated when enough of the single revolution winds are retrieved (i.e. at least 50 %).

In the method proposed by Detring et al. (in prep.), prior to the wind gust retrieval, a filter has been applied to all radial velocity estimates of a measurement interval to separate reliable from noisy data. This filtering is done in two steps and each in different coordinate systems. Latter allows a different perspective on the measurement data and thus different possibilities for data analysis w.r.t noise detection. In a first step a coarse filter is used to obtain a kind of first guess for reliable measurements. This filter works using the VV90D perspective, where the time series of measurements from a conical scan is plotted against the same measurement series but with a phase shift by 90 degree. Using this perspective, measurements from conically scanning DWLs show a circular structure, reminiscent to a harmonic oscillator. An individual analysis of subsets of the whole measurement series confined to different circular rings in the VV90D plane reveals noise in the form of singular points which is exploited in the coarse filter to re-

move noisy measurements. This approach, however, is only successful if the DWL noise resembles white noise. By operating the DWL with small number of pulses frequently another second type of noise distribution characterized through a pronounced aggregation of noise values around zero has been observed. In such a case the noise removal is made possible by an evaluation of the autocorrelation function (ACF) of circular ring related subsets of the whole measurement time series. This approach exploits the fact that the autocorrelation function can provide valuable information about the general existence of nonreliable radial velocity estimates in noise contaminated measurements. Eventually, having once a first guess for reliable measurements, in a post processing step a second filter uses the first guess information to fully capture all good measurements. This filter works using the well known VAD (velocity azimuth display) perspective. One major difference to the method according to Steinheuer et al. (2022) is that the filter method works without an a priori estimate of the wind variability which is used in Steinheuer et al. (2022) to define thresholds that terminate the retrieval procedure. In general, it can be concluded that the two methods differ in their approach. In Steinheuer et al. (2022), 10 min intervals and measurements from single DWL head circulations are processed independently of each other while in Detring et al. (in prep.) a filtering in advance for both products is conducted at once.

Figure 31 shows the results of the sonic anemometer compared with the DL measurements in scatterplots for the entire FESSTVaL period (17.05. - 31.08.2021 with a measurement interruption from 16.07.-10.08.). Both retrievals are considered for the mean wind as well as for the maximum identified gust. In order to draw a conclusion about the quality of the derived values from the DWL, the root-mean-squared-difference (RMSD) and coefficient of determination (R^2) are calculated. The retrievals come to similarly good results for the mean wind. The R^2 value for both methods lies at a very high value of 0.98. Slight differences can be seen in the RMSD (Steinheuer: 0.34 m/s, Detring: 0.32 m/s), which, however, provides a very good result for both methods. At this point it should be mentioned that more data points are included in the comparison when considering the Steinheuer's method. The data reduction in Detring's method could be related to the relatively strict quality criterion that was chosen. Here, all intervals are discarded in which less than 60% data are available and the $ACF < 0.75$.

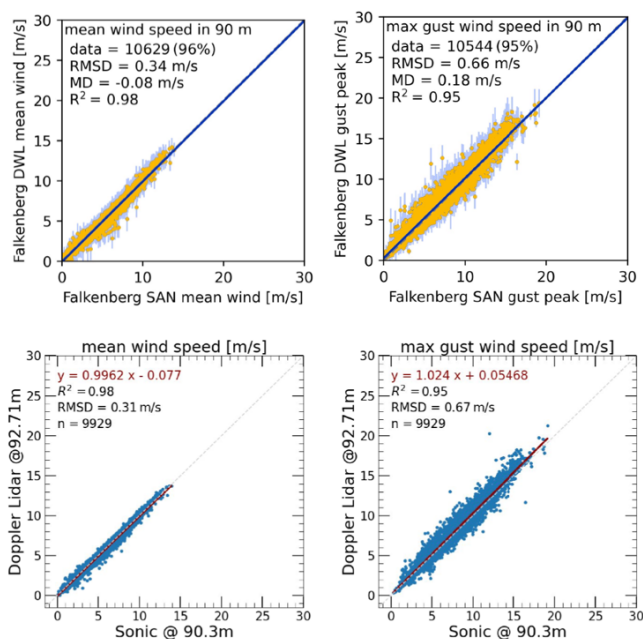


Figure 31 Scatterplots of sonic anemometer vs DWL wind retrievals during the period 17 May to 31 August 2021 at 90.3 m. (upper row) processing from Steinheuer et al. (2022) with estimated DWL standard deviation of the horizontal wind or gust peak shown by vertical bars. (bottom row) processing from Detring et al. (in prep.). Left column shows comparisons for the 10 min mean wind and right for the maximum gust speed.

Similarly good results can also be achieved for the identified gusts from the two methods compared to the sonic anemometer. The R^2 is 0.95 in both cases and the RMSD is 0.66 m/s (Steinheuer) and 0.67 m/s (Detring). The spread of the values is greater for the gusts than for the mean wind. This, however, is not too surprising since here measurements from different measurement systems with different underlying measuring principles (point vs. volume) are compared. Larger deviations are expected here, but they are still within reasonable limits. A slight tendency of overestimation by the DWL can be seen with both methods. Validations at higher altitudes are still required. Since the occurrence of noise increases with increasing height, the robustness of the different approaches will be revealed here. But nevertheless, reasonable profiles of the mean wind speed and the gusts can be produced.

Time-height plots for retrieved wind and gusts from the two different approaches are shown in Figure 32 for 29 June 2021 (day of cold pool "Jogi"), respectively. The upper row represents the mean wind and the lower row the maximum gust at the Falkenberg site. Consistent structures can be identified for both methods. It becomes evident that Steinheuer's method yield a higher vertical availability. For the mean wind, in both methods, at least 1000 m and for the gusts at least 500 m of the lower part of the atmosphere can be covered continuously. It is noticeable that although Steinheuer's method produces more data, these appear to be more erroneous at the edges of available data and that there are more mean wind speeds determined which have values close to zero. To what extent these values are plausible still needs to be investigated. It is known that some DWLs occasionally detect a second signal around zero in addition to valid measured values, which can lead to such erroneous values. Especially in situations of low winds Steinheuer's retrieval struggles with distinguishing between actual wind signal and this noise signal close to zero. Detring's data processing tries to account for that by discarding such data in the data filtering.

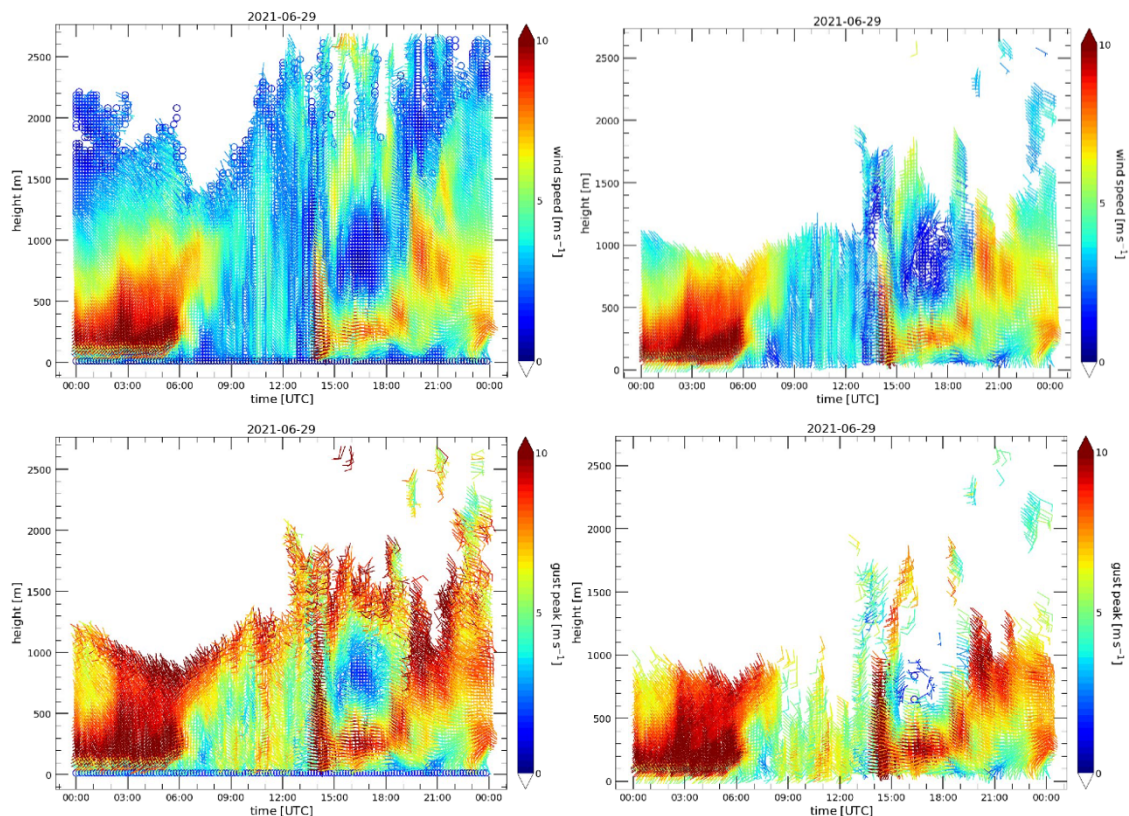


Figure 32 Upper row: 10 minutes mean wind speed and bottom row maximum wind gust speed for 29 June 2021. On the left column are shown the results from the Steinheuer retrieval and on the right column from the Detring retrieval.

Figure 33 shows time series of the mean wind and gust speed at a height of 90 m agl as derived from the DL measurements at the three supersites. A strong sudden increase in mean wind speed and gusts of more than 20 m/s were derived in connection with the cold pool "Jogi" at around 14 UTC. With the thunderstorm propagating from SE towards NW thereby hitting Birkholz and Lindenberg, while no precipitation occurred in Falkenberg, the strong winds first occurred in Birkholz. In Falkenberg, the maximum gust speed was weakest.

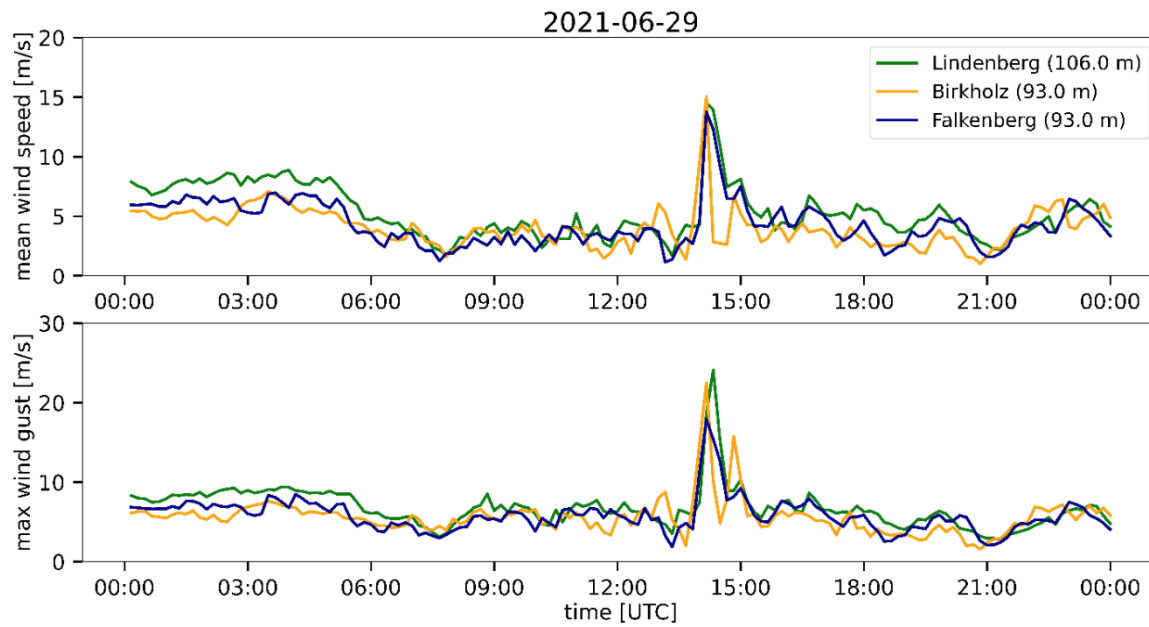


Figure 33 Time series of wind from DWL measurements at a height of about 90 m at the sites Falkenberg (blue), Birkholz (yellow) and Lindenberg (green) from 29 June 2021. A strong increase in mean wind speed (top) and maximum gusts (bottom) can be seen during the Cold Pool event "Jogi" around 14 UTC.

Figure 34 shows a further look into cold pool Jogi by collocating wind and temperature measurements. At Birkholz, the cold pool was registered first at 14:00 UTC as indicated by the temperature drop throughout the lowest 500 m (panel f) and the preceding strong horizontal winds beginning at 13:45 (panel d). Here, the cold pool is accompanied by rain leading to a strong attenuation of the lidar signal shortly after 14:00 from 400 m upward. The cold pool hit Falkenberg (g) and Lindenberg (a) with gust fronts up to 1000 m and remarkable amounts of lifting especially in Falkenberg (pink area in panel h). While Falkenberg remains dry, small amounts of precipitation fell in Lindenberg (blue area with cloud base drop at 14:15 UTC in panel b). While the heavy precipitation leaves a wet MWR radom that yield a useless temperature profile in Birkholz after 14:10 UTC (panel f), clear drops in the whole temperature profiles are apparent at the other two sites, with warmer temperatures above colder, indicating the cold pool outflow that lifts the ambient air.

Overall, it could be shown that with two different retrievals wind gusts can be derived from DWL measurements, which provide valid results at a height of 90 m, comparable to the gusts from in-situ measurements. The evaluation of the high-resolution time series can additionally produce profiles of the wind, which can contribute to the understanding of the process and adds a new facet for future measurement campaigns, since such a high resolution has not been achieved before.

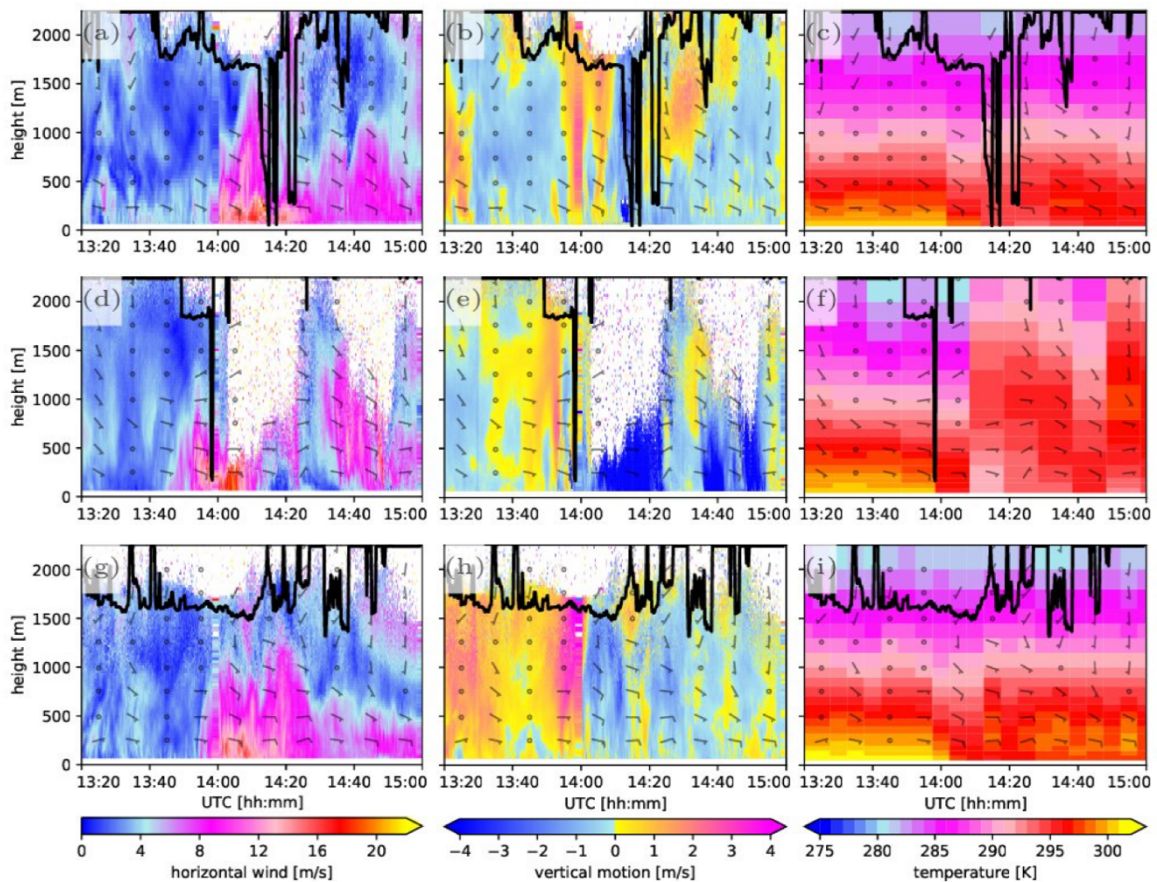


Figure 34 (same as Fig. 13 – shown again for better readability of the report): Profiles of horizontal wind speed (first column) and vertical motion (second) from DWLs, and temperature (third) from MWRs on June 29, 2021 at 13:40 to 15:20. The profiles are from Lindenberg (top row), Birkholz (middle), and Falkenberg (bottom). Wind barbs showing wind direction are included every 250m/10min and the lowest cloud base height recorded by a ceilometer is indicated as a thick black line. Cloud base heights exceeding the image section (which is up to 2250 m) are indicated by a horizontal line at the top of the panel.

Further validation of the two methods at higher altitudes should be carried out. For this purpose, the measurements of the UAVs can be considered. Intercomparison measurements at a different location with a meteorological tower with sonics at higher altitudes would also be beneficial. In addition, further analyses of gusts in both spatial and vertical propagation are planned. The DWD is also pursuing the goal of testing and analyzing the identified measurement mode for wind gusts over a longer period of time.

3.3.4 Citizen Science

The first goal of the citizen science project was to analyze to what extent low-cost internet-of-things-based measurement devices deployed (and partly built) by citizens can be integrated into a professional measurement network and thus enhance station density.

The data collected using the MESSI devices needs some amount of postprocessing before it allows for actual scientific findings. Obvious reasons are a) the low successful data transmission rate (60%) and b) the only passively ventilated radiation shield. As described above, we recovered most of the missing data from the flash memory of the MESSI after the campaign and transferred it to the database to make the data set as complete as possible. This was followed by an outlier detection to find and eliminate data from malfunctioning sensors. For subsequent campaigns involving the MESSIs we improved the protection of sensors using

other protective coating. Furthermore, from MESSIs co-located with reference instruments from DWD and FU Berlin, we developed a calibration function meant to compensate effects from insufficient (passive) ventilation. It turns out, that a piecewise linear function involving the temperature sensors inside and outside the housing were very effective to reduce systematic errors of the temperature measurement due to insufficient ventilation. A more elaborated calibration function is based on a Generalized Additive Model using inside temperature, the difference between inside and outside temperature, as well as light intensity; all quantities required were measured directly by the MESSI.

Another challenge is the unfixed location of the devices. MESSIs are identified with their hardware ID. If a device at a given location needs to be exchanged due to a failure, the same location has a device with another ID. During the transport, devices do also change location or are stored indoors. This is being solved by defining one fixed MESSI (with ID) for each position where there was a device for a fixed minimum amount of time. We define gaps in measurements when the MESSI was not at the respective position.

When all the steps described above are finished and documented, the actual data analysis begins. This will include different geostatistical models using the preprocessed MESSI data and also a merged data set of MESSI and Apollo data. First attempts with a simple ordinary Kriging model show that it is possible to visualize the movement of the cold pool Jürg on a map- using only the MESSI data (Fig. 35). When combining MESSI and Apollo data we need to account for potentially different biases of MESSIs and Apollos.

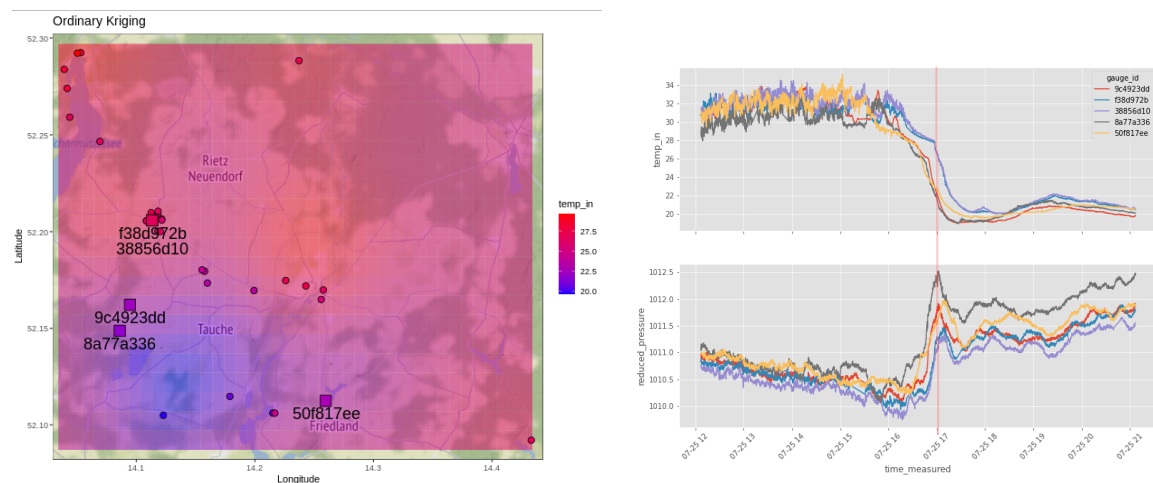


Figure 35 Left: An ordinary Kriging model derived from MESSI data set at 2021-07-25 17:00 (CEST). Right: Timeline of highlighted devices indicating movement of cold pool Jürg.

The amount of necessary interaction with citizens was challenging at times given the small human resources available.

The second goal was to investigate if the involvement of citizens in weather research is helpful for their understanding of the concept of uncertainty in measurement and consequently in prediction, communicating weather related risks and promoting weather related research. This was investigated by answering two questionnaires. 60 (32) people answered the pre-(post-) survey, i.e. not completely the same sample. A first block of questions asked for the expected weather in July to test their climatological knowledge before the campaign, and in the post-survey, the same questions were asked about the July weather they remembered. In the pre-test most people realistically judged the expected (i.e. climatological) frequency of days with thunderstorms or the nightly minimum temperature, but strongly overestimated the number of hot days. The latter were still overestimated in the post-test, but less so compared to the pre-test. The second block of questions tested their knowledge about weather forecasts and weather risks. Participants moderately underestimated the probability of forecasts missing thunderstorms and they strongly underestimated the probability of false alarms (similar to a study of a representative German sample, Fleischhut et al. 2020). Various risks associated

with heat and severe precipitation were correctly judged by most of the participants. Less so for thunderstorms (e.g. a third strongly underestimated the distance of a thunderstorm, given the time between lightning and thunder; furthermore, most didn't know that lightning can strike up to 10 km away from a thunderstorm). A third block of questions tested the knowledge of observed climate change in Germany. There was a good knowledge about temperature related changes, but less so about precipitation and storm strength, again similar to the study of Fleischhut et al. 2020.

Finally, another set of questions evaluated the success of the campaign. 92% found participation (very) interesting before and 78% after the campaign. 2/3 experienced assembling the MESSI as easy, 1/3 as moderately difficult. Most of the participants found supporting texts and video on the website understandable. Many participants would recommend to participate in future campaigns. The survey participants were asked to describe in their own words what they liked most and least about the project. What they liked most was: having their own instrument and being able to view the measurement data; the active research and the knowledge they gained by participating in the project; comparing the measurement data with the weather; getting help from the MESSI team; assembling the device; the web app. What they liked least was: technical (mainly data transmission) problems; poor quality of the components; a lack of comparison with other MESSI stations; the assembly; the short measuring phase.

4. Modeling

4.1 Modeling strategy

The observed sub-mesoscale variability of the turbulence and convection in the atmospheric boundary layer (ABL), cold pools, winds, surface radiation and a multitude of measurement methods and strategies make FESSTVaL a unique campaign particularly suitable for the development, testing and evaluation of the parameterization schemes in the NWP models that use challenging kilometre-scale grid spacing. These are the intermediate scales where mesoscale processes are starting to be partially resolved by the models and where the spatial variability of turbulence, convection, land surface processes, radiative and exchange surface fluxes can no longer be neglected. The advantage of FESSTVaL is not only in the high spatiotemporal resolution and combination of the measurement methods, but also the characteristics of the measurement site located in low-level terrain with varying land cover types and vegetation.

A modelling framework is set up to accompany FESSTVaL using different modes of the Icosahedral Nonhydrostatic model (ICON; Zängl et al., 2015): the large-eddy simulation mode (ICON-LES; Dipankar et al., 2015), the numerical weather prediction in a limited area mode (ICON-NWP/LAM), and single-column mode (ICON-SCM; Bašták Ďurán et al., 2021). The group of Wageningen University will contribute with very high-resolution LES with 3D radiation computations with the MicroHH model (van Heerwaarden et al. 2017).

The hierarchy of elliptical modelling domains is centered around the Lindenberg-Falkenberg measurement site: the four LES domains of about 75, 125, 300 and 600 m grid spacing, and the three NWP limited-area domains of about 1.2, 2.5 and 5 km grid spacing (Figure 36). The axes of the innermost LES domain are about 22 (N-S) and 24 km (E-W), while the outermost NWP domain is about 547 (E-W) km wide. The LES simulations are forced by the ICON-D2 operational forecasts at about 2.2 km resolution, while the NWP simulations are forced by the ICON-EU forecasts at about 6.5 km resolution. The setup of the simulations, including the grids, external static data, the forcing data and the available model output are temporarily stored at the German Climate Computing Center (DKRZ, levante.dkrz.de:/pool/data/fesstval) for the entire FESSTVaL measurement period and will be published as a long-term open-access archive at the DKRZ World Data Center for Climate (WDCC). The forcing data for all modelling configurations are available for the entire FESSTVaL measurement period.

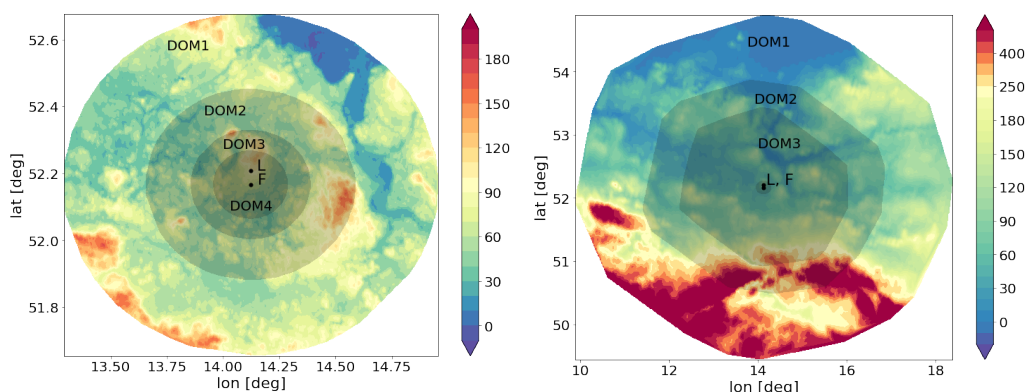


Figure 36 The ICON-LES (left) and ICON-NWP/LAM (right) modelling domains overlaid over the orography map representing height in meters.

Based on the availability of the ABL measurements during the FESSTVaL campaign, we have selected seven example case studies representing typical weather conditions, one predominantly clear sky day, three shallow convective days of which one developed prominent ABL rolls, one overcast day with organized roll patterns, one day with locally forced precipitating

convective clouds and one precipitating deep convective day (Fig. 37). The ICON-LES and NWP studies focus on these example cases, while the complete set of the simulations otherwise covers most of the days during the intensive observational period of FESSTVaL from the June 7 to July 4 2021. The ICON-SCM experiments were run in real-time during the entire campaign and the results are published at https://ikroener.github.io/fesstval_figs/html/modellierung.html. The MicroHH case studies include 14 (clear), 17 (thin shallow cumulus) and 27 June (deeper shallow cumulus) which were the days with the best conditions for the surface radiation studies and coverage of the surface radiation network measurements.

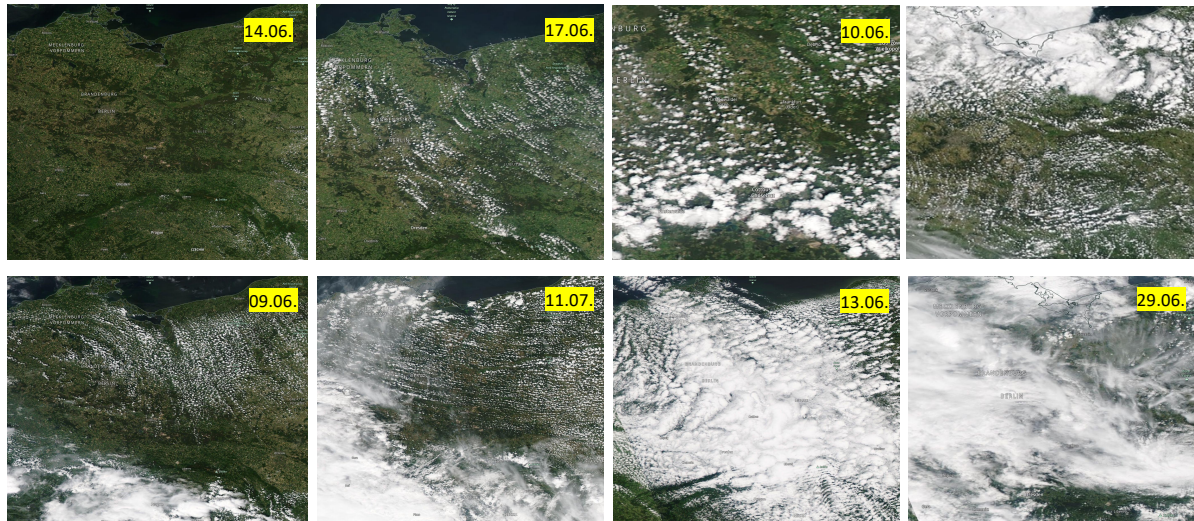


Figure 37 Selected example cases of the FESSTVaL campaign. Moderate Resolution Imaging Spectroradiometer (MODIS) images taken from the NASA's Worldview.

In the next phase of HERZ, we plan to exploit the established modelling framework and expand the modelling studies to include more modelling systems worldwide, setting up FESSTVaL as one of the benchmark cases for model development and intercomparison. The topics we plan to propose include the development and evaluation of the ABL schemes, the evaluation of the performance of various stochastic ABL and convection parameterizations in cold pool cases, and surface radiation topics. The extension to more topics of focus in FESSTVaL such as wind gusts as well as the establishment of the ICON-system in the specific FESSTVaL configuration operationally at the Lindenberg site for research purposes, future campaigns and parameterization development are foreseen in the future activities within HERZ.

4.2 Scientific findings

4.2.1 Realistic LES

The LES mode of the ICON model stems from the NWP version of ICON and was first developed by Dipankar et al. (2015) and used in real-case studies by Heinze et al. (2017). Similar to Heinze et al. (2017), we use ICON-LES in a limited area mode with a two-way nesting setup. The coarsest resolution grid of our LES setup (600 m) is forced by the ICON operational forecasts at about 2.2 km horizontal grid resolution, while three two-way nested grids are used with the finest resolution of about 75 m. The ICON-LES uses a 3D turbulence scheme of Smagorinsky-Lilly (Lilly, 1962), while the parameterizations of convection, subgrid-scale orographic effects and gravity wave drag parameterization are switched off. TERRA land surface model (Schulz and Vogel, 2020) is used interactively with the option for subgrid land-surface variability turned off due to the high LES horizontal resolutions. Among other static land-surface data also used in the operational ICON-NWP, our setup uses ASTER orography data with the original resolution of 1" and Corine land cover data set at 100 m resolution (see also Section

4.2.5).

To assess how realistic the real-case LES are, we first compare the model output with the observations at the Lindenberg, Falkenberg and Kehrighk observational sites. We focus on the diurnal changes of temperature, humidity and wind speed, vertical thermodynamic profiles and surface energy budget (Figs. 38,39,40). An overview of the model performance is given for typical conditions observed during summer, a clear sky day, fair weather cloudy day and deep convective day (Fig. 38). The ICON-LES model captures the diurnal cycle in temperature and humidity well, even the abrupt changes in temperature, humidity and wind speed with the passage of a cold pool front in the afternoon of the 29.6.2021. The vertical structure of the ABL and its growth during the day is also well captured for all three example cases (Fig. 39). An example of the surface energy budget in the model and observations is plotted in Fig. 40. The surface turbulent heat flux is sensitive to the spatial variability in soil moisture, land cover and soil types, but is also influenced by the convective circulations in the ABL (not shown here). This sensitivities of the surface flux to the variability in the surface properties and convective circulations explains the discrepancy between the modeled and observed sensible heat flux. In-situ measurements provide the surface heat flux representative of the land cover conditions at the measurement point which is located either in the area covered by crops (Falkenberg) or a forest (Kehrighk), while the modelled heat flux is the flux averaged over the area of about 80 m² around Falkenberg. A better estimate of the area-averaged flux is obtained from the measurements using large-aperture scintillometers that operate along the path of about 5 kilometers between the sites at Lindenberg and Falkenberg. However, we also find a disagreement between the modelled area-averaged sensible heat flux and the flux estimated

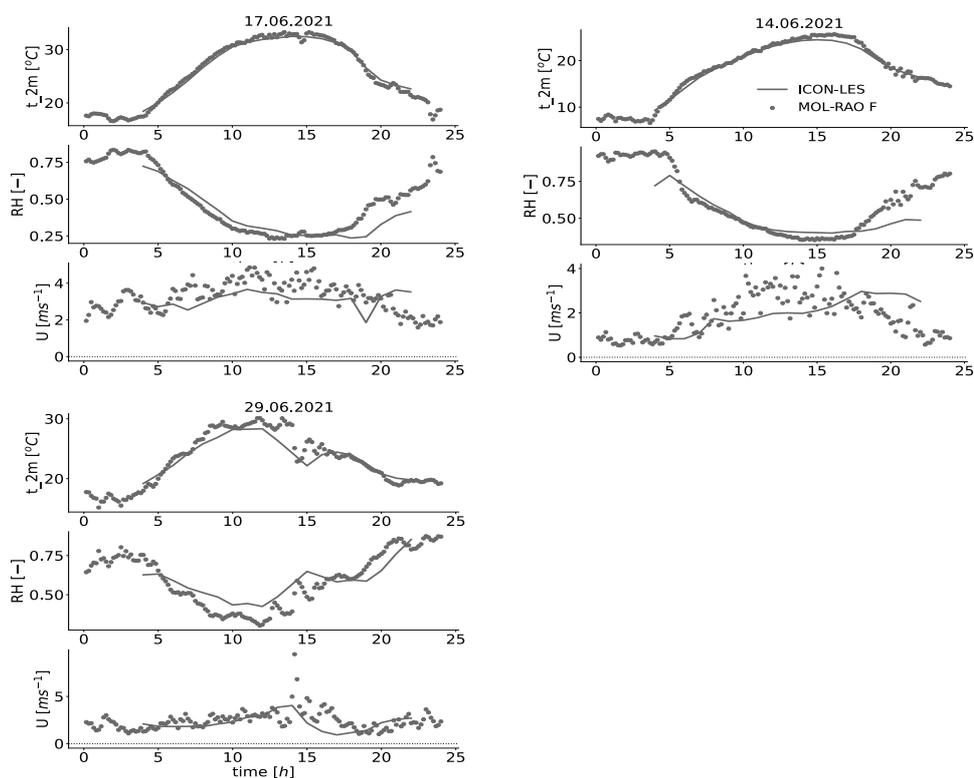


Figure 38 Comparison between the modelled (ICON-LES) and measured (MOL-RAO) temperature and relative humidity at the 2m height and wind speed at the 10m height for a predominantly clear sky day, a day with shallow clouds and deep convective day.

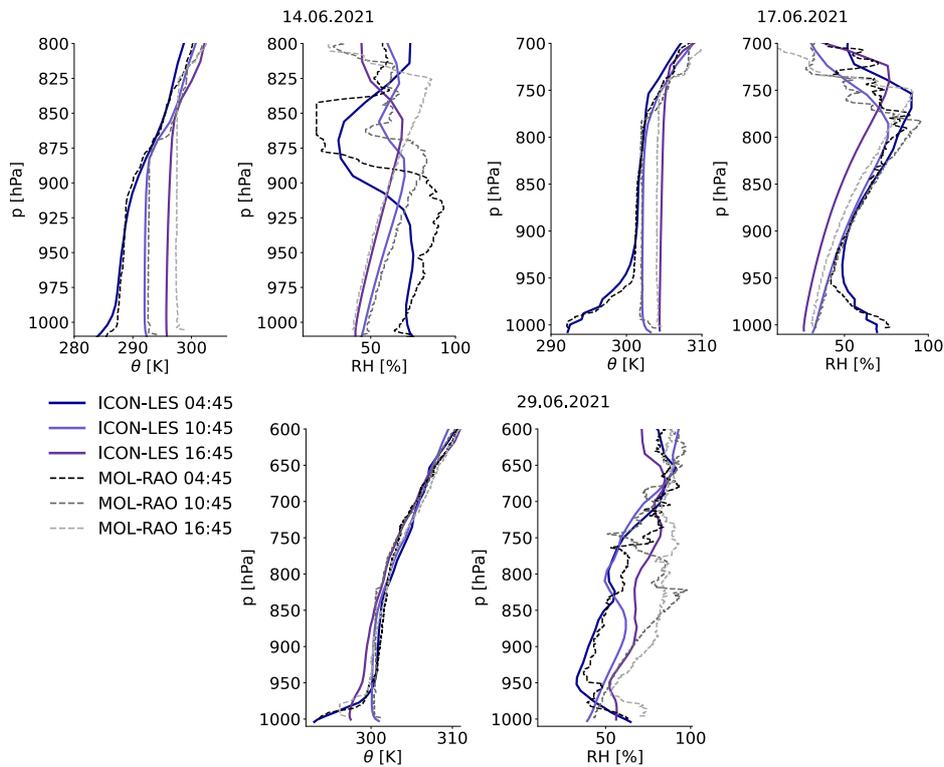


Figure 39 Comparison between the modelled (ICON-LES) and measured (MOL-RAO) vertical profiles of the potential temperature and relative humidity, clear-sky day.

using the scintillometer measurements especially near the mid-day peak (Fig. 40, left). The measured sensible heat flux is higher over the forest at the Kehrigk site, while the latent heat flux is lower compared to the flux measured at the Falkenberg site. The ICON-LES is not able to capture such a change in the flux values depending on the vegetation type. The gap in the closure of the surface energy budget in observations is shown in Fig. 40 (right) for both types of measurements, the eddy-covariance method and scintillometry (see also Mauder et al., 2020), while in the ICON-LES the closure of the surface energy budget is assured by the model formulation (the total surface heat flux as modelled by ICON is thus not plotted).

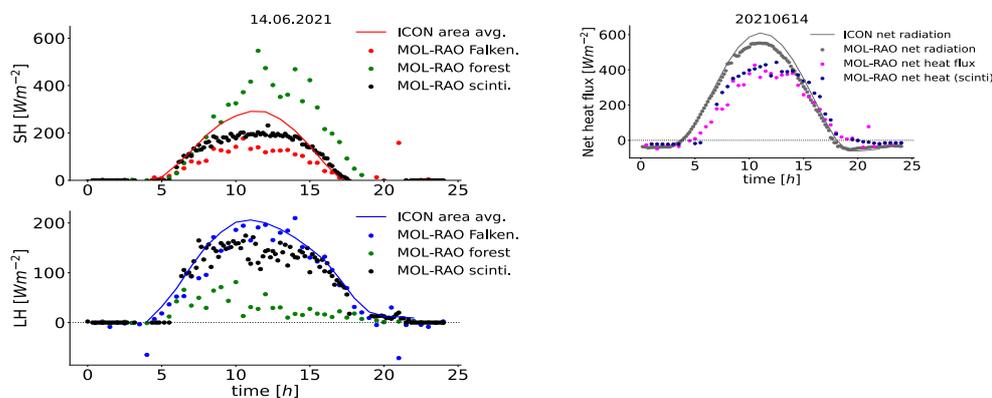


Figure 40 Comparison between the modelled (ICON-LES) and measured (MOL-RAO) surface turbulent heat fluxes (left) and the surface energy budget (right) for an example of a clear-sky day.

As a measure of the variability and intensity of turbulence in the ABL, the variance of vertical velocity as modelled in LES is compared to the FESSTVaL measurements derived from a Doppler Lidar (DL) in vertical stare mode (Fig. 41). Similar to the previous work of Heinze et al. (2017) the variance is underestimated in LES and changes with the horizontal resolution of the LES model. There are two possible reasons for this underestimation of the variance: first and most likely is the horizontal grid resolution of the LES of about 75m which is still insufficient to fully resolve the ABL convection (large eddies) and second, the area over which the variance is sampled in the model does not correspond well to the spatial scales of the origin of the convective circulations advected over the measurement point of the DL.

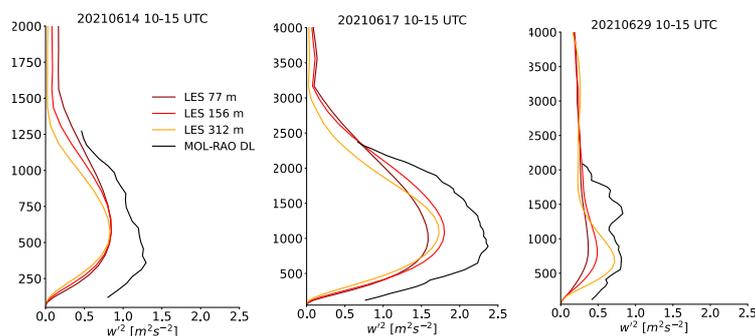


Figure 41 Comparison between the modelled (ICON-LES) and measured (MOL-RAO) surface turbulent heat fluxes (left) and the surface energy budget (right) for an example of a clear-sky day.

4.2.2. Testing of the ABL schemes in ICON

Several available ABL and convection schemes in ICON are tested using the ICON-LES and FESSTVaL observations as a reference in the modelling framework described above. The configurations of the model physics for these tests include:

- The operationally used configuration (ICON-NWP);
- The configuration with a newly developed unified turbulence and convection scheme: the two Turbulent Energies coupled to an Assumed PDF scheme (2TE + APDF; Bařtak Duran et al., 2022);
- The stochastic shallow cloud scheme of Sakradzija et al. (2015; 2016);
- The cold pool parameterization scheme (CPP) developed by Hirt et al. (2021).

The tests are organized around two main topics of interest, the coherent structures in the ABL such as boundary layer rolls and longer-lasting secondary convective circulations and cold pools that develop after deep precipitating convective events.

4.2.2.1 Coherent ABL structures

Thanks to its high horizontal and vertical resolution, the ICON-LES can realistically represent submesoscale spatiotemporal coherent structures. This was demonstrated in several realistic cases during the FESSTVaL measurement campaign (cases shown in Fig. 37). The submesoscale coherent structures are difficult to simulate in NWP models because their scales lie in the gray zone of convection, which makes them partly unresolved by the dynamics in current NWP models. Additionally, traditional parameterizations of convection, turbulence, and cloud processes are based on assumption that transport caused by these structures is entirely unresolved. Therefore, if physical parameterization of convection is used, it is usually too active, which prevents the dynamics of the model to contribute to the representation of these coherent structures. Thus, the modeled coherent structures have unrealistic spatiotemporal organization.

On the other hand, if no convection parameterization is used, the dynamics of the model cannot resolve all scales of the coherent structures, hence a significant part of the processes is not represented. The horizontal resolution of the NWP models plays an important role in this aspect. It is expected that the representation improves with increasing resolution. However, most current physical parameterizations are not scale-aware in the gray zone of convection, thus an increase in resolution does not guarantee a better forecast.

Data from the FESSTVaL measurement campaign present a rare opportunity to test the ability of NWP models to simulate such coherent structures at different resolutions. Here, we compare two ICON configurations: the operationally used configuration (NWP) and the configuration with a newly developed unified turbulence and convection 2TE + APDF scheme (Bařtak řuran et al., 2022). Both were run with a horizontal resolution of approximately 2.5 km.

One of the most interesting cases for this kind of study is the day of 13.6.2021 with horizontally elongated boundary-layer rolls. In ICON-LES, clouds are formed at the top of the updraft flanks of the coherent roll structures (Fig. 42) and imprint on the surface turbulent heat fluxes (not shown). The NWP setup of the ICON model produces a different mode of organized resolved flow with structures that are oriented perpendicular to the horizontal wind direction and are less regular compared to the ICON-LES. A striking feature of the NWP simulation is an undisturbed resolved horizontal flow that is decoupled from the coherent structures in the vertical velocity, the cloud field, and the surface heat fluxes. In comparison, ICON with 2TE + APDF scheme gives rise to elongated horizontal structures that resemble those produced by the ICON-LES at finer spatial scales. The resolved flow interacts (convergence and divergence) with these coherent structures and shows a good coupling between the 2TE + APDF scheme and the ICON dynamical core. Sensitivity experiments with different horizontal resolutions (1.2 km, 2.5 km, 5 km) also show that the better interaction of the 2TE + APDF scheme with the dynamics of the model improves the scale awareness of the ICON model (not shown here).

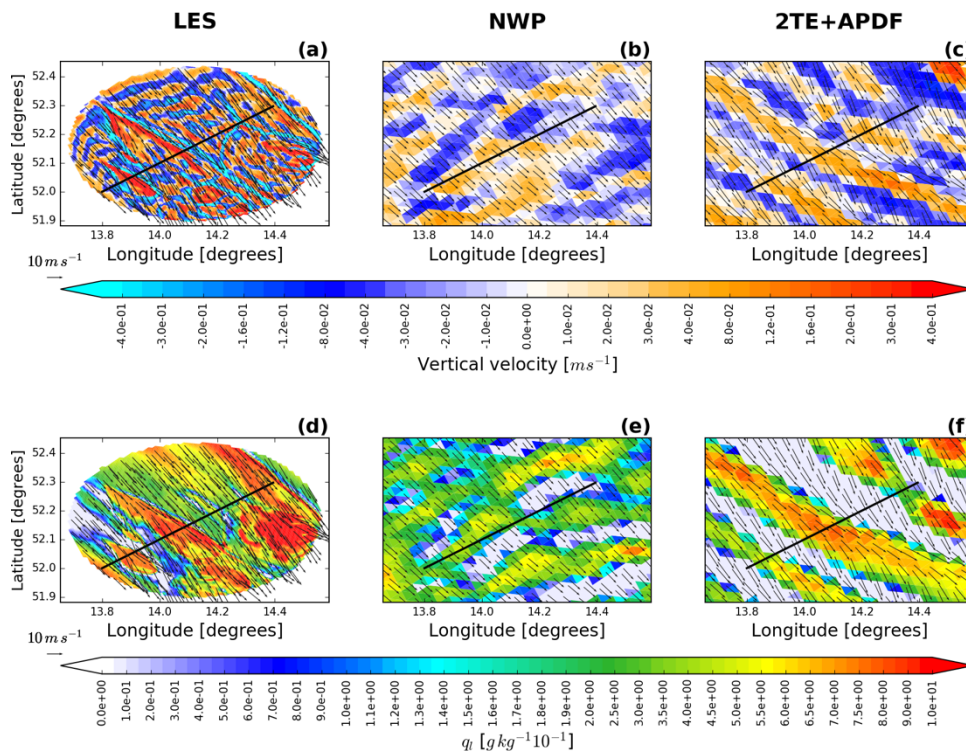


Figure 42 Horizontal cross sections of the vertical velocity (a–c) and the liquid water content (d–f) at the 44th model level height (approx. 1,900 m above the surface). Vector field of the horizontal velocity at the corresponding height is depicted with arrows. Real case simulation over the Lindenberg Observatory starting on 13.06.2021 after 10 hr of integration, starting at 00 UTC. Comparison between ICON-LES (LEM) and ICON-LAM (2.5 km resolution) with the NWP setup, and with 2TE + APDF scheme.

Another case with shallow boundary layer circulations organized in roll structures was observed on June 17th 2021 over Eastern Germany and Western Poland. This case proved to be an interesting testing ground for the shallow convection parameterization in the “grayzone”. The NWP setup here differs slightly from that in the previous case study, using a modified version of the shallow convection scheme. In order to successfully simulate the organized boundary layer rolls, the model must be able to represent the coupling between the parameterized convective processes and the resolved boundary layer eddies. ICON is able to produce the observed roll structures qualitatively, in part thanks to the moist static energy closure employed in the Tiedtke-Bechtold shallow convection scheme. This closure calculates the cloud base mass flux as a function of the moist static energy convergence within the subcloud layer. Thus, a direct link between mass convergence in the subcloud layer and convective activity is “built-in” to the scheme. However, the scheme cannot successfully address the problem of the appropriate spatial scales for the boundary layer circulations. These are resolution-dependent and appear to approximate the lowest effectively resolved horizontal scales of the model configuration. This is illustrated in Fig. 43, showing simulations at approx. 5, 2.5 and 1.2 km horizontal grid spacing.

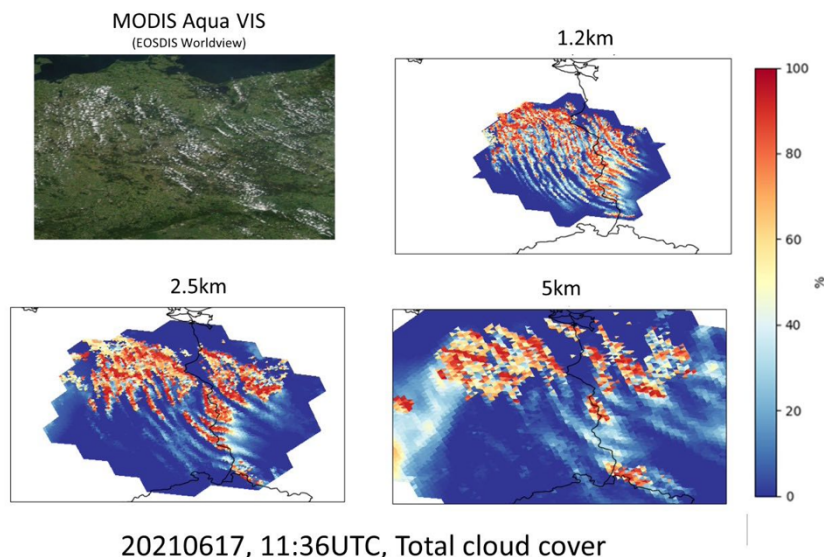


Figure 43 Resolution dependency of the simulated ABL rolls on the 17.6.2021.

The latter case is also a suitable test bed for the stochastic shallow convection parameterization developed as part of the HERZ collaboration with U. Hamburg/MPI (Sakradzija et al., 2015; 2016; Sakradzija and Klocke, 2018). Per design, the scheme is scale-adaptive and tailors the parameterized mass flux to suit the model’s horizontal resolution. A core assumption of the scheme is that the conventional mass flux closure is appropriate only at a coarser scale large enough to contain a representative cloud ensemble, while the location of individual clouds at smaller scales (e.g. within a km-scale grid box) is random. To account for this, the closure is calculated at a coarser scale than the horizontal resolution of the model. On the other hand, the scheme retains the direct link to the resolved circulation via the moist static energy closure mentioned above. It is therefore the choice of the “representative larger scale” that the closure is applied to that determines whether the boundary layer roll circulations are represented by the scheme or not. With the current implementation choice of applying the closure to the “halo” region surrounding the ICON grid box (12 immediately neighbouring grid boxes, a choice partially motivated by code-design arguments), the roll circulations are retained. This implementation choice favours a representation of the boundary layer roll circulations (even if they occur at incorrect scales) over a scheme that is “agnostic” of these circulations because they fall

below the horizontal scales that ICON can correctly resolve (approx. $8dx$ or $18km$ at a horizontal grid spacing of $2.2 km$, based on 2D kinetic energy spectra).

4.2.2.2 Cold pools

Over the past year, the HERZ partners at Hamburg University have analysed observations from the FESSTVaL measurement network to characterize the morphology of cold pools (Kirsch et al., 2022b), providing the opportunity to investigate to what degree the ICON model is able to reproduce the observed cold pool characteristics. To answer this question, simulations with ICON were performed with the NWP modelling setup at $2.5 km$ horizontal resolution for the approximately 40 days during which cold pool events were observed during FESSTVaL. Individual cold pool events were identified in the model output in a manner similar to the detection within the measurement network: The cold pool origin is identified as the grid point first exceeding a (case-dependent) precipitation threshold within the model domain. A region of similar size to the measurement network around the cold pool origin is then defined, and cold pool area (all grid points with temperature depression exceeding $2K$), cold pool intensity (temperature depression averaged across cold pool area) and the total accumulated precipitation in the region around the cold pool origin are calculated for a 4-hour period.

Generally speaking, ICON is successful at generating cold pools on most days with observed cold pool features during the FESSTVaL period. However, the intensity of the cold pool activity in the model is dependent on the model configuration. With the original Tiedtke-Bechtold shallow convection scheme, relatively strong cold pools are generated. The ICON configurations using the currently operational “grayzone tuning” for shallow convection or the two-moment microphysics produce less intense precipitation and therefore also less intense cold pools. The cold pools analyzed in Fig. 44 are from the default Tiedtke-Bechtold scheme and show that the simulated cold pools share many characteristics with those observed. We also tested the impact of the cold pool parameterization scheme (CPP) developed at Ludwig-Maximilians-University Munich (Hirt et al., 2021), and can show that this does enhance the simulated cold pool area, intensity and associated precipitation as designed.

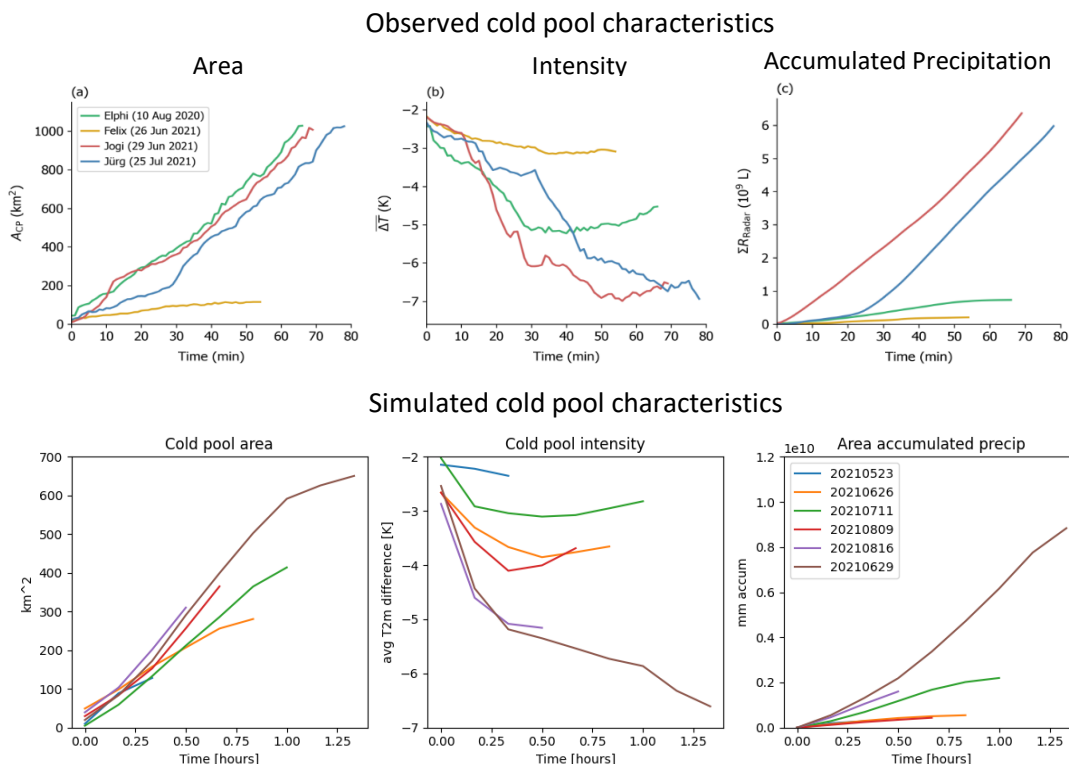


Figure 44 Simulated cold pool characteristics compared to the observed characteristics for selected cases.

An interesting specific case is the cold pool event observed on 29.6.2021, which is a landmark FESSTVaL case. The ICON-LES shows a realistic flow representation of a cold pool (Figs. 45a and 45d). The cold pools are visible via the temperature anomaly near the surface. The horizontal flow is divergent in the center of the cold pools, which is correlated with the negative vertical velocity in the downdraft. The placement and timing of cold pools in the ICON-NWP configuration do not match the ICON-LES (Figs. 45b and 45e). ICON with 2TE + APDF scheme is able to simulate a cold pool that is in the same area as the ICON-LES domain. Its magnitude is clearly overestimated, but the interaction of the cold pool with the horizontal flow appears to be realistic.

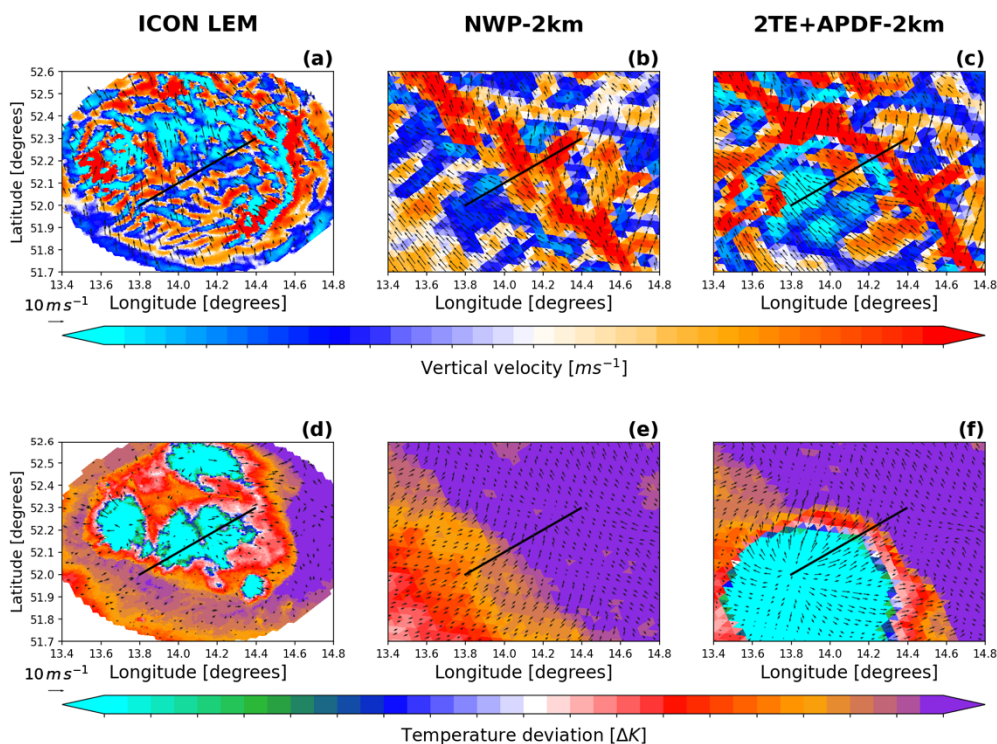


Figure 45 Horizontal cross sections of the vertical velocity (a–c) and the temperature anomaly (d–f) at 10 m above the surface. Vector field of the horizontal velocity at the corresponding height is depicted with arrows. Real case simulation over the Lindenberg Observatory starting on 29.06.2021 after 15 hr of integration, starting at 00 UTC. Comparison between ICON-LES (LEM) and ICON-LAM (2.5 km horizontal resolution) with the NWP setup, and with 2TE + APDF scheme.

4.2.3 MicroHH LES

The focus of the LES modelling at Wageningen University is on the ability of high-resolution model to represent the observed surface variability, particularly in surface solar irradiance. For this work, we have forced the MicroHH model against ERA5 forcings, created with the (LS)²D Python package. By doing so, the model is run in doubly periodic mode, but with large scale advection terms consistent with the large-scale meteorology. Such a mode should be good in simulation locally generated dry convection and small-scale cumulus clouds, as inflow of larger cloud systems is not possible.

Our primary task was first to compare the simulations against observations. The first evaluation was that of the downwelling radiation components as shown in Figure 46. Here it is seen that MicroHH, just as ICON-NWP, captures the diurnal cycle of radiation well, and delivers excellent clear sky radiation, as seen in the validation of the 14th of June. For this day, the downwelling

longwave is produced well in the model, showing that temperature and humidity profiles in the boundary layer are well represented. For the days with cumulus clouds, both models produce clouds and hence introduce variability in the incoming radiation. The spatially averaged line shows a slight reduction due to clouds in the downwelling shortwave. The recording at a single grid cell introduces the variability that is also observed in the field observations.

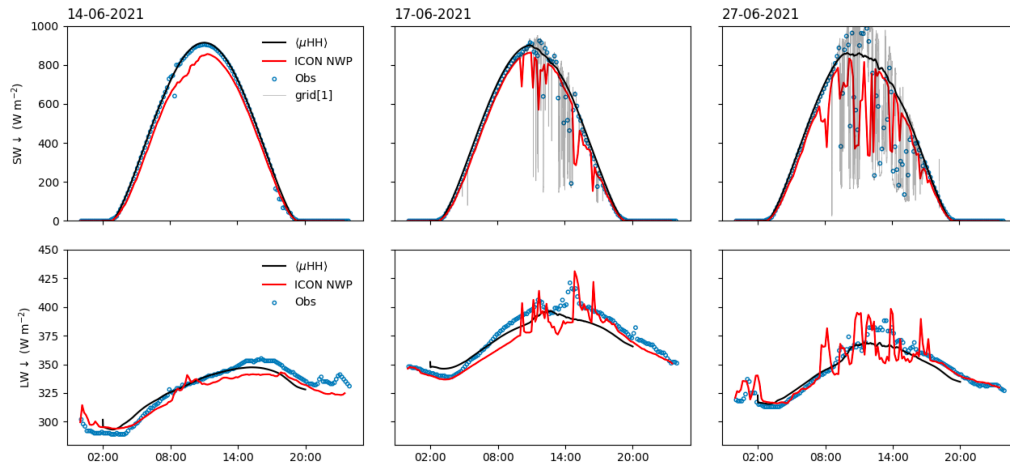


Figure 46 Evaluation of the incoming shortwave and longwave surface solar irradiance for the three selected days.

The accurate representation of the radiation components results also in a good match of temperature and specific humidity with the observations (Fig. 47). The diurnal cycle of temperature is very close to the observations, showing the ability of the model to capture the boundary-layer dynamics well. It needs to be noted that also ICON shows a very close match with observations, but that the temperature and humidity here are recorded at 2 m, rather than at the 10 m of the MicroHH observations that matches exactly with the observations, if corrected for that, the match is nearly perfect as well. ICON NWP captures the diurnal evolution of specific humidity almost perfectly, indicating that accurate boundary forcings of humidity fields might be very important to produce this case correctly.

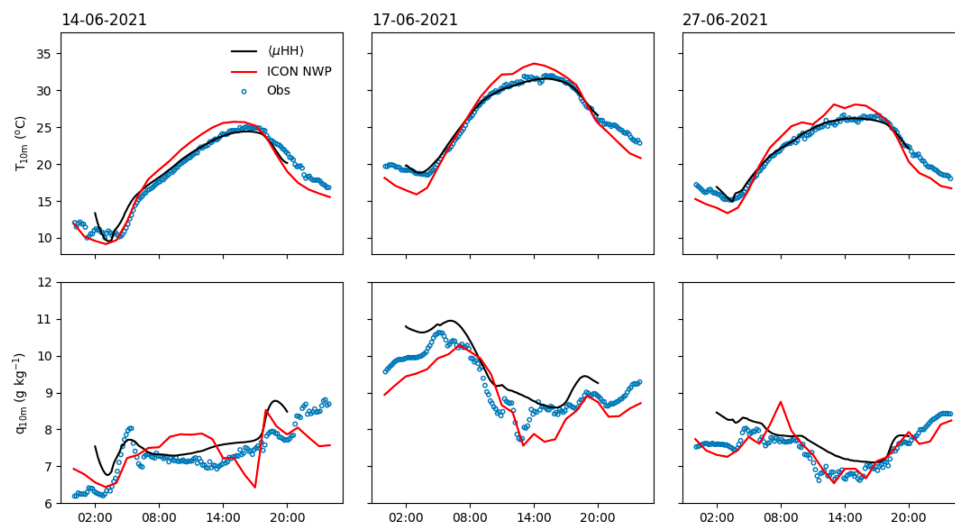


Figure 47 Evaluation of the modeled near surface temperature (top row) and specific humidity (bottom row) of MicroHH and ICON NWP for the three selected days. Note that the ICON NWP temperature and humidity are the 2-m values as 10 m was not available. Hence ICON performance is better than this figure suggests.

The ultimate goal of the MicroHH experiments is to reproduce the observed cloud-driven variability in incoming solar radiation. To be able to do this exercise exactly, we estimated cloud cover from radiation and ceilometer observations and compared those to simulation output. This turned out to be a very challenging endeavor, due to the subtle differences in what is measured or recorded exactly by different instruments and what is the impact of different averaging procedures. Figure 48 shows the estimated cloud cover from our simulations, radiation observations, and a ceilometer. The horizontally averaged cloud cover from the simulations (black line) is a smooth line, whereas an average over a subset of 20 grid points mimicking the radiation observation grid (yellow lines) fluctuates more as often only a single or a few clouds are contained within the 200 x 150 m of our grid, rather than the 25 x 25 km² of the full simulation field. The cloud cover as estimated from our radiation grid (blue) and the ceilometer (red) fluctuate strongly and have high peaks as often the instruments are fully shaded by individual clouds or observe no clouds at all. In ongoing research, we are comparing the cloud cover as determined by the simulations and instruments in more detail to learn more about the 3D effects of radiative transfer in shallow cumulus fields.

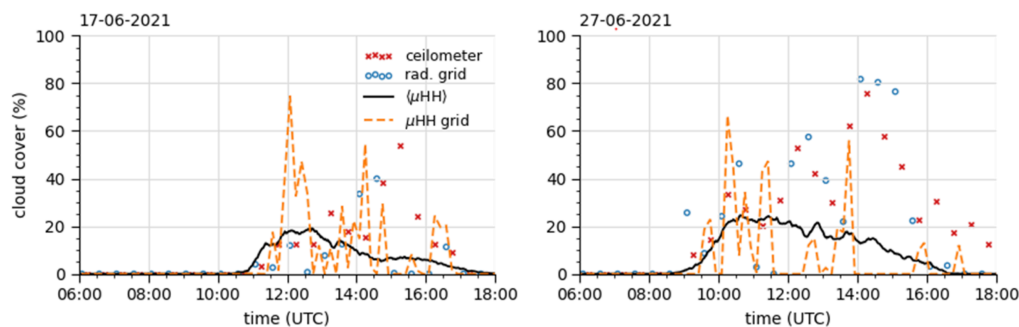


Figure 48 Simulated cloud cover compared against observations from the ceilometer and the radiation grid.

4.2.4 Data assimilation: representation of the land surface

In the past years, a lot of work has been done in Herz Bonn towards investigating how to improve the surface representation in the DACE assimilation framework, i.e. including a better land use dataset (CORINE) and assimilating the land surface temperature (LST) in KENDA. FESSTVaL also provided additional dense observations of the near surface, which are crucial for a correct evaluation. At the time of writing, only part of the presented simulations are focusing on the field campaign period, and this framework provides the bases for comparisons.

The assimilation of the satellite composite LST across the D2.1 domain is performed for the onset of the June 2019 heatwave, due to the lack of clouds which leads to the highest possible number of observations. The experiments with the LST assimilation show an overall improvement in the quantities at the assimilation step, as well as in the 1-hour forecasts, shown for an area of 1.5 degrees longitude and latitude box centered over Berlin and the Urban Metropolitan area of NRW (Fig. 49). While the heatwave is developing over NRW, the Berlin region is on the eastern edge.

The assimilation reduces the daytime surface temperature biases averages from 7-10K to 6-1K, depending on the assimilation settings and the region. The assimilation is not able to completely correct the biases in surface temperature as the ensemble spread is not high enough (up to 2.5K during daytime).

The sharp decrease in surface temperature in the 1-hour forecast affects the 2-meter temperature biases differently depending on the region (Fig. 50). While the Berlin area shows that the surface temperature changes affect the 2-meter temperature, this is not true for the NRW region.

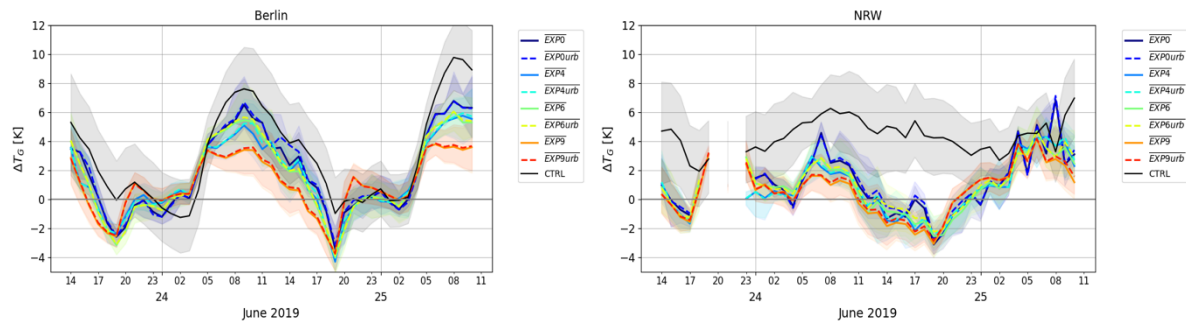


Figure 49 1-hour surface temperature biases for the control simulation (black line, no LST assimilation) and for some of the experiments with different assimilation settings, for two 1.5 longitude-latitude boxes around Berlin (left) and the Ruhr metropolitan area (right).

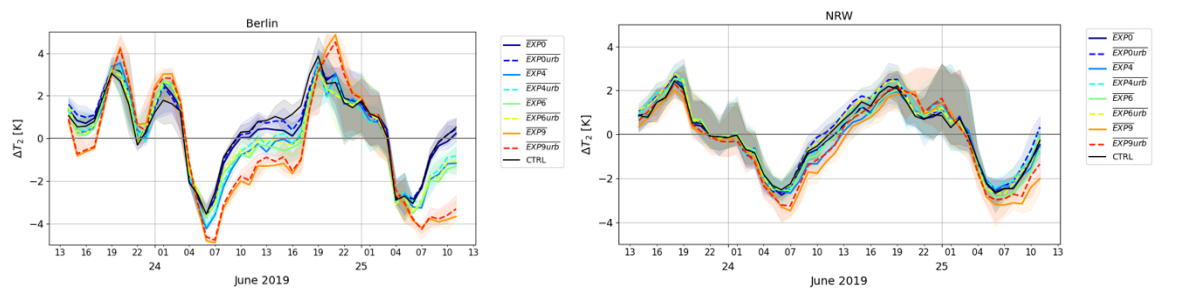


Figure 50 Same as Fig. 49, but for the 1-hour 2-meter temperature biases.

Ongoing work shows that the Berlin region was already suffering from a really low soil moisture, while NRW was undergoing a drying forced by the heatwave conditions, giving a possible radically different response of the atmosphere to the soil conditions.

Similar results are obtained for a set of sensitivity tests performed at the LES scales using different initial soil moisture conditions, namely half and twice the original, its spatial average and a perturbation of it (rows of Fig 51), and comparing the results with the observations, T2m and the Bowen ratio. The Bowen ratio provides a good indicator of the energy partitioning at the surface, thus the soil-atmosphere coupling (Seneviratne et al. 2010).

First of all, the 2-meter temperature does not show a model resolution dependency, while the Bowen ratio shows some variability. The results of the sensitivity tests shows that the 2-meter temperature responds more to changes in the total area-averages soil moisture (row two and three, as compared to the last two), rather than the changes in the Bowen ratio (row one compared to the last two). Small scales soil moisture perturbations have also no effect on neither the 2-meter temperature nor to surface energy partitioning.

These two works provide a solid baseline in addressing a multi-scale soil-atmosphere coupling issues, from the LAM to the LES scales, and the difference in the periods simulated only highlights the need for further investigation. The work of including the land surface temperature satellite observations in the data assimilation shows how an improvement there does not lead to one in the 2-meter temperature consistently. The LES work shows how having a better correspondence between the observed Bowen ratio and the modeled one, does not always lead to an improve in the 2-meter temperature. Further, the results point to the importance of the area average of the soil moisture, rather than its smaller scales perturbations.

Future work includes the inclusion of data assimilation for the FESSTVaL modeling experiments at multiple resolutions, both to provide better initial and boundary conditions to the free simulations and to investigate the impact of high-resolution observation networks in representing these phenomena.

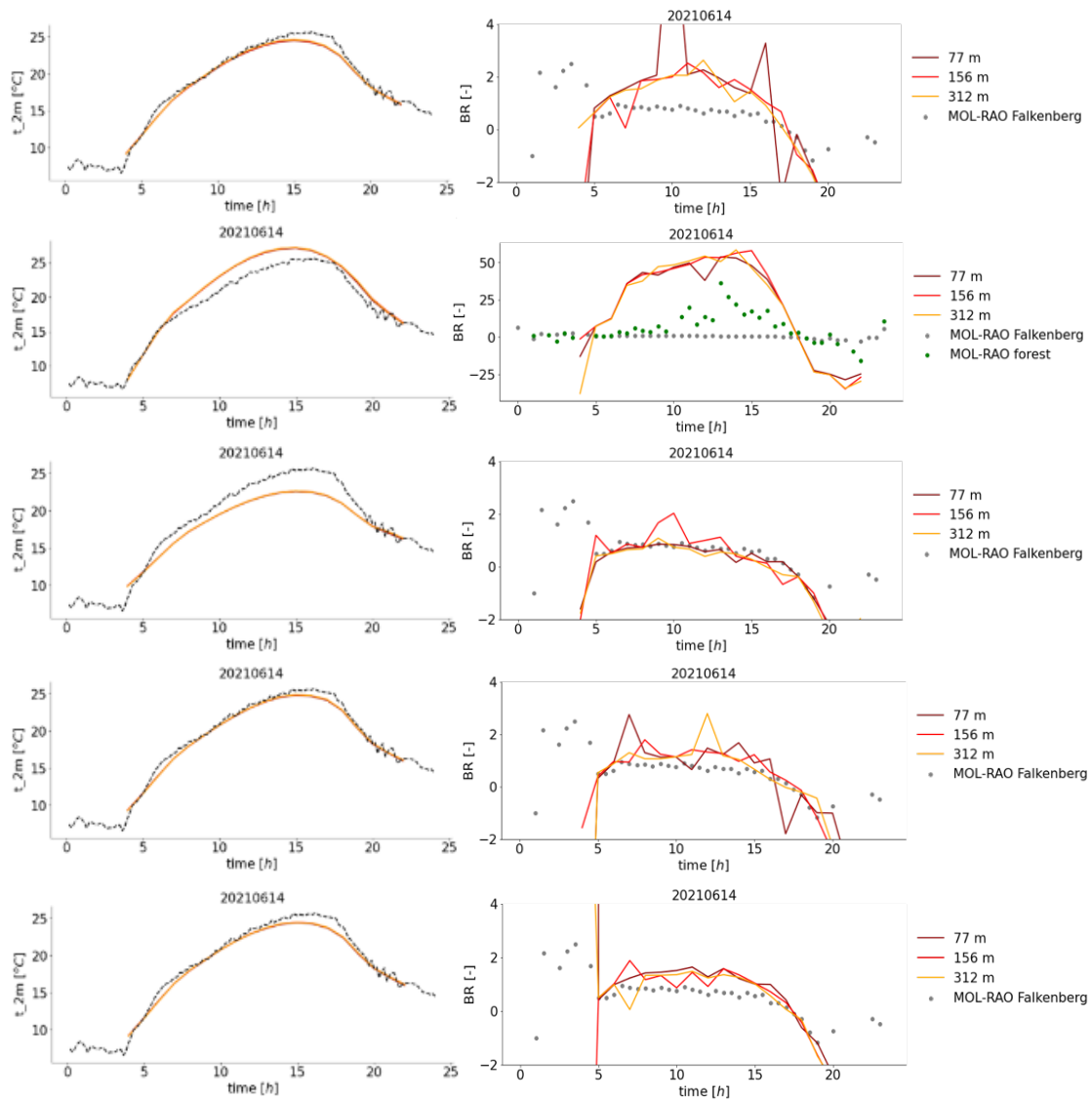


Figure 51 T2m (left) and Bowen ratio (right) timeserie for the experiments with different initial soil moisture conditions: in order, original D2.1, half, twice, a constant value equal to the area average, and a perturbation around the average. The Bowen ratio for the half initial soil moisture has a different scale than the other plots.

5. Data strategy

The data of the FESSTVaL measurement campaign as well as the FESST@home are part of the SAMD archive. The data stored here meets the specific data standard. During the measurements raw data was collected and saved on an ftp-server. Afterwards it was cleaned and rehashed.

In the course of the campaign a so-called PI in charge wrote daily reports. During the IOP daily weather briefings were scheduled. Quicklooks on the FESSTVaL website provided condensed information on the latest measurements throughout the campaign. Furthermore a Logbook was established for storage of maintenance protocols.

The FESSTVAL measurement data follows a certain data policy, available via <http://doi.org/10.25592/uhhfdm.10181>. According to which data from the FESSTVaL campaign may be used freely for research and commercial applications.

6. Education and outreach

- During the campaign, lecture series were carried out: <https://fesstval.de/en/summer-school/translate-to-english-lecture-series-2021>
- The planned summer school had to be canceled due to pandemic restrictions. Instead, a “Joint FESSTVaL & PROBE Training School on network-ready thermodynamic profiling” was carried out at the University of Cologne from March 28 to April 1, 2022. Organized by TB Cologne/Bonn and TB Berlin
- Pressebeiträge auf Deutsch: cf. <https://fesstval.de/presse>
- Articles in english: cf. <https://fesstval.de/en/news/press-articles>

7. Collaboration and networking (national and international)

FESSTVaL is carried out as an overarching project within HErZ as a close and continuous cooperation between DWD, all the HErZ groups (TB Hamburg, TB Berlin, TB Köln/Bonn, TB Frankfurt) and external national and international partners as listed below:

- Environmental Physics, University of Tübingen
- Institute of Atmospheric Physics, Deutsches Zentrum für Luft und Raumfahrt (DLR)
- Institute of Meteorology and Climate Research - Atmospheric Environmental Research, Campus Alpin, Karlsruhe Institute of Technology
- Institute of Geo-Hydroinformatics, Technical University Hamburg-Harburg
- Technical University Berlin.
- METEK GmbH
- DWD Mobile Messeinheit (MME) Potsdam
- Helmholtz-Centre for Environmental Research GmbH (UFZ Leipzig)
- LR-Tech/National Oceanic and Atmospheric Administration (NOAA)
- Finnish Meteorological Institute/ University of Helsinki
- Meteorology and Air Quality, Wageningen University and Research

8. Project-related scientific publications

8.1 Peer-reviewed articles (published, or submitted)

2023

- (1) Hohenegger, C. et al., 2023: FESSTVaL: the Field Experiment on Submesoscale Spatio-Temporal Variability in Lindenberg, BAMS, in review
- (2) Dewani, N., Sakradzija, M., Schlemmer, L., Leinweber, R., and Schmidli, J.: Dependency of vertical velocity variance on meteorological conditions in the convective boundary layer, *Atmos. Chem. Phys.*, 23, 4045–4058, <https://doi.org/10.5194/acp-23-4045-2023>, 2023.

2022

- (3) Bašták Ďurán, I., M. Sakradzija, and J. Schmidli (2022): **The two-energies turbulence scheme coupled to the assumed PDF method**, *Journal of Advances in Modeling Earth Systems*, 14, e2021MS002922. <https://doi.org/10.1029/2021MS002922>
- (4) Kirsch, B., C. Hohenegger, D. Klocke, R. Senke, M. Offermann, and F. Ament, 2022a: **Sub-mesoscale observations of convective cold pools with a dense station network in Hamburg, Germany**, *Earth System Science Data*, 14, 3531–3548, <https://doi.org/10.5194/essd-14-3531-2022>
- (5) Steinheuer, J., C. Detring, F. Beyrich, U. Löhnert, P. Friederichs, and S. Fiedler (2022): **A new scanning scheme and flexible retrieval for mean winds and gusts from Doppler lidar measurements**, *Atmos. Meas. Tech. Discuss.*, 15, 3243–3260, <https://doi.org/10.5194/amt-15-3243-2022>
- (6) Wetz, T. and N. Wildmann: **Spatially distributed and simultaneous wind measurements with a fleet of small quadrotor UAS**, *Journal of Physics: Conference Series*, 2265, <https://doi.org/10.1088/1742-6596/2265/2/022086>, 2022.
- (7) Wildmann, N. and T. Wetz: **Towards vertical wind and turbulent flux estimation with multicopter UAS**, *EGUsphere [preprint]*, <https://doi.org/10.5194/egusphere-2022-110>, 2022.

2021

- (8) Bašták Ďurán I, M. Köhler, A. Eichhorn-Müller, V. Maurer, J. Schmidli, A. Schomburg, D. Klocke, T. Göcke, S. Schäfer, L. Schlemmer, and N. Dewani (2021): **The ICON Single-Column Mode**. *Atmosphere*; 12(7):906. <https://doi.org/10.3390/atmos12070906>
- (9) Kirsch, B., F. Ament, and C. Hohenegger (2021): **Convective Cold Pools in Long-Term Boundary Layer Mast Observations**, *Monthly Weather Review*, 149 (3), 811–820, <https://doi.org/10.1175/MWR-D-20-0197.1>
- (10) T. Kox, H.W. Rust, B. Wentzel, M. Göber, C. Böttecher, J. Lehmke, E. Freundl, M. Garschagen: **Build and measure: Students report weather impacts and collect weather data using self-built weather stations**, *Austral. J. Disaster Trauma Stud.*, 25 (3), 79–86, http://trauma.massey.ac.nz/issues/2021-3/AJDTS_25_3_Kox.pdf, 2021.
- (11) Wetz, T., N. Wildmann, and F. Beyrich: **Distributed wind measurements with multiple quadrotor unmanned aerial vehicles in the atmospheric boundary layer**, *Atmos. Meas. Tech.*, 14, 3795–3814, <https://doi.org/10.5194/amt-14-3795-2021>, 2021.

2020

- (12) Steinheuer J., and P. Friederichs (2020): **Vertical profiles of wind gust statistics from a regional reanalysis using multivariate extreme value theory**. *Nonlin Processes Geophys*, 27 (2):239–252. doi:10.5194/npg-27-239-2020.01, ICDC, <https://doi.org/10.25592/uhhfdm.9758>.

8.2 Other publications

- (1) Kirsch, Bastian, 2022: Illuminating convective cold pools with a dense station network. PhD Thesis, Universität Hamburg, Hamburg. doi:10.17617/2.3432702.
- (2) Steinheuer, J., C. Detring, F. Beyrich, U. Löhnert, P. Friederichs, and S. Fiedler: JSt-einheuer/DWL_retrieval: **DWL retrieval**, Zenodo610 [code], <https://doi.org/10.5281/ZENODO.5780949>, 2021a.

8.3 Conference contributions

International

2022

- (1) Lundgren, K., C. Hohenegger, D. Klocke, F. Ament, F. Beyrich, U. Löhnert, M. Göber, H. Rust, M. Sakradzija, I. Bašták Ďurán, M. Masbou, and A. Jahnke-Bornemann: **FESSTVaL: Field Experiment on sub-mesoscale spatio-temporal variability in Lindenberg – the campaign, first results and data availability**, 3rd PAN-GASS Meeting – Understanding and modeling atmospheric processes, July 25 - July 29, 2022, Monterey, USA. (Poster)
- (2) Lundgren, K., C. Hohenegger, F. Ament, F. Beyrich, U. Löhnert, M. Göber, H. Rust, M. Sakradzija, I. Bašták Ďurán, M. Masbou, and A. Jahnke-Bornemann: **FESSTVaL: Field Experiment on sub-mesoscale spatio-temporal variability in Lindenberg – the campaign, first results and data availability**, EGU General Assembly 2022, Vienna, Austria, May 23 – May 27, 2022, EGU22-8889, doi.org/10.5194/egusphere-egu22-8889, 2022. (Oral)
- (3) Kirsch, B., C. Hohenegger, D. Klocke, and F. Ament: **Illuminating the Sub-Mesoscale Structure of Cold Pools with a Dense Station Network during FESSTVaL**, 2nd Workshop on Cloud Organization (WCO2), Utrecht, Netherlands, May 16 – May 19, 2022. (Oral)

2021

- (4) Detring, C., J. Steinheuer, E. Päschke, R. Leinweber, M. Kayser, and F. Beyrich: **First results of a promising Doppler lidar configuration to derive wind gusts within the FESSTVaL campaign**, EMS Annual Meeting 2021, online, Sept 6 – Sept 10, 2021, EMS2021-247, doi.org/10.5194/ems2021-247, 2021.
- (5) Hohenegger, C., F. Ament, F. Beyrich, I. Bašták Ďurán, U. Löhnert, M. Göber, M. Masbou, H. Rust, M. Sakradzija, J. Schmidli, and S. Wiesner: **FESSTVaL: Field Experiment on sub-mesoscale spatio-temporal variability in Lindenberg – the campaign 2021 and its predecessors**, EMS Annual Meeting 2021, online, Sept 6 – Sept 10, 2021, EMS2021-296, doi.org/10.5194/ems2021-296, 2021.
- (6) Göber, M., H. W. Rust, T. Kox, B. Wentzel, C. Böttcher, J. Lehmke, A. Trojand, and N. Fleischhut: **Build, measure, understand: Pupils contributing to meteorological measurement campaigns.**, EMS Annual Meeting 2021, online, Sept 6 – Sept 10, 2021, EMS2021-398, doi.org/10.5194/ems2021-398, 2021.
- (7) Steinheuer, J., C. Detring, F. Beyrich, U. Löhnert, P. Friederichs, and S. Fiedler: **New flexible retrieval for gusts and mean winds from Doppler wind lidars, tested for various scanning configurations**, EMS Annual Meeting 2021, online, Sept 6 – Sept 10, 2021, EMS2021-366, doi.org/10.5194/ems2021-366, 2021.
- (8) Kox, T., M. Göber, B. Wentzel, B. Freundl, and H. W. Rust: **Fostering weather and climate literacy among pupils by engagement in a weather citizen science project**, Proceedings of Austrian Citizen Science Conference 2020 PoS (ACSC2020), doi:10.22323/1.393.0002, 2021.

2020

- (9) Kirsch, B., F. Ament, C. Hohenegger, and D. Klocke: **Sub-mesoscale observations of cold pools during FESSTVaL**, EGU General Assembly 2020, online, May 4 – May 8, 2020, EGU2020-9779, doi.org/10.5194/egusphere-egu2020-9779, 2020.

2019

- (10) Wiesner, S., F. Ament, F. Beyrich, I. Bašták Ďurán, D. Klocke, C. Hohenegger, U. Löhnert, M. Göber, M. Masbou, H. Rust, L. Schlemmer, J. Schmidli, A. Schomburg, S. Wahl, and M. Weissmann (2019): **FESSTVaL: Field Experiment on sub-mesoscale spatio-temporal variability in Lindenberg – the campaign is at the ready**. EMS Annual Meeting 2019, Copenhagen, Denmark, Sept 9- Sept 13, 2019 (Oral)
- (11) Klocke, D. (2019): **FESSTVaL: Field Experiment on sub-mesoscale spatio-temporal variability in Lindenberg**. Workshop Observational campaigns for better weather forecasts, ECMWF, London, Großbritannien, June 10 – June 13, 2019. (Oral)
- (12) Kirsch, B., F. Ament, C. Hohenegger, D. Klocke: **Catching Cold Pools during FESSTVaL 2020**. EGU General Assembly 2019, Vienna, Austria, April 7 – April 12, 2019. (Poster, EGU2019-9238)
- (13) Schlemmer, L., C. Hohenegger, D. Klocke, A. Schomburg, S. Wahl, J. Schmidli, M. Goeber, M. Weissmann, H. Rust, I. Bašták Ďurán, U. Löhnert, F. Ament: **FESSTVaL - Field Experiment on Sub-Mesoscale Spatio-Temporal Variability in Lindenberg**. UCP2019 - Understanding Clouds and Precipitation, Berlin, Germany, Feb 25 - March 2, 2019. (Poster, A217)
- (14) Ament, F., B. Kirsch, D. Klocke, C. Hohenegger: **Catching Cold Pools – dense nets during FESSTVaL 2020**. UCP2019 - Understanding Clouds and Precipitation, Berlin, Germany, Feb 25 - March 2, 2019. (Poster, B218)

2018

- (15) Hohenegger, C., D. Klocke, A. Schomburg, S. Wahl, T. Janjic-Pfander, J. Schmidli, M. Göber, T. Pardowitz, H. Rust, I. Bašták Ďurán, U. Löhnert, M. Masbou, B. Kirsch, F. Ament: **FESSTVaL: Field Experiment on sub-mesoscale spatio-temporal variability in Lindenberg**. EMS Annual Meeting, Budapest, Hungary, Sept 3 – Sept 7, 2018. (Oral, EMS2018-555)

National

2022

- (1) Becker, C., E. Päschke, and F. Beyrich: **Vergleiche von Profilen der turbulenten kinetischen Energie in der Atmosphärischen Grenzschicht auf der Basis von Doppler-Lidar-Messungen mit Simulationsergebnissen des NWV-Modells ICON**, DACH2022, Leipzig, Deutschland, 21–25 March, 2022, [DACH2022-47](https://doi.org/10.5194/dach2022-47), doi.org/10.5194/dach2022-47, 2022.
- (2) Boventer, J., I. Weber, M. Schön, K. zum Berge, A. Platis, J. Bange, F. Beyrich, C. Detring, and E. Päschke: **Validierung von Doppler Wind LiDARen des Deutschen Wetterdienstes (DWD) mit unbemannten kleinen Forschungsflugzeugen (UAS)**, DACH2022, Leipzig, Deutschland, March 21–25, 2022, [DACH2022-243](https://doi.org/10.5194/dach2022-243), doi.org/10.5194/dach2022-243, 2022.
- (3) Detring, C., E. Päschke, J. Steinheuer, R. Leinweber, M. Kayser, and F. Beyrich: **Untersuchungen zur Ableitung von Windböen aus Doppler-Lidar-Messungen**, DACH2022, Leipzig, Deutschland, March 21–25, 2022, [DACH2022-48](https://doi.org/10.5194/dach2022-48), doi.org/10.5194/dach2022-48, 2022.

- (4) Kirsch, B., C. Hohenegger, D. Klocke, and F. Ament: **FESST@HH 2020: Ein dichtes Messnetz als Lupe für die Struktur konvektiver Cold Pools**, DACH2022, Leipzig, Deutschland, March 21–25, 2022, [DACH2022-248](#), doi.org/10.5194/dach2022-248, 2022.
- (5) Lundgren, K., F. Ament, C. Hohenegger, F. Beyrich, U. Löhnert, M. Göber, H. Rust, M. Sakradzija, I. Bašták Ďurán, M. Masbou, and A. Jahnke-Bornemann: **FESSTVaL: Field Experiment on sub-mesoscale spatio-temporal variability in Lindenberg – Übersicht der Messkampagne und erste Ergebnisse**, DACH2022, Leipzig, Deutschland, March 21–25, 2022, [DACH2022-237](#), doi.org/10.5194/dach2022-237, 2022.
- (6) Stankovic, M., B. Kirsch, and F. Ament: **100 Messstationen – eine Stadt: Die raumzeitliche Variabilität der Lufttemperatur in Hamburg während der Messkampagne FESST@HH 2020**, DACH2022, Leipzig, Deutschland, March 21–25, 2022, [DACH2022-240](#), doi.org/10.5194/dach2022-240, 2022.
- (7) Wolz, K., N. Wildmann, F. Beyrich, E. Päsche, C. Detring, and M. Mauder: **Vergleich von Windmessungen verschiedener Doppler Lidarscanstrategien und zweier Lidarmarken mit einem Ultraschallanemometer**, DACH2022, Leipzig, Deutschland, March 21–25, 2022, [DACH2022-282](#), doi.org/10.5194/dach2022-282, 2022.

2019

- (8) Kirsch, B., F. Ament, C. Hohenegger, D. Klocke, I. Bašták Ďurán, M. Göber, T. J. Pfander, U. Löhnert, T. Pardowitz, H. Rust, L. Schlemmer, J. Schmidli, A. Schomburg, S. Wahl, M. Weissmann, F. Beyrich, and M. Masbou (2019): **FESSTVaL - Field Experiment on Sub-Mesoscale Spatio-Temporal Variability in Lindenberg**. Meteorologentagung DACH, Garmisch-Partenkirchen, Deutschland, March 18-22, 2019 (Vortrag, DACH2019-101)
- (9) Kirsch, B., F. Ament, C. Hohenegger, D. Klocke, and R. Senke (2019): **Die Erfassung von Cold Pools mit dichten Messnetzen bei FESSTVaL 2020**. Meteorologentagung DACH, Garmisch-Partenkirchen, Deutschland, March 18-22, 2019 (Oral, DACH2019-102)
- (10) Rust, H., M. Göber, N. Fleischhut und T. Kox (2019): **Ein Bürgermessnetz zur Unterstützung von FESSTVaL**. Meteorologentagung DACH, Garmisch-Partenkirchen, Deutschland, March 18-22 March, 2019 (Oral, DACH2019-243)

9. Data-related publications

9.1 Data policy and data standard

- (1) Wiesner, Sarah. (2022, May 3): **Data Policy for FESSTVaL campaign data** (Version 1.0), <http://doi.org/10.25592/uhhfdm.10181>.
- (2) Jahnke-Bornemann, Annika. (2022, May 2): **The SAMD Product Standard (Standardized Atmospheric Measurement Data)** (Version 2.1), <http://doi.org/10.25592/uhhfdm.10180>.

9.2 Data sets FESSTVaL 2021

- (1) Burgemeister, Finn, Clemens, Marco, & Ament, Felix. (2022): **Rainfall rates estimated from X-Band radar observations during FESSTVaL 2021** (Version 0) [Data set]. <http://doi.org/10.25592/uhhfdm.10090>
- (2) Kirsch, Bastian, Hohenegger, Cathy, Klocke, Daniel, & Ament, Felix. (2022b): **Meteorological network observations by APOLLO and WXT weather stations during FESSTVaL 2021** (Version 00-2) [Data set]. <http://doi.org/10.25592/uhhfdm.10179>
- (3) Löhnert, Ulrich, Knist, Christine, Böck, Tobias, & Pospichal, Bernhard (2022): **Micro-wave Radiometer Observations during FESSTVaL 2021** (Version 00) [Data set]. <http://doi.org/10.25592/uhhfdm.10198>
- (4) Turner, Dave, & Rochette, Luc. (2022): **Thermodynamic retrieved profiles from the ASSIST infrared spectrometer, FESSTVaL campaign** (Version 01) [Data set]. <http://doi.org/10.25592/uhhfdm.10212>
- (5) Wildmann, Norman (2022): **Multicopter UAS measurements at GM Falkenberg during FESSTVaL 2021** (Version 0) [Data set], <http://doi.org/10.25592/uhhfdm.10148>

9.3 Data sets FESST@home 2020 and pre-campaign 2019

- (1) Kirsch, B., Hohenegger, C., Klocke, D., Senke, R., Offermann, M., Ament, F. (2021): **FESST@HH meteorological network measurements** (Version v00) [Data set], doi.org/10.25592/uhhfdm.8966
- (2) Steinheuer, J., Detring, C., Kayser, M., and Leinweber, R. (2021b): **Doppler wind lidar wind and gust data from FESSTVaL 2019/2020**, Falkenberg, data version 01, ICDC, <https://doi.org/10.25592/uhhfdm.9758>.

10. Bibliography

- Bašták Ďurán I, Köhler M, Eichhorn-Müller A, Maurer V, Schmidli J, Schomburg A, Klocke D, Göcke T, Schäfer S, Schlemmer L, Dewani N., 2021: The ICON Single-Column Mode. *Atmosphere*. **12**(7), 906. <https://doi.org/10.3390/atmos12070906>
- Bašták Ďurán, I., Sakradzija, M., & Schmidli, J., 2022: The two-energies turbulence scheme coupled to the assumed PDF method. *Journal of Advances in Modeling Earth Systems*, **14**, e2021MS002922. <https://doi.org/10.1029/2021MS002922>
- Beyrich, F., and W. K. Adam, 2007, Site and Data Report for the Lindenberg Reference Site in CEOP - Phase I. *Berichte des Deutschen Wetterdienstes*, 230, Offenbach am Main, Germany, 55 pp.
- Crewell, S. and U. Lohnert, 2007: "Accuracy of Boundary Layer Temperature Profiles Retrieved with Multifrequency Multiangle Microwave Radiometry," in *IEEE Transactions on Geoscience and Remote Sensing*, vol. 45, no. 7, pp. 2195-2201, doi: 10.1109/TGRS.2006.888434.
- Detring, C., E. Päsche, M. Kayser, R. Leinweber, and F. Beyrich, 2022: Deriving wind gust from Doppler lidar measurements. URL <https://doi.org/10.5194/ems2022-184>, EMS Annual Meeting, Bonn, Germany
- Dewani N., Sakradzija, M., Schlemmer, L., Leinweber, R., and J. Schmidli, in review: Dependency of vertical velocity variance on meteorological conditions in the convective boundary layer, *Atmospheric Chemistry and Physics Discussions* [preprint], <https://doi.org/10.5194/acp-2022-543>
- Dipankar, A., Stevens, B., Heinze, R., Moseley, C., Zängl, G., Giorgetta, M., and S. Brdar, 2015: Large eddy simulation using the general circulation model ICON, *J. Adv. Model. Earth Syst.*, **7**, 963-986, doi:10.1002/2015MS000431
- Fleischhut, N., S. M. Herzog, and R. Hertwig, 2020: Weather Literacy in Times of Climate Change. *Wea. Climate Soc.*, **12**, 435–452, <https://doi.org/10.1175/WCAS-D-19-0043.1>.
- Heinze, R., Dipankar, A., Henken, C.C., et al., 2017: Large-eddy simulations over Germany using ICON: a comprehensive evaluation. *QJR Meteorol. Soc.*, **143**, 69-100, doi:10.1002/qj.2947
- van Heerwaarden, C. C., van Stratum, B. J. H., Heus, T., Gibbs, J. A., Fedorovich, E., and Mellado, J. P., 2017: MicroHH 1.0: a computational fluid dynamics code for direct numerical simulation and large-eddy simulation of atmospheric boundary layer flows, *Geosci. Model Dev.*, **10**, 3145–3165, <https://doi.org/10.5194/gmd-10-3145-2017>
- Heusinkveld, B. G., Mol, W. B., and van Heerwaarden, C. C., 2022: A new accurate low-cost instrument for fast synchronized spatial measurements of light spectra, *EGUsphere* [preprint]
- Hill, R. J., 1997: Algorithms for Obtaining Atmospheric Surface-Layer Fluxes from Scintillation Measurements. *J. Atmos. Oceanic Technol.*, **14**, 456–467, [https://doi.org/10.1175/1520-0426\(1997\)014<0456:AFOASL>2.0.CO;2](https://doi.org/10.1175/1520-0426(1997)014<0456:AFOASL>2.0.CO;2).
- Hirt, Mirjam, and George C. Craig., 2021: A cold pool perturbation scheme to improve convective initiation in convection-permitting models. *Quarterly Journal of the Royal Meteorological Society* **147**, 2429-2447.
- Hohenegger, C. et al, 2023: FESSTVal: the Field Experiment on Submesoscale spatio-Temporal Variability in Lindenberg. *Bull. Ame. Meteorol. Soc.*, revised.
- Kirsch, Bastian, et al., 2022a: Sub-mesoscale observations of convective cold pools with a dense station network in Hamburg, Germany., *Earth System Science Data*, **14**, 3531-3548
- Kirsch, Bastian, 2022: Illuminating convective cold pools with a dense station network. PhD Thesis, Universität Hamburg, Hamburg. doi:10.17617/2.3432702.
- Köhli, M. et al., 2015: Footprint characteristics revised for field-scale soil moisture monitoring with cosmic-ray neutrons. *Water Resour Res* **51**, 5772–5790
- Kooijmans, L.M.J., Hartogensis, O.K., 2016: Surface-Layer Similarity Functions for Dissipation Rate and Structure Parameters of Temperature and Humidity Based on Eleven Field Experiments. *Boundary-Layer Meteorol* **160**, 501–527. <https://doi.org/10.1007/s10546-016-0152-y>

- Kox, T., H.W. Rust, B. Wentzel, M. Göber, C. Böttecher, J. Lehmke, E. Freundl, M. Garschagen, 2021a: Build and measure: Students report weather impacts and collect weather data using self-built weather stations, *Austral. J. Disaster Trauma Stud.*, **25** (3), 79-86
- Kox, T., Göber, M., Wentzel, B., Freundl, E., & Rust, H., 2021b: Fostering weather and climate literacy among pupils by engagement in a weather citizen science project. In Proceedings of Austrian Citizen Science Conference 2020 (2 p.). Proceedings of Science. <https://doi.org/10.22323/1.393.0002>
- Kropfli, R. A., 1986: Single Doppler Radar Measurements of Turbulence Profiles in the Convective Boundary Layer, *Journal of Atmospheric and Oceanic Technology*, **3**, 305 – 314, [https://doi.org/10.1175/1520-0426\(1986\)003<0305:SDRMOT>2.0.CO;2](https://doi.org/10.1175/1520-0426(1986)003<0305:SDRMOT>2.0.CO;2)
- Lengfeld, K., Clemens, M., Münster, H., and Ament, F., 2014: Performance of high-resolution X-band weather radar networks – the PATTERN example, *Atmos. Meas. Tech.*, **7**, 4151–4166, <https://doi.org/10.5194/amt-7-4151-2014>
- Lenschow, D. H., J. C. Wyngaard, and W. T. Pennell, 1980: Mean-Field and Second-Moment Budgets in a Baroclinic, Convective Boundary Layer. *J. Atmos. Sci.*, **37**, 1313–1326, [https://doi.org/10.1175/1520-0469\(1980\)037<1313:MFASMB>2.0.CO;2](https://doi.org/10.1175/1520-0469(1980)037<1313:MFASMB>2.0.CO;2).
- Lilly, D. K., 1962: On the numerical simulation of buoyant convection. *Tellus*, **14**(2), 148–172. <https://doi.org/10.1111/j.2153-3490.1962.tb00128.x>
- Lüdi, A., Beyrich, F. & Mätzler, C., 2005: Determination of the Turbulent Temperature–Humidity Correlation from Scintillometric Measurements. *Boundary-Layer Meteorol* **117**, 525–550 . <https://doi.org/10.1007/s10546-005-1751-1>
- Luiz, E. W., & Fiedler, S., 2022: Spatiotemporal observations of nocturnal low-level jets and impacts on wind power production. *Wind Energy Science*, **7** (4), 1575–1591, <https://doi.org/10.5194/wes-7-1575-2022>.
- Mauder, M., Foken, T. and Cuxart, J., 2020: Surface-Energy-Balance Closure over Land: A Review. *Boundary-Layer Meteorol* **177**, 395–426. <https://doi.org/10.1007/s10546-020-00529-6>.
- Päschke, E., R. Leinweber, and V. Lehmann, 2015: An assessment of the performance of a 1.5 µm Doppler lidar for operational vertical wind profiling based on a 1-year trial, *Atmospheric Measurement Techniques*, **8.6**, 2251–2266. doi: 10.5194/amt-8-2251-2015.
- Rautenberg A, Schön M, zum Berge K, Mauz M, Manz P, Platis A, van Kesteren B, Suomi I, Kral ST, Bange J. The Multi-Purpose Airborne Sensor Carrier MASC-3 for Wind and Turbulence Measurements in the Atmospheric Boundary Layer. *Sensors*. 2019; 19(10):2292. <https://doi.org/10.3390/s19102292>
- Rose, T., S. Crewell, U. Löhnert, C. Simmer, 2005: A network suitable microwave radiometer for operational monitoring of the cloudy atmosphere, *Atmospheric Research*, Volume 75, Issue 3, 183-200, <https://doi.org/10.1016/j.atmosres.2004.12.005>.
- Sakradzija, M., and D. Klocke. 2018: Physically constrained stochastic shallow convection in realistic kilometer-scale simulations. *J. Adv. Model. Earth Syst.*, **10**, 2755-2776, <https://doi.org/10.1029/2018MS001358>
- Sakradzija, M., Seifert, A. and A. Dipankar. 2016: A stochastic scale-aware parameterization of shallow cumulus convection across the convective gray zone. *J. Adv. Model. Earth Syst.*, **8**, 786-812, doi:10.1002/2016MS000634
- Sakradzija, M., Seifert, A. and Heus, T. 2015: Fluctuations in a quasi-stationary shallow cumulus cloud ensemble. *Nonlinear Proc. Geoph.*, **22**, 65-85, doi:10.5194/npg-22-65-2015
- Schrön, M. *et al.*, 2018a: Intercomparison of cosmic-ray neutron sensors and water balance monitoring in an urban environment. *Geoscientific Instrum Methods Data Syst* **7**, 83–99
- Schrön, M. *et al.*, 2018b: Cosmic-ray Neutron Rover Surveys of Field Soil Moisture and the Influence of Roads. *Water Resour Res* **54**, 6441–6459
- Schulz J-P, and Vogel G., 2020: Improving the Processes in the Land Surface Scheme TERRA: Bare Soil Evaporation and Skin Temperature. *Atmosphere*, **11**(5), 513. <https://doi.org/10.3390/atmos11050513>

- Schween, J. H., A. Hirsikko, U. Löhnert, and S. Crewell, 2014: Mixing-layer height retrieval with ceilometer and Doppler lidar: from case studies to long-term assessment, *Atmospheric Measurement Techniques*, **7**, 3685–3704. doi: 10.5194/amt-7-3685-2014
- Seneviratne, S., T. Corti, E. L. Davin, M. Hirschi, E. B. Jaeger, I. Lehner, B. Orlowsky, A. J. Teuling, 2010: Investigating soil moisture–climate interactions in a changing climate: A review, *Earth-Science Reviews*, Volume 99, Issues 3–4, 125-161, <https://doi.org/10.1016/j.earscirev.2010.02.004>.
- Smalikho, I. N. and Banakh, V. A., 2017: Measurements of wind turbulence parameters by a conically scanning coherent Doppler lidar in the atmospheric boundary layer, *Atmospheric Measurement Techniques*, **10**, 4191–4208, <https://doi.org/10.5194/amt-10-4191-2017>, 2017.
- Steinheuer, J., Detring, C., Beyrich, F., Löhnert, U., Friederichs, P. and Fiedler, S., 2022.: A new scanning scheme and flexible retrieval for mean winds and gusts from Doppler lidar measurements, *Atmos. Meas. Tech.*, **15**(10):3243–3260, doi: <https://10.5194/amt-15-3243-2022>
- Suomi, I., Gryning, S.-E., O'Connor, E. J., and Vihma, T., 2017: Methodology for obtaining wind gusts using Doppler lidar, *Q. J. Roy. Meteor. Soc.*, **143**, 2061–2072, <https://doi.org/10.1002/qj.3059>
- Turner, D. D. and Löhnert, U., 2021: Ground-based temperature and humidity profiling: combining active and passive remote sensors, *Atmos. Meas. Tech.*, **14**, 3033–3048, <https://doi.org/10.5194/amt-14-3033-2021>
- Vickers, D. and Mahrt, L., 1997: Quality Control and Flux Sampling Problems for Tower and Aircraft Data, *J. Atmos. Ocean. Technol.*, **14**, 512–526
- Wildmann, N. and Wetz, T.: Towards vertical wind and turbulent flux estimation with multicopter uncrewed aircraft systems, *Atmos. Meas. Tech.*, **15**, 5465–5477, <https://doi.org/10.5194/amt-15-5465-2022>, 2022.
- Wetz, T. und N. Wildmann, 2022: Spatially distributed and simultaneous wind measurements with a fleet of small quadrotor UAS. *Journal of Physics: Conference Series*, 2265 (2), 022086.. doi: 10.1088/1742-6596/2265/2/022086.
- Zängl, G., Reinert, D., Rípodas, P. and M. Baldauf, 2015: The ICON (ICOsahedral Non-hydrostatic) modelling framework of DWD and MPI-M: Description of the non-hydrostatic dynamical core. *QJR Meteorol. Soc.*, **141**, 563-579. doi:10.1002/qj.2378
- Zreda, M. *et al.*, 2012: COSMOS: the COsmic-ray Soil Moisture Observing System. *Hydrol Earth Syst Sc* **16**, 4079–4099